Relaxation in the Electrical Properties of Amorphous Selenium Based Photoconductors

A Thesis
Submitted to the College of Graduate Studies and Research
in Partial Fulfillment of the Requirements for the Degree of
Master of Science
in the Department of Electrical Engineering
University of Saskatchewan

By

Christopher S. Allen
Saskatoon, Saskatchewan

PERMISSION TO USE

In presenting this thesis in partial fulfillment of the requirements for a Postgraduate degree from the University of Saskatchewan, I agree that the Libraries of this University may make it freely available for inspection. I further agree that permission for copying of this thesis in any manner, in whole or in part, for scholarly purposes may be granted by the professor or professors who supervised my thesis work or, in their absence, by the Head of the Department or the Dean of the College in which my thesis work was done. It is understood that any copying or publication or use of this thesis or parts thereof for financial gain shall not be allowed without my written permission. It is also understood that due recognition shall be given to me and to the University of Saskatchewan in any scholarly use which may be made of any material in my thesis.

Requests for permission to copy or to make other use of material in this thesis in whole or part should be addressed to:

Head of the Department of Electrical and Computer Engineering
University of Saskatchewan
Saskatoon, Canada, S7N 5A9

ACKNOWLEDGEMENTS

I would like to extend a very heartfelt thank you to my supervisor, Dr. S.O. Kasap, for his patience, guidance, and encouragement throughout the course of this work. I would also like to thank Dr. Robert Johanson and George Belev for their assistance with the construction and setup of the experimental system, as well as for taking the time to answer my many questions. I would like to thank Dancho Tonchev for making my samples to measure. I would also like to thank the University of Saskatchewan, Anrad, and NSERC for providing me with financial support. Last, but certainly not least, I would like to thank my family for their continuing support, encouragement and patience.

ABSTRACT

Time-of-Flight (TOF) and Interrupted-Field Time-of-Flight (IFTOF) measurements were performed repeatedly on several different samples of amorphous Selenium (a-Se) alloys as they aged from deposition or after annealing above the glass transition temperature (T_g) in order to examine the relaxation of the electrical properties. The mobility was found to relax slightly, but the relaxation did not fit well to a stretched exponential. The increase in the mobility for electrons was significantly more than the increase in mobility for holes in all sample compositions measured. For electrons, the mobility increased by 20-40%, whereas for holes, the mobility only increased by less than 10%. The relaxation of the lifetime, on the other hand, fit well to a stretched exponential. Furthermore, the overall increase in lifetime as it relaxed was much greater than the increase in the mobility. The average increase in lifetime was 85% for holes and 45% for electrons. The stretched exponential fits consisted of two important factors: the structural relaxation time τ_{sr} and the stretching factor β. For a given a-Se alloy, τ_{sr} was approximately the same for relaxation from both immediately after sample deposition, and annealing above T_g, indicating that the relaxation is readily repeatable and has the same physical origin. The relaxation was found to be dependent on the a-Se alloy composition. While the general shape of the relaxation was consistently a stretched exponential, τ_{sr} increased with increasing arsenic (As) concentration in the alloy, while β remained constant between 0.6-0.7. Additionally, τ_{sr} was found to be the same for both electron and hole relaxations for a given composition. Thus, the relaxation in both the electron and hole lifetime seems to be controlled by the same structural relaxation process, that is, the electron and hole traps are structural in origin.

TABLE OF CONTENTS

PERMISSION TO USE i
ACKNOWLEDGEMENTS ii
ABSTRACT iii
TABLE OF CONTENTS iv
LIST OF TABLES vi
LIST OF FIGURES vii
LIST OF ABBREVIATIONS xii
1. Digital Radiography and Amorphous Selenium 1
1.1 Introduction 1
1.2 Radiographic Imaging 3
1.3 a-Se as an X-ray Photoconductor 8
1.3.1 X-ray Absorption Coefficient 9
1.3.2 Electron-Hole Pair Creation Energy 10
1.3.3 Charge Transport and Schubweg 10
1.3.4 Ideal X-ray Photoconductor 11
1.4 Research Objectives 13
1.4.1 Transient Photoconductivity Experiments 13
1.4.2 Relaxation of the Carrier Transport Properties 14
1.5 Thesis Outline 14
2. Amorphous Selenium 16
2.1 Introduction 16
2.2 Structure of Amorphous Semiconductors 16
2.3 Band Theory for Amorphous Semiconductors 18
2.4 The Atomic Structure of Amorphous Selenium 20
2.5 Density of States of a-Se and Carrier Transport in a-Se 24
2.6 Optical Properties of a-Se 27
2.7 Summary 30
3. Time-of-Flight and Interrupted-Field Time-of-Flight Transient Photoconductivity 31
3.1 Introduction 31
3.2 The Time-of-Flight Measurement Technique 31
3.3 The Interrupted-Field Time-of-Flight Technique 38
3.4 Transient Trap Limited Theory 41
3.4.1 Monoenergetic Trap Level 41
3.4.1.1 Low Fields: Shallow Trap Controlled Transport 44
3.4.1.2 High Fields 46
3.4.2 Binary Trap Distribution 47
3.5 Summary 49

4. Experimental Procedure 51
4.1 Introduction 51
4.2 Sample Preparation 51
4.3 Charge Transport Measurements 54
4.4 TOF/IFTOF Experimental System 60
4.4.1 Overview 60
4.4.2 Pulse Generator 63
4.4.3 Xenon Flash 65
4.4.4 High Voltage Switch & Supply 67
4.4.5 Amplifier 70
4.4.6 Signal Capture and GUI 71
4.5 Annealing Chamber 73
4.6 Summary 75
5. Results and Discussion 76
5.1 Introduction 76
5.2 Measuring charge carrier transport properties in a-Se 76
5.3 The Relaxation of the Carrier Transport Properties in a-Se 85
5.3.1 Background 85
5.3.2 Technique 86
5.3.3 Results 88
5.4 Summary 104
6. Summary and Conclusions 106
6.1 Relaxation of the Electrical Properties of a-Se 107
6.2 Suggestions for Future Work 109
7. References 111
Appendix: Sensitivity Calculations 114

LIST OF TABLES

Table 2.1: Typical transport properties of stabilized a-Se (a-Se:0.2-0.5%As + 10-40ppm Cl) photoconductor films. 27

Table 5.1: Overall improvements in Mobility and "best" τ_{sr} and β for all samples used in this work 93

Table 5.2: Overall change in lifetime for all samples used in this work 100

Table 5.3: Change in sensitivity of a detector for mammography using a-Se over the course of the relaxation..... 102

Table 5.4: Change in sensitivity of a detector for general radiography using a-Se over the course of the relaxation..... 102

Table 5.5: Change in the total trap concentration in a-Se over the course of the relaxation. 103

LIST OF FIGURES

Figure 1.1: An image of a flat panel active matrix direct conversion X-ray image sensor [6]. 2

Figure 1.2: A simplified system used for x-ray imaging using a phosphorous screen and photographic film to capture the image. 4

Figure 1.3: A cross section of a pixel in a direct conversion x-ray detector using a-Se as a photoconductor. 6

Figure 1.4: A small section of a thin-film transistor active-matrix-array used in a direct conversion detector with self-scanning readout. 7

Figure 1.5: A sample x-ray image obtained from an a-Se direct conversion flat-panel x-ray detector [6]. 8

Figure 2.1: A two-dimensional representation of the of the atomic structure of (a) a crystalline semiconductor and (b) an amorphous semiconductor. Over-coordinated (O) and under-coordinated (U) defects are marked for the amorphous case. 17

Figure 2.2: Density of States (DOS) models for crystalline and amorphous semiconductors. (a) the crystalline case; two bands separated by a forbidden energy region. (b) initial DOS model for amorphous semiconductors; localized states encroach into the band gap. (c) The CFO model; the localized states extend all the way into the band gap and overlap. (d) Marshal and Owen model; structural defects create a large number of localized states deep in the band gap. From [11]. 19

Figure 2.3: The selenium chain model, demonstrating the dihedral angle, ϕ. It is best observed looking down the bond between atoms 2 & 3. The bond angle θ and the bond length r are also shown. 21

Figure 2.4: The random chain model of the structure a-Se. Certain regions are chainlike and others are ringlike. From [10]. 22

Figure 2.5: Structure and energy for different bonding configurations for Se atoms. Straight lines are bonding orbitals, lobes are lone-pair orbitals (non-bonding), and circles are anti-bonding orbitals. The energy of a lone pair is taken as the zero energy. Figure adapted from [18] 23

Figure 2.6: The a-Se structure with an IVAP defect, adapted from [10]. 24

Figure 2.7: Density of states function for a-Se as derived from experimental measurements [21]. 25

Figure 2.8: Absorption coefficient α (shown by solid line) and quantum efficiency η (shown by dashed lines) as a function of incident photon energy (hv) for various applied fields. 29

Figure 3.1: Schematic Diagram of the Time-of-Flight Measurement Technique..... 32

Figure 3.2: The motion of a charge, q, through a distance dx makes a charge, dQ, flow in the external circuit. 34

Figure 3.3: A simplified small signal AC equivalent circuit for the TOF experiment. C_s is the combination of the sample capacitance and any parasitics in the external electronics. 36

Figure 3.4: TOF transient signals for (a) I-mode and (b) V-mode. Solid lines are the case of sample with no traps, and the dashed lines represent a sample with deep traps..... 38

Figure 3.5: (a) Typical TOF waveform. (b) Typical IFTOF waveform. The magnitude of the photocurrent drops after the interruption due to carriers being trapped. 40

Figure 3.6: Current flow of holes in a semiconductor involving trapping and release within a slice, dx. 42

Figure 3.7: Comparison the I-mode signals for the trap free drift mobility and shallow trap controlled models. 45

Figure 3.8: Diagram of the photocurrent in the high fields model. 47

Figure 4.1: Schematic diagram of the NRC 3117 vacuum deposition system used to make the samples in this study. From [11]. 52

Figure 4.2: Schematic diagram of the Hummer VI sputtering system used to generate contacts on the a-Se samples. From [11]. 53

Figure 4.3: A briefly simplified schematic of a system for transient photoconductivity measurements. The voltage supply V will supply constant or pulsed bias for TOF and IFTOF measurements respectively. The oscilloscope is synchronized with the light source in order to effectively capture the transient photocurrent signal. 55

Figure 4.4: Typical timing and resulting transient photocurrent for drifting holes for (a) TOF experiment and (b) IFTOF experiment. The hole drift mobility is found using the transit time of the TOF transient. The hole lifetime is found from the ratio of the recovered photocurrent to the initial photocurrent after an interruption time t_i in the IFTOF transient..... 56

Figure 4.5: The rapid switching of the HV Bias generates a large displacement current that must be dealt with for the IFTOF technique to work properly. 59

Figure 4.6: A grounded bridge network to eliminate the large displacement currents caused by switching the high voltage in IFTOF measurements. 60

Figure 4.7: The TOF/IFTOF system used in the experiments. The system uses an internal HV supply and a grounded bridge network to reduce

switching transients. Timing for the experiment is controlled by the computer and the transient response is recorded onto a connected TDS210 oscilloscope. 61

Figure 4.8: Typical displacement current free IFTOF signal for holes after the digital subtraction has been performed. This sample was a-Se:0.5% As with a thickness of 105 μm. 63

Figure 4.9: The pulse generator circuit used to interface the PCI-CTR05 timer board and the IFTOF apparatus. 64

Figure 4.10: Timing of Pulses using in a typical IFTOF experiment, manual control switch is set to "Pulsed" 65

Figure 4.11: Schematic sketch of the xenon flash circuit. 66

Figure 4.12: Optical system used to filter and focus the light pulse from the xenon pulse. The resulting blue light pulse is transferred to the TOF/IFTOF system by way of a fiber optic cable. 67

Figure 4.13: A high voltage supply capable of delivering 2KV 68

Figure 4.14: A high voltage switch capable of switching 1KV 69

Figure 4.15: A two-stage differential amplifier with 16dB of gain. 70

Figure 4.16: A circuit to generate a delay to control the application of the amplifier protection. The circuit is shown in (a), the timing diagram is shown in (b). Adjusting the 50k potentiometer controls the delay, t_s. 71

Figure 4.17: Graphical user interface (GUI) used to control the TOF/IFTOF experiment. 72

Figure 4.18: Typical Temperature Curve for an Annealing Experiment 74

Figure 4.19: Annealing chamber used to anneal samples for relaxation. The water-cooling lines are actually interspersed inside the copper sample platform..... 74

Figure 5.1: Fractional recovered photocurrent as it varies with resting time between IFTOF firings. t = 0 corresponds with the initial measurement on a fully rested sample. 78

Figure 5.2: I-mode waveforms for samples of a-Se:0.5% As. (a) Hole waveform captured with an applied field of 1 V/μm with a thickness of 105 μm; transit time was measured to be 8.5 μs. (b) Electron waveform captured with an applied field of 1.93 V/μm with a thickness of 86 μm; transit time was measured to be 228.2 μs. 79

Figure 5.3: IFTOF waveforms for samples of a-Se:0.5% As. (a) Hole IFTOF waveform with interruption time of 20 μs. (b) Electron IFTOF waveform with interruption time of 200 μs. 81

Figure 5.4: Semilogarithmic plots of fractional recovered photocurrent i_2/i_1 vs. interruption time for samples of a-Se:0.5% As. (a) The resulting

hole lifetime, τ_h, was 19.9 ± .8 μs. (b) The resulting electron lifetime, τ_e, was 375 ± 10 μs. 82

Figure 5.5: Semilogarithmic plots of i_2/i_1 vs. t_i for different samples with varying hole lifetimes. The exponential fit remains applicable for all hole lifetimes. 83

Figure 5.6: Semilogarithmic plots of i_2/i_1 vs. t_i for different samples with varying electron lifetimes. The exponential fit remains applicable for all electron lifetimes. 83

Figure 5.7: Semilogarithmic plot of i_2/i_1 vs. t_i/τ for holes. The high R^2 value indicates that the hole lifetime follows an exponential dependence. 84

Figure 5.8: Semilogarithmic plot of i_2/i_1 vs. t_i/τ for electrons. The high R^2 value indicates that the electron lifetime follows an exponential dependence. 84

Figure 5.9: Enthalpy vs. temperature for a-Se. Once a sample is heated or fabricated above T_g and cooled to room temperature, it is at state G. From there it relaxes towards the equilibrium steady state at A. By heating the sample up from state A above T_g, the process can be repeated. 87

Figure 5.10: Change in the electron TOF waveform as the relaxation experiment progresses in a sample of a-Se:0.2% As. 89

Figure 5.11: Change in the hole TOF waveform as the relaxation experiment progresses in a sample of a-Se:0.2% As. 90

Figure 5.12: Relaxation of the mobility of electrons and holes in samples of a-Se:0.3% As + 5ppm Cl. 91

Figure 5.13: Comparison of different fitting parameters on the electron mobility fit. 92

Figure 5.14: Adjusted sample thickness vs. time. 94

Figure 5.15: Electron mobility relaxation taking into account changing sample thickness. 95

Figure 5.16: Relaxation of the lifetime of electrons and holes in samples of a-Se:0.2% As. 96

Figure 5.17: Comparison of different fitting parameters. Effects of changing τ_{sr} and β on the curve fits. 96

Figure 5.18: Relxation of the lifetime of electrons of a sample of a-Se:0.2% As from both depostition and annealing. τ_{sr} =15.7 h for the deposition measurements and τ_{sr} = 14.6 h for the annealing measurement. 97

Figure 5.19: Relaxation of the lifetime of electrons and holes in samples of pure a-Se. 98

Figure 5.20: Structural relaxation time, τ_{sr}, for the lifetimes of the samples of various compositions measured in this work. 99

Figure A.1: Schematic diagram of a photoconductor sandwiched between two metal plates as electrodes. From [i]. 115

Figure A.2: Plot of the mass energy absorption coefficient (α_{air}) vs. incident x-ray photon energy for air. 119

Figure A.3: Plot of the mass energy absorption coefficient (α_{en}) and linear attenuation coefficient (α) vs. incident x-ray photon energy for Se. 120

LIST OF ABBREVIATIONS

a-Se	amorphous selenium
a-Si:H	hyrdogenated amorphous silicon
AMA	active matrix array
CCD	charge coupled device
CFO	density of states model proposed by Cohen, Fritsche and Ovshinski
CMOS	complementary metal oxide semiconductor
CMRR	common mode rejection ratio
DOS	density of states
DPDT	double pole double throw
EHP	electron hole pair
ESR	electron spin resonance
GUI	graphical user interface
HEXFET	hexagonal shaped MOSFET
HV	high voltage
IFTOF	interrupted-field time-of-flight
IVAP	intimate valence alternation pair
MOSFET	metal oxide field effect transistor
NSB	normal structure bonding
PC	personal computer
PCI	peripheral component interconnect
PID	proportional with integral and derivative control
PPM	parts per million
SCR	silicon controlled rectifier
SNR	signal to noise ratio
SPDT	single pole double throw
TFT	thin film transistor
TOF	time-of-flight
VAP	valence alternation pair

1. Digital Radiography and Amorphous Selenium

1.1 Introduction

Radiography, in the form of x-ray imaging, is one of the most widespread diagnostic tools for medical treatments around the world. Currently, the most prevalent radiography uses a film emulsion to capture the optical response when x-rays passing through a patient collide with a phosphor screen. The film and phosphor screen are packaged together in an x-ray cassette that is inserted into the x-ray system manually by an x-ray technician. Each x-ray cassette is only good for one exposure; it must be manually replaced for each new image the operator wishes to take. Once exposed, each film must be taken to a separate room for the film to be developed into a visible image. The developed film prints are quite bulky, making them difficult to transport and store.

Even though this system has worked well since its inception in the 1890s, there are advantages to switching from this largely analog system to a digital system [1]. A fully digital system could adjust the intensity of the x-ray source in order to achieve a good image, while still minimizing patient exposure, far more accurately than current trial-and-error methods. The use of digital images has widespread applications. Computer software can be used to enhance the image quality [2], allowing for a more accurate diagnosis. Digital images can also easily be transferred from one location to another [3], allowing for doctors to receive test results quicker, as well as allowing for remote diagnosis. Furthermore, a digital image takes almost no space, making image storage easier.

Direct conversion flat panel x-ray detectors have recently become commercialized for digital radiography [4]. These detectors replace the traditional film and phosphor screen with a large area integrated circuit known as an active matrix array (AMA) coated with an x-ray photoconductive material. The photoconductor directly converts incident x-rays into electronic charges that are then stored in charge collection capacitors in each

element of the AMA. The stored charges can be read out one at a time by activating the thin film transistors in proper order. Thus, the readout of the image charge is digitized and can be sent to a computer for processing and display. The materials and electronics in these flat-panel detectors are compact enough that they can be fit into an existing film imaging system. Furthermore, these detectors have the potential to generate higher quality images with less patient x-ray exposure [5].

Figure 1.1: An image of a flat panel active matrix direct conversion X-ray image sensor [6].

Amorphous Selenium (a-Se) is currently being used as an x-ray photoconductor for these flat panel x-ray detectors. Like other potential x-ray photoconductors, a-Se can easily be fabricated into a large-size uniform layer to cover the AMA electronics. However, a-Se has a relatively low dark current compared to other candidates [7]. The electrical properties of the photoconductive layer of a-Se vary with alloy composition. These properties, such as charge carrier drift mobility and deep trapping time (lifetime), directly control the overall performance of any detector. Therefore, continued studies of a-Se and its alloys are important in order to build better x-ray photodetectors.

The first objective of this work was to develop an experimental system capable of performing Time-of-Flight (TOF) and Interrupted-Field Time-of-Flight (IFTOF) transient

photoconductivity measurements. These measurements measure the transient response that occurs when a short pulse of light injects carriers into a biased sample. The TOF measurement examines the transit time of the injected carriers as they travel through the sample to determine the carrier drift mobility, μ. The IFTOF experiment uses the fractional change in photocurrent caused by an interruption of the bias voltage while the carriers are travelling through the sample to determine the deep trapping time (lifetime), τ. The mobility (μ) and lifetime (τ) found in the TOF and IFTOF experiments are extremely important for device performance as their product, $\mu\tau$, is directly related to the sensitivity of the photodetector [7].

With a working TOF/IFTOF system in place, the system was then used to examine the relaxation of the electrical properties of a-Se alloys from fabrication or annealing until they reached steady state. From the time the samples are deposited, or immediately after they are annealed, the electrical properties of the a-Se change considerably. Since the sensitivity of a photodetector is directly related to its electrical properties, the performance of a detector with a-Se as a photoconductor will also be affected, making the study of the relaxation effects very important.

1.2 Radiographic Imaging

Radiographic imaging works by measuring the amount of x-ray radiation that has passed through an object. X-rays are attenuated differently depending on what they pass through, bones and different body tissues will have different amounts of attenuation on the incident x-rays. When the attenuated x-rays are converted into a visible image, the difference in attenuation shows up in the subsequent image. For example, bone tissues tend to absorb more incident x-rays, so will show up darker on the subsequent image. Conversely, soft tissues like fat and muscle will appear whiter on the image since they do not absorb many x-rays.

A typical system used for x-ray imaging is shown in Figure 1.2. In this typical system, the x-rays are emitted from an x-ray source and passed through the object being x-rayed. As the x-rays pass through the object, they are attenuated depending on what they are passing through; the x-ray detector captures the intensity of the x-rays that pass through the object. The requirements of the x-ray detector vary depending on what is being observed. For chest x-rays, a detector needs a large dynamic range to capture the large intensity difference between the bones and the softer tissues in the chest, as well as being large enough to capture the full area being imaged. For mammography, there are far more stringent requirements on the detector in order to see the difference between normal cells and cancerous cells, which are both soft tissues. In the most common detectors used presently, the detector consists of a cassette of a photographic film and a phosphorus screen.

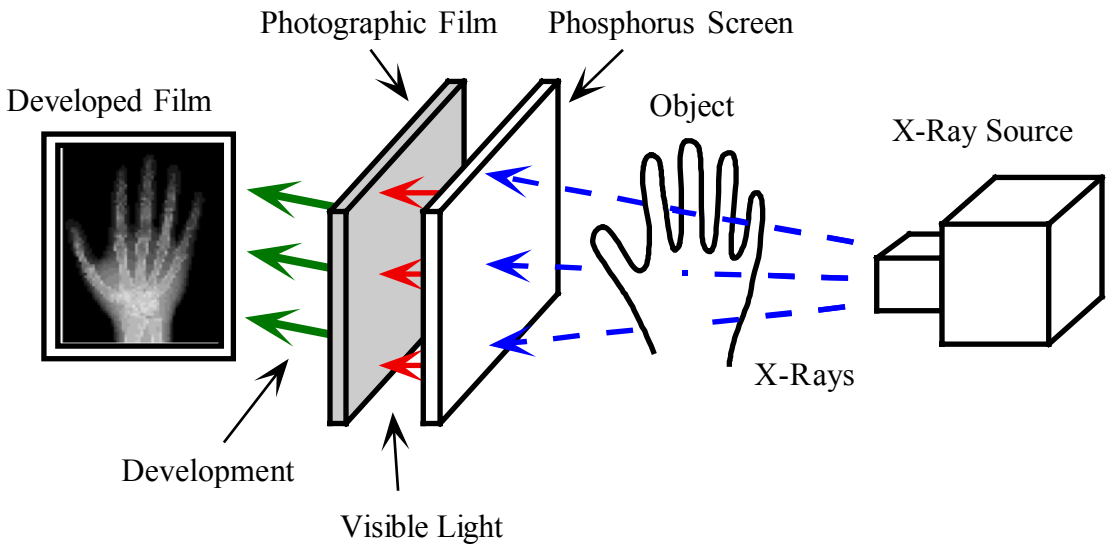

Figure 1.2: A simplified system used for x-ray imaging using a phosphorous screen and photographic film to capture the image.

To obtain a digital x-ray image, the incident x-ray photons must be eventually converted into an electronic signal. There are two methods to do this: indirect conversion and direct conversion. Indirect conversion is similar to the standard analog x-ray film used today; the x-ray photons strike a phosphor screen, which converts the x-rays into visible light. The visible light is then collected and converted to an electronic signal with the use of a silicon photodiode or CCD camera. In a direct conversion detector, the

phosphor screen is completely omitted; the detector itself converts the x-rays directly into an electronic signal. For direct conversion, an x-ray sensitive photoconductive material is used to absorb incoming x-rays to generate electron-hole pairs. If a biasing potential is applied to the material, the electron-hole pairs (EHPs) will separate and drift to opposite electrodes on the material. The amount of charge collected at the electrodes will be proportional to the exposure (intensity × duration) of the incident x-rays, and this is quite easily measured electronically.

Direct conversion detectors have several advantages over indirect conversion detectors. Direct conversion detectors have a greater inherent resolution than indirect; the x-ray generated charges can only drift in the direction of the applied bias, set to be perpendicular to the image plane. Thus, lateral spread of the x-ray image is heavily reduced. The image the electronics read out will be the same as the image from the absorbed x-rays. In an indirect photodetector, the light in the thick phosphorous layers needed to absorb the incident x-rays spreads out, reducing the resultant image resolution [1]. Another advantage of a direct conversion detector is the sensitivity of the detector can be increased with careful selection of the photoconductor material. Furthermore, the sensitivity of a particular photoconductor can be maximized with careful balance of the applied bias and photoconductor thickness [8]. In an indirect converter, the phosphor screen limits the x-ray sensitivity of the system.

A direct conversion digital flat-panel x-ray detector has recently been developed using a-Se as a photodetector [1]. This technology is based on the amorphous silicon (a-Si:H) AMA device for displays. In an AMA circuit, a display is split into discrete picture-producing elements, also know as pixels, that are placed into and M x N array, with M and N being the number of elements in each direction. Each pixel contains a small charge capacitor and a thin-film-transistor (TFT) switch. For a direct conversion x-ray detector, a layer of a-Se, ~1 mm thick is coated onto the surface of the AMA. After the deposition of the a-Se, a top contact is evaporated on the photoconductor in order to apply a bias. A cross section of an individual pixel is shown in Figure 1.3. During an x-ray imaging, the x-ray photons that pass through the patient will travel into the a-Se

photoconductor and generate electron-hole pairs; the number of EHPs generated will be proportional to the number of x-ray photons (i.e. the exposure). Under the applied field, the EHPs will separate; the electrons will travel to the top electrode to be collected by the battery, while the holes will travel to the bottom electrode to be collected and stored by the pixel capacitor C_{ij}. The total positive charge signal (Δq_{ij}) collected by the capacitor will be determined by the number of holes collected, and therefore, dependent on the intensity of the radiation in the pixel area.

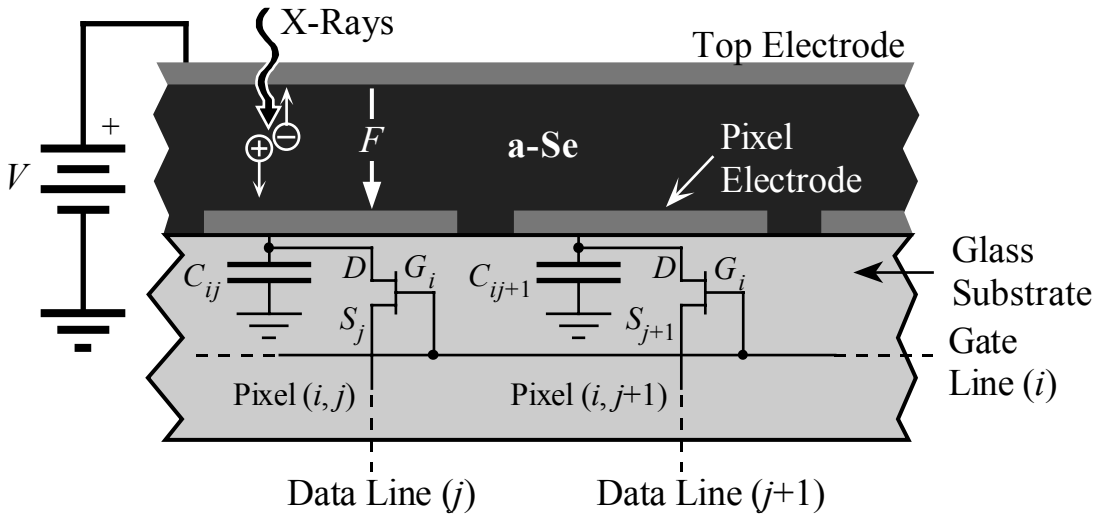

Figure 1.3: A cross section of a pixel in a direct conversion x-ray detector using a-Se as a photoconductor.

Each pixel stores the part of the x-ray image that occurs in its range. The total x-ray image can be found by examining all the charges in all the pixels in the AMA. The image can be read from the AMA by carefully coordinating the activation of the TFTs in the array. A small section of an M x N AMA is shown in Figure 1.4. The gate terminals of each TFT in a row is connected by a control line, i. Similarly, the source terminals in a column of TFTs are all connected by a data line, j. To read out the x-ray image from the AMA, control line i is activated, turning the TFTs in that row on. With the entire row on, the stored charge in the capacitors is passed onto the data lines, which are read from the N columns in the AMA. The data is processed and sent to the computer, before the process is continued onto the next row in the AMA. This continues until all the rows have been activated, thereby transferring the entire image to the computer.

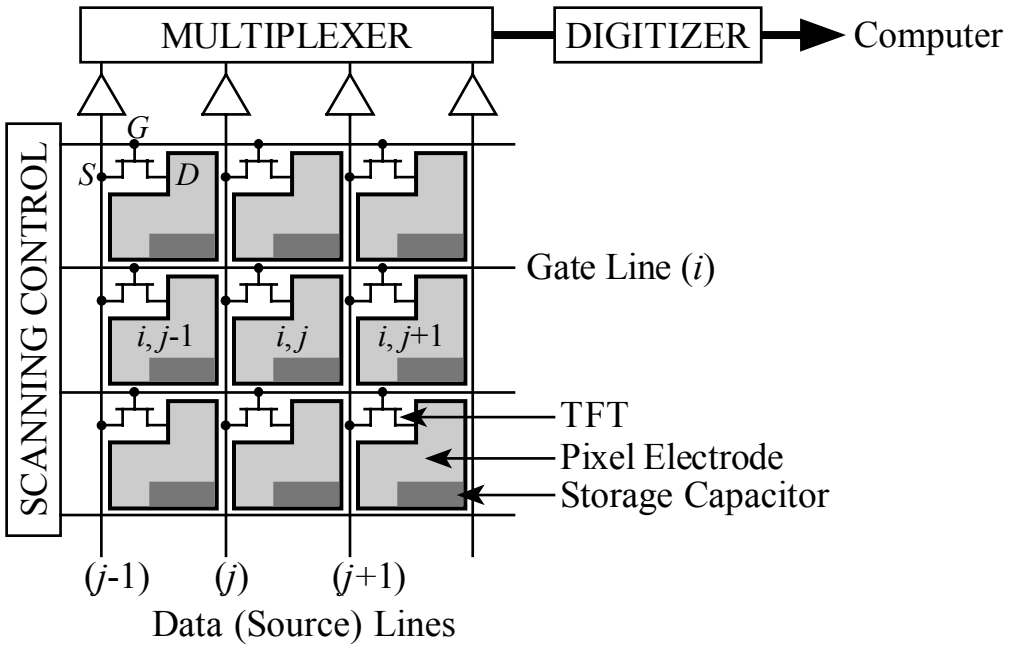

Figure 1.4: A small section of a thin-film transistor active-matrix-array used in a direct conversion detector with self-scanning readout.

These flat panel detectors with an AMA using a-Se as an x-ray photoconductor are self-scanning and can produce good images for general x-ray imaging. An x-ray image taken using an a-Se flat panel x-ray detector is shown in Figure 1.5. Since the flat panel detector contains all the electronics needed to generate the image, they are quite compact and do not require adjustment after every image like the x-ray film systems currently in use. The resolution of these flat panel detectors is based on the pixel size of the AMA. Currently, pixel sizes of ~150 μm are available, which is suitable for chest radiographic imaging. Research is being done, however, to decrease the pixel size in order to achieve the resolution needed for mammography, which would require a pixel size ~50 μm [7].

Figure 1.5: A sample x-ray image obtained from an a-Se direct conversion flat-panel x-ray detector [6].

1.3 a-Se as an X-ray Photoconductor

The sensitivity of a direct conversion flat panel detector is determined by the amount of charge generated per unit of radiation. Three properties are especially important for the sensitivity: the absorption coefficient, the electron-hole pair creation

energy, and the charge transport properties of the material: the mobility and lifetime. These properties are described in this section, followed by a description of an ideal x-ray photoconductor material.

1.3.1 X-ray Absorption Coefficient

The absorption coefficient, α, gives the number of photons that are absorbed by a photoconductor by the photoelectric effect. The fraction of absorbed photons is given by:

$$A_Q(E) = [1 - \exp(-\alpha L)] \quad (1.1)$$

where L is the thickness of the detector, and $\alpha = \alpha(E, Z, d)$ is the absorption coefficient of the material. The absorption coefficient depends on the energy of the incident x-rays E, the atomic number Z, and the density of the photoconductor d.

The detector thickness is related to the absorption coefficient. In order to get the best image quality while minimizing the patient exposure, as much of the incident x-rays must be absorbed in the photodetector material as possible. The absorption depth, $\delta = 1/\alpha$, gives the thickness of photoconductor needed in order to absorb 63% of the incident x-rays. Thus, to absorb as much x-rays as possible, the detector thickness should be greater than the absorption depth, $L > \delta$. For example, in mammography, the x-rays have an average energy of 20 keV. If the minimum detector thickness is specified at 2δ, then the thickness of a-Se needed will be about 200 μm.

The ideal detector would therefore be as thick as possible, if it was not limited by several factors. First, it is very difficult and expensive to deposit the photoconductor onto the AMA with large thicknesses while still maintaining the uniformity and preventing defects from occurring [6]. Secondly, the operating bias needed for device operation also increases with increasing thickness. If 10V/μm is required as a bias voltage, a detector with a thickness of 1000 μm would require 10kV of bias, high enough to create technological problems, such as dielectric breakdown in the panel, and difficulty protecting the AMA. Finally, as the thickness of the photodetector increases, so does the probability that the electrical charges will be lost to trapping while they are moving

through the photoconductor. The *schubweg* in a photoconductor determines how far on average the generated electrical carriers will travel before being trapped, and is discussed shortly.

1.3.2 Electron-Hole Pair Creation Energy

When an x-ray photon is absorbed in a photoconductor, it generates a highly energetic electron. As the electron moves through the material, it collides with other atoms and generates many electron-hole pairs. Thus, one x-ray photon generates multiple electron-hole pairs in the photoconductor. The amount of charge generated ΔQ from the absorption of x-ray energy ΔE is given by

$$\Delta Q = \frac{e\Delta E}{W_{\pm}} \tag{1.2}$$

where $W_{\pm}$ is the electron-hole pair creation energy, the amount of radiation energy that must be absorbed to generate a single electron-hole pair. $W_{\pm}$ has been shown to be related to the energy of the mobility gap (E_g) in amorphous semiconductors by $2.2E_g + E_{phonon}$ [9]. $W_{\pm}$ has also been shown to have some dependence on the electric field, but the exact nature is still being investigated [6]. For a-Se, $W_{\pm}$ at a given x-ray energy E decreases with increasing electric field F, and can be approximated by

$$W_{\pm} \approx W_{\pm}^{o} + \frac{B}{F} \tag{1.3}$$

where $W_{\pm}^{o}$ is the saturated EHP creation energy (at infinite applied field) and B is a constant that depends on the x-ray photon energy.

1.3.3 Charge Transport and Schubweg

In order for a direct conversion detector to function, the charges generated when an x-ray is absorbed must be collected. When an electron is generated, it moves towards the storage capacitance with a velocity determined by the electron's mobility (μ) in the photoconductor, as well as the applied field. Unfortunately, in a-Se, as well as in many

other photoconductive materials, there is a concentration of electron and hole traps. If a carrier is captured by one of these traps, it is essentially lost, as the carrier cannot move from the trap to reach the collection electrode. Thus, some generated charges are captured and do not contribute to the resulting image signal, decreasing the sensitivity of the detector. The carrier trapping time (lifetime), τ, gives the average amount of time a carrier can travel in the semiconductor without being captured by one of the deep traps.

The product of the mobility, lifetime, and applied field (F) is known as the carrier *schubweg*. The schubweg, $\mu\tau F$, gives the average distance a generated carrier will travel without becoming trapped. Therefore, for an ideal performance in a photodetector, the photoconductive material should have a thickness (L) that is much less than the schubweg, i.e. $\mu\tau F >> L$. This conflicts with the requirements for ideal x-ray absorption, mentioned before, which desire a photoconductive layer that is as thick as possible in order to absorb as many x-rays as possible. Thus, the thickness of the photoconductor must be carefully selected for desired performance with $1/\alpha < L < \mu\tau F$. Though thicker layers (for better absorption) with large applied fields (to increase the schubweg) could be used, this also increases the dark current of the photoconductor, decreasing the overall signal-to-noise ratio (SNR) of the detector, as well as causing other problems mentioned previously.

1.3.4 Ideal X-ray Photoconductor

The performance of any direct conversion detector is directly related to the performance of the selected photoconductor. An ideal photoconductive material can be described as follows.

1) X-ray absorption must be as high as possible. Any x-rays that are not absorbed by the detector are wasted. The higher the absorption, the lower the amount of x-rays a patient needs to be exposed to in order to generate comparable images.

2) The photoconductor should have a low value for the EHP creation energy ($W_{\pm}$). This will enable the generation of as much electrical charge for each incident x-ray photon as possible.
3) The dark current of the photoconductor should be minimal in order to generate the best SNR. Using a material with a larger band gap (E_g) and using non-injecting contacts can help reduce the dark current. A larger E_g, however, means that $W_{\pm}$ will increase, creating a conflict with 2).
4) Generated EHPs should not recombine in the bulk of the photoconductor. Since the rate of recombination is proportional to the amount of generated charges, this will be mostly negligible as long as there is not too much x-ray exposure.
5) The deep trapping within the photoconductor should be minimal. Therefore, the schubweg should be much greater than the photoconductor thickness, i.e. $\mu\tau F >> L$.
6) The longest transit time of the generated carriers should be shorter than the access time for a pixel.
7) The properties of the photoconductor should not deteriorate under repetitive exposure to x-rays.
8) The photoconductor should be able to coat onto a large area AMA circuit without damaging the circuitry. For example, annealing the photoconductor at temperatures above 300 ºC can damage a-Si:H TFTs. Large detector area is required because there is no practical method to focus x-rays.

a-Se is a good choice for the photodetector for direct-conversion detectors. a-Se can be easily coated onto an AMA panel using conventional vacuum deposition techniques. The substrate temperature during the deposition is only around 60-70 ºC, which will not damage the TFTs in the AMA. As a photodetector, a-Se has good electron and hole transport properties (given by $\mu\tau F$), acceptable x-ray absorption, and a low dark current. a-Se has also been well studied over time so information on its electronic and physical properties is readily available [10].

1.4 Research Objectives

This research focuses on the charge transport properties of various alloys of a-Se that could be used as a photodetector in a flat-panel detector. Specifically, the mobility (μ) and lifetime (τ) will be measured. These properties are of importance to any photoconductor as they determine the schubweg of the material, and thus directly affect the sensitivity of any detector. These properties must be able to be measured easily and accurately, otherwise the validity of the results could be questioned.

1.4.1 Transient Photoconductivity Experiments

The charge transport properties of the a-Se alloys in this work will be measured using time-of-flight (TOF) and interrupted-field time-of-flight (IFTOF) transient photoconductivity measurements. The TOF technique has been used for many years to measure the drift mobility of carriers in materials such as a-Se. In this technique, a short pulse of light injects carriers into a biased sample. One of the carriers will drift through the sample, generating a transient photocurrent in external circuitry that can be readily measured. This photocurrent can be used to calculate the mobility of the carriers in the sample. The IFTOF technique works on a similar principle, though the measurements are performed by removing the applied bias, interrupting the drift of the photoinjected carriers. When the bias is re-applied, the drift of the carriers resumes though some will be captured by the deep traps located within the sample. The deep trapping lifetime can be found by examining the dependence of the recovered photocurrent signal vs. the interruption time.

The first goal in this work was to build an experimental apparatus capable of performing both TOF and IFTOF measurements. The actual implementation of the IFTOF technique is particularly difficult due to the large switching transients created by switching the bias voltage on and off. This switching transient can completely dwarf the transient photoconductivity signal being measured, so eliminating the switching transient is important. This is done with the use of a balanced bridge network and transient

suppressing rectifiers. The theory involved with the TOF and IFTOF techniques is described in Chapter 3, and a detailed description of the experimental apparatus used in this work is presented in Chapter 4.

1.4.2 Relaxation of the Carrier Transport Properties

a-Se is a typical glass, and thus exhibits typical glass relaxation. The properties of a-Se will change over time (relax) from an initial state when it is fabricated (or annealed above the glass transition temperature, T_g) until the properties reach a steady state value. Changes in the mobility and lifetime, and thus the schubweg, could have a large effect on the performance of a detector; a brand new detector may not function at all until the a-Se photoconductive layer has been given sufficient time to relax after being deposited. Furthermore, if the temperature of the photodetector ever rises to a temperature above T_g, for example during shipping, the detector would need a certain amount of time to recover its properties.

This relaxation of electrical properties has been observed before, but never precisely examined. Thus, a technique to examine the relaxation as it occurs had to be developed. This technique used repeated TOF and IFTOF measurements to determine the mobility and lifetime of an individual sample at specific intervals. The shape of relaxation can be observed by looking at the overall change in mobility and lifetime as it relaxes from its initial state to steady state. This process was repeated for different alloys of a-Se to determine the effects of alloy composition on the relaxation. With many different alloys measured, the relaxation of all the alloys was compared to see if any patterns emerged.

1.5 Thesis Outline

This chapter provided an outline of digital radiography as well as the implementation of direct-conversion flat panel detectors. These detectors use an x-ray

sensitive photodetector, such as a-Se, to directly convert incident x-rays into electrical charge, which is collected and read out using a TFT AMA. Detectors like this are compact, self-scanning, and produce high-quality digital x-ray images. Research into materials to be used as x-ray photodetectors is therefore highly desired in order to maximize the performance of these flat panel detectors. a-Se is currently the best photodetector material due to its ability to be coated onto large-area AMAs safely, good x-ray sensitivity, small dark current, and good transport properties.

The rest of the thesis is presented in 5 chapters. In Chapter 2, the nature of a-Se is described and a band model for a-Se is derived to help explain the electronic properties of a-Se and its alloys. In Chapter 3, the theory behind the TOF and IFTOF techniques is described, as well as the derivation of several theoretical expressions for the TOF transient photocurrent. In Chapter 4, the experimental apparatus used in this work is described, as well as a brief description of the methodology used to create the a-Se samples used in this work. In Chapter 5, the results and discussion from the measurements of the relaxation of the electrical properties of the a-Se alloys in this work are presented. Finally, in Chapter 6 the conclusions from the experimental work are presented as well as suggestions for future work.

2. Amorphous Selenium

2.1 Introduction

Amorphous Selenium (a-Se) was initially studied to improve its performance in xerography in the early 1960s and 1970s. Recently, much interest has emerged due to the use of a-Se as a photoconductor in flat-panel x-ray imaging detectors. Not only can a-Se be easily deposited over large surface areas, but it also allows for direct conversion of x-ray photons into electronic charge. The optical and electronic properties of a-Se can significantly affect the performance of any device using it as a photoconductor. It is therefore important to understand its properties and learn how these properties can be modified.

The band theory for solids provides a good theoretical base from which to understand the properties of a-Se. In a crystalline solid, the periodicity of the crystal leads to an easy derivation for a band model to help determine the electronic and optical properties of the solid. However, the disorder of an amorphous semiconductor makes the derivation of an exact model extremely difficult. Nevertheless, a band model for amorphous semiconductors can be found through noting the similarities to crystalline semiconductors, as well as using experimental observations.

2.2 Structure of Amorphous Semiconductors

Amorphous semiconductors are quite different from crystalline materials. Figure 2.1 shows the bonding arrangements for crystalline and amorphous semiconductors. The dots in the figure represent the equilibrium position in the crystal in which the individual atoms will oscillate. The lines between the dots represent the bonds between the atoms and its nearest neighbours. The crystalline structure is shown in Figure 2.1 (a). The crystalline structure is characterized by a highly ordered arrangement of atoms; each atom has the same number of bonds (or coordination number), the bond lengths are all

the same, and the bond angles are the same between all atoms. This order carries throughout the crystal and therefore, if the surface states are ignored, the equilibrium position of any atom in the crystal can be determined from any other position in the network. This is known as long-range order because the periodicity of the network is applicable throughout the bulk of the solid.

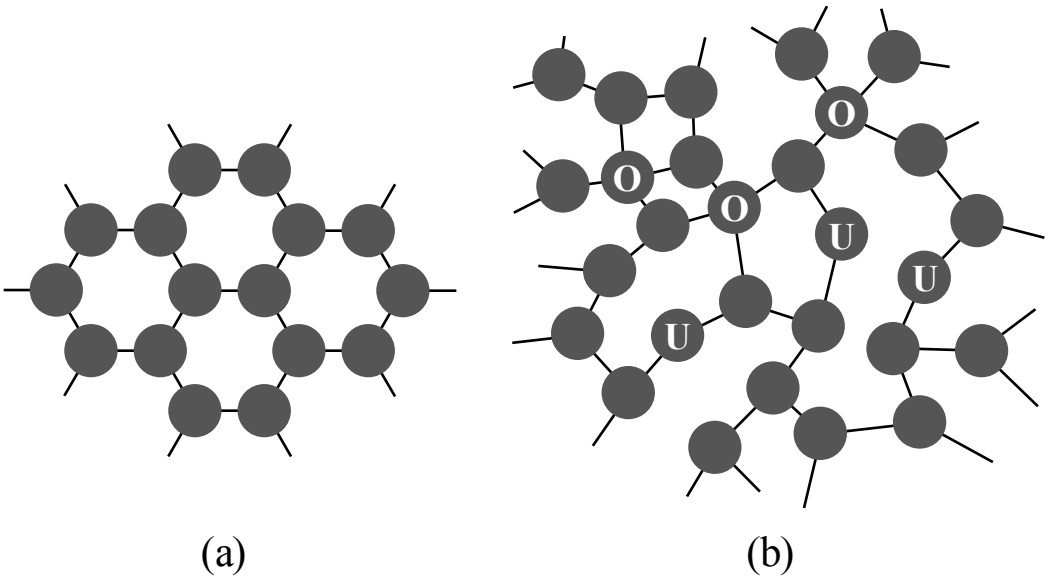

Figure 2.1: A two-dimensional representation of the of the atomic structure of (a) a crystalline semiconductor and (b) an amorphous semiconductor. Over-coordinated (O) and under-coordinated (U) defects are marked for the amorphous case.

An amorphous semiconductor, shown in Figure 2.1 (b), is far more complicated than the crystalline case. Slight variations in the bond lengths and angles eliminate any periodicity for distances greater than a few atomic radii. On the other hand, amorphous semiconductors do exhibit some short-range order; each atom still maintains its normal valency requirements, resulting in a similar electronic structure in the amorphous phase as for the crystalline phase. The overall disorder in an amorphous semiconductor also generates various localized electronic states. The energy location and density of these localized states can significantly affect the electronic and optical properties of amorphous semiconductors.

Both crystalline and amorphous semiconductors contain defects. In the crystalline case, a defect is simply an atom that is out of its equilibrium position. In the amorphous case, this cannot apply due to the random nature of the bond length and angle. The only aspect in the amorphous case that is constant is the number of bonds, often referred to as the normal structure bonding (NSB) of the atom. A defect in amorphous semiconductors is therefore any atom with a different number of bonds. In Figure 2.1 (b), each atom normally has 3 bonds each, but there are several over-coordinated atoms, containing 4 bonds each, and under-coordinated atoms, with only 2 bonds each. These defects affect the electronic structure of the semiconductor by generating localized electronic states in the semiconductor.

2.3 Band Theory for Amorphous Semiconductors

Band models are commonly used to explain the electronic and optical properties of semiconductors. In a system with a single atom, quantum theory states that the energy of the electron is quantized at discrete levels or states. When several atoms are brought together to form a solid, the individual electron energy states combine in a way to form almost continuous bands of allowable energy states. These band states make up the density of states for a material, $g(E)$, which defines the number of electron states per unit energy per unit volume at an energy E.

The density of states for crystalline semiconductors is shown in Figure 2.2 (a). Its derivation involves using simplifications from the periodicity of the crystalline structure. It contains 2 bands of allowed energies, separated by a gap of forbidden energy states known as the *bandgap*. The lower band is filled with electrons and is known as the valence band; the upper band is mostly devoid of electrons and is known as the conduction band. The edges of the bands are denoted as E_V and E_C for the valence band and conduction band respectively, E_F is the Fermi Level.

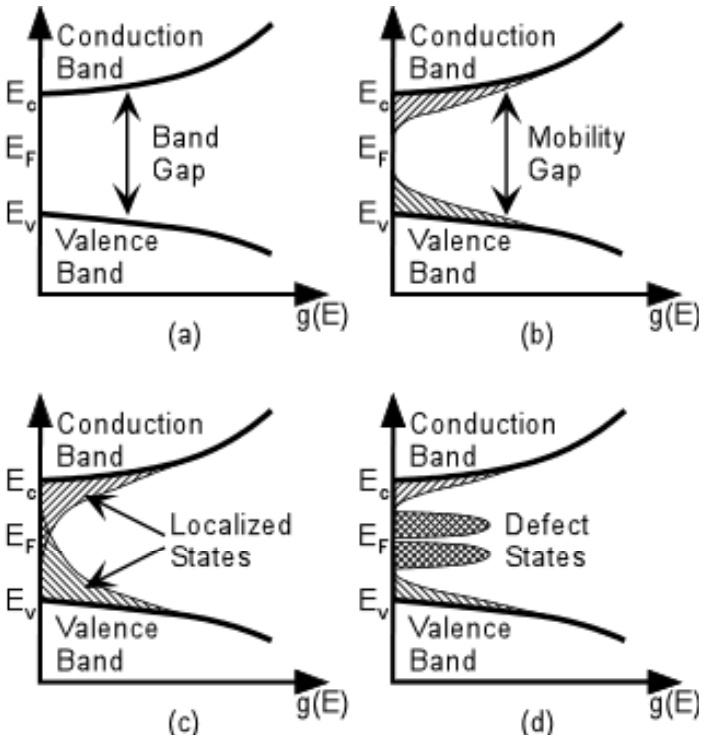

Figure 2.2: Density of States (DOS) models for crystalline and amorphous semiconductors. (a) the crystalline case; two bands separated by a forbidden energy region. (b) initial DOS model for amorphous semiconductors; localized states encroach into the band gap. (c) The CFO model; the localized states extend all the way into the band gap and overlap. (d) Marshal and Owen model; structural defects create a large number of localized states deep in the band gap. From [11].

The development of a density of states model for amorphous semiconductors is far more difficult due to the lack of long-range order. Because of this, several band models have been proposed over the years. The first was proposed by N. F. Mott [12]. Mott hypothesised that the sharp band edges in the crystalline model were due to the long-range order within the material. Since amorphous semiconductors only have short-range order, instead of the sharp edged bands of the crystalline materials, the amorphous materials would have bands with tails of localized states that would enter into the bandgap. This is shown in Figure 2.2 (b). The tails begin at the band edges E_V and E_C and trail off into the forbidden gap. Mott also argued that the transition from the tail of localized states to the extended band states was well defined, corresponding to a sharp increase in mobility where the extended band states began. Electrons in the tail of localized states move with mobility controlled by thermally activated tunnelling between states, while electrons in the extended band states would move with a mobility

determined by the electron's effective mass in the solid and scattering from potential fluctuations due to the randomness in the structure. The transition in the mobility leads to the concept of a *mobility gap* in amorphous semiconductors, somewhat similar to the bandgap for crystalline solids.

The next model was put forth by Cohen, Fritzche, and Ovshinsky, who expanded on Mott's orignal model [13]. Their model, known as the CFO Model, is shown in Figure 2.2 (c). They argued that amorphous semiconductors were more disordered than Mott proposed. So, as a result, the localized tail states extend much deeper into the mobility gap and overlap around the Fermi level. Even though there would be a continuous distribution of states throughout the mobility gap, metallic conduction would not occur because the gap states are still highly localized in space. The CFO model also considered that since the atoms in an amorphous material were less restrained than those in the crystalline state, they would normally be able to fulfill their valency requirements, ie. each atom would be able to have the correct number of bonds. This would prevent any sharp structures in the density of localized states from occurring in the mobility gap.

However, the structure of amorphous semiconductors also contains impurities; atoms with different coordination than normal structure bonding (NSB) of the network. This causes well-defined local defects such as dangling bonds, chain ends, vacancies, substitutional impurities, and interstitials. As such, there will be additional localized states within the mobility gap that the CFO model does not account for. Another model, by Marshal and Owen [14], proposed that these structural defects would cause a larger density of mid-gap states around the Fermi level. This model is shown in Figure 2.2 (d).

2.4 The Atomic Structure of Amorphous Selenium

Selenium has an atomic number, Z, of 34 in the periodic table, contained within Group VI, commonly called chalcogens. Chalcogens have 6 valence electrons in the outermost shell in the eight possible states. Two electrons are located in the s-states and

form a lone pair, and 2 electrons in p-state also form a lone pair. Lone pairs act as non-bonding states, leaving the 2 remaining electrons in the p-states to be used for bonding with other atoms. With this setup, Se has a two-fold coordinated bonding structure with an optimum bond angle of 105º and dihedral angle of 102º [15]. This is the lowest energy configuration for a Se atom.

In the crystalline state, Se can take two forms: α-monoclinic Se (α –Se) and trigonal Se (γ-Se). In α-Se, the atoms bond together and form rings of Se_8 (meaning 8 atoms in one ring), whereas in γ–Se, the Se bonds together to form Se_n spiral chains. Early theory thought that amorphous Selenium would therefore be a mixture of these two states, randomly distributed in the solid. Structural studies now favour a "random chain model". This model specifies that the atoms are linked together in a twofold coordinated chain structure where the magnitude of the dihedral angle, ϕ, is constant but randomly changes sign [15, 16]. The dihedral angle is the angle between two adjacent bonding planes, shown in Figure 2.3. Its definition requires 4 atoms, and can be seen to be the angle between the plane formed by the 1-2-3 atom connection plane, and the 2-3-4 atom connection plane.

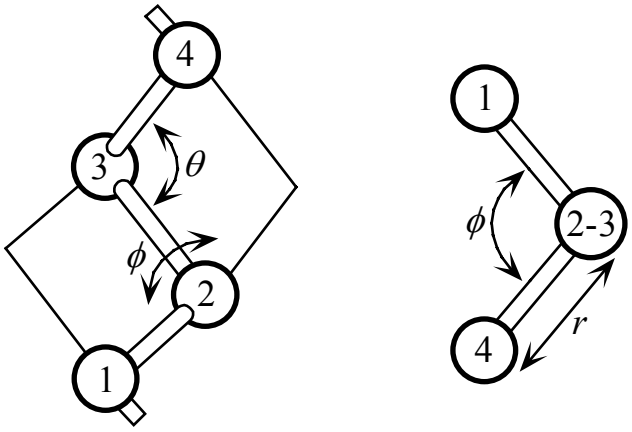

Figure 2.3: The selenium chain model, demonstrating the dihedral angle, ϕ. It is best observed looking down the bond between atoms 2 & 3. The bond angle θ and the bond length r are also shown.

In crystalline Se, the atoms have fixed locations due to symmetry, constant bond length r, constant bond angle θ, and consistent dihedral angle ϕ. The sign of the dihedral

angle depends on which type of crystalline Se is being observed. For trigonal Se, which has a chainlike structure, the dihedral angle rotates in the same sense as moving along a chain to give a spiral pitch of three atoms. Examining the sign of the dihedral angle, it will have a consistent sign being either +++ or ---, where the + and - signs indicate the sign of the dihedral angle. On the other hand, in α-Se, the dihedral angle will alternate its sign in order to generate a ringlike structure, generating a pattern like +-+- [15]. In a-Se, the dihedral angle will randomly change, creating regions that are chainlike and regions that are ringlike. For example, Figure 2.4 shows an a-Se chain with a structure of +++-+-+---, i.e. a chainlike region, followed by a ringlike region, followed by a chainlike region. Various structural studies of a-Se support this model [17].

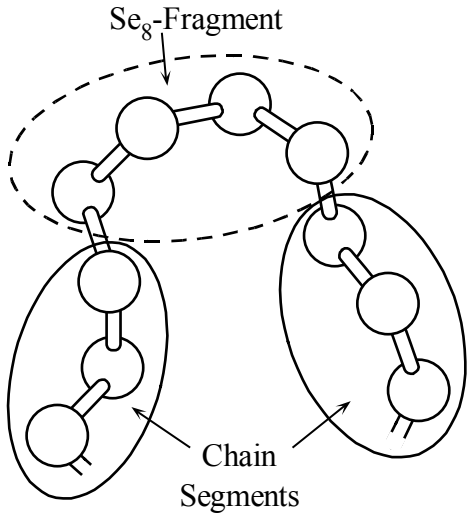

Figure 2.4: The random chain model of the structure a-Se. Certain regions are chainlike and others are ringlike. From [10].

Amorphous chalcogenide solids contain structural defects caused by some of the atoms being over-coordinated or under-coordinated, and a-Se is no exception. Figure 2.5 shows the bonding configurations known for a-Se, adapted from [18]. The lowest energy bonding state is Se_2^0, the normal bonding configuration for Se. The lowest energy neutral defect is Se_3^0 which has three valence electrons available for bonding and one electron in an anti-bonding state. There is also another neutral defect, Se_1^0 which only has one electron available for bonding.

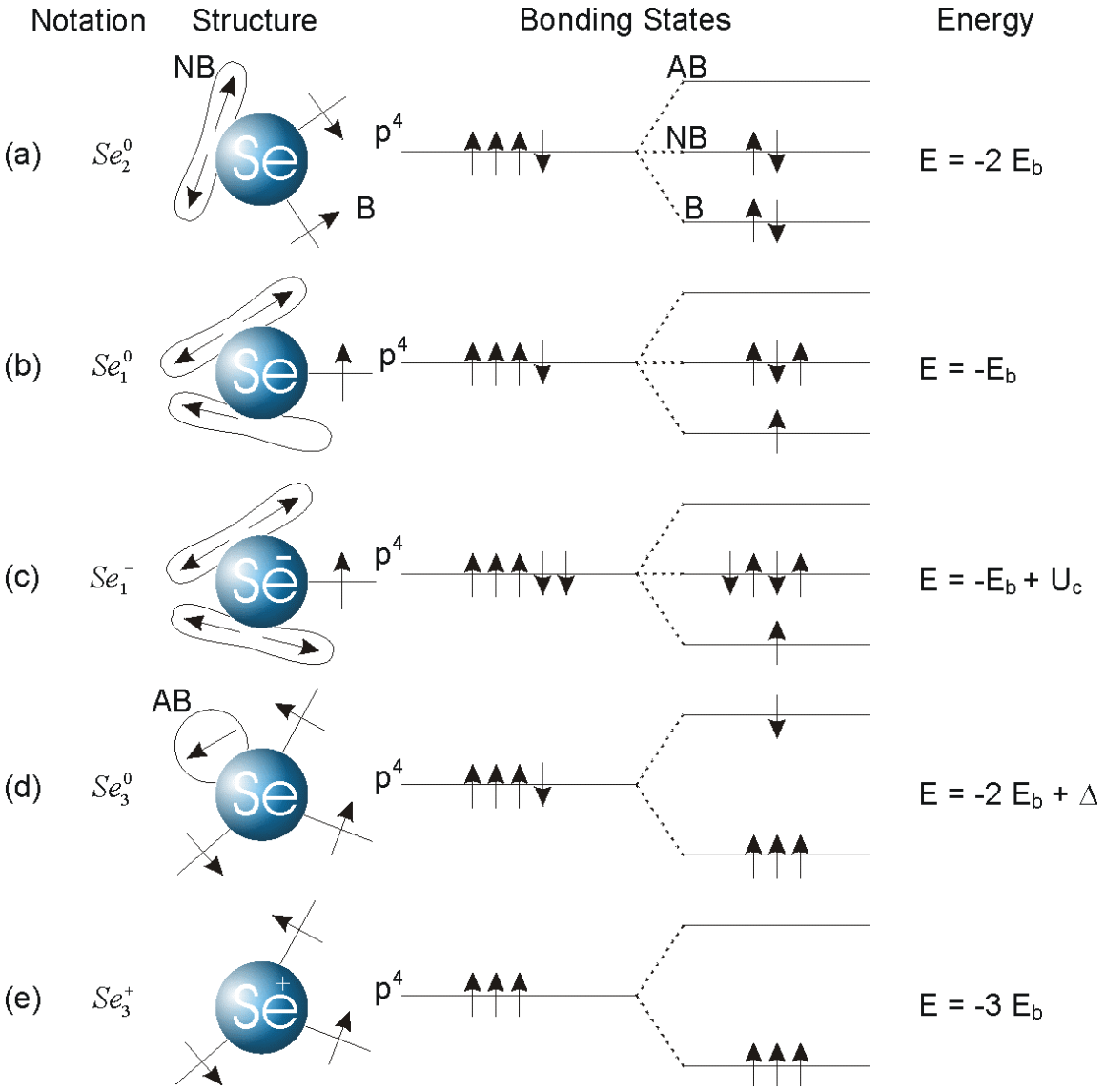

Figure 2.5: Structure and energy for different bonding configurations for Se atoms. Straight lines are bonding orbitals, lobes are lone-pair orbitals (non-bonding), and circles are anti-bonding orbitals. The energy of a lone pair is taken as the zero energy. Figure adapted from [18]

Electron Spin Resonance (ESR) studies have shown that there are no dangling bonds in the a-Se structure [19, 20]. This means that there are very few neutral defects in the a-Se structure. Therefore, the defects from over- and under-coordinated atoms must be thermally derived charged structural defects, know as Valence Alternation Pairs (VAPs). These defects are shown in Figure 2.5 as Se_3^+ and Se_1^-. These defects are more prevalent because they are more energetically favourable than the neutral defects Se_3^0 and

Se_1^0. For example, Se_1^0 as a chain end can lower its energy by approaching the lone pair on a normal Se_2^0 atom in order to generate an intimate valence alternation pair (IVAP). The reaction can release more energy as the resulting IVAP pair diffuses apart. This reaction is denoted as:

$$Se_1^0 + Se_2^0 \rightarrow Se_1^- + Se_3^+ \qquad (2.1)$$

which is exothermic because the reaction releases energy as the lone pair electrons are absorbed into dative bonding. Figure 2.6 shows a representation of a typical a-Se structure with an IVAP.

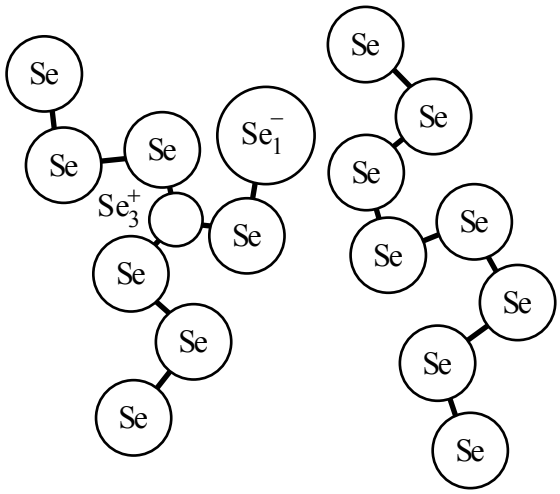

Figure 2.6: The a-Se structure with an IVAP defect, adapted from [10].

2.5 Density of States of a-Se and Carrier Transport in a-Se

Amorphous Selenium and its alloys have been widely studied due its use in xerography in the 1960s and 1970s. Despite the large amount of time spent studying a-Se since its earlier uses, there is still a fundamental disagreement of the exact density of states (DOS) of a-Se, and therefore the exact nature of hole and electron transport in a-Se. The currently accepted DOS is shown in Figure 2.7. It has been derived from various xerographic and transient photoconductivity measurements, such as time-of-flight (TOF) measurements. It was originally proposed by Abkowitz [21] as an extension of the Owen-Marshal DOS model for amorphous semiconductors, described previously. The

model has a decaying density of localized states, but also contains several peaks. The peaks close to the conduction and valence bands are known as shallow electron and hole traps respectively. The peaks in the middle near the Fermi level are know as the deep electron and hole traps. The mobility gap for a-Se in this model is 2.22 eV, as indicated in Figure 2.7.

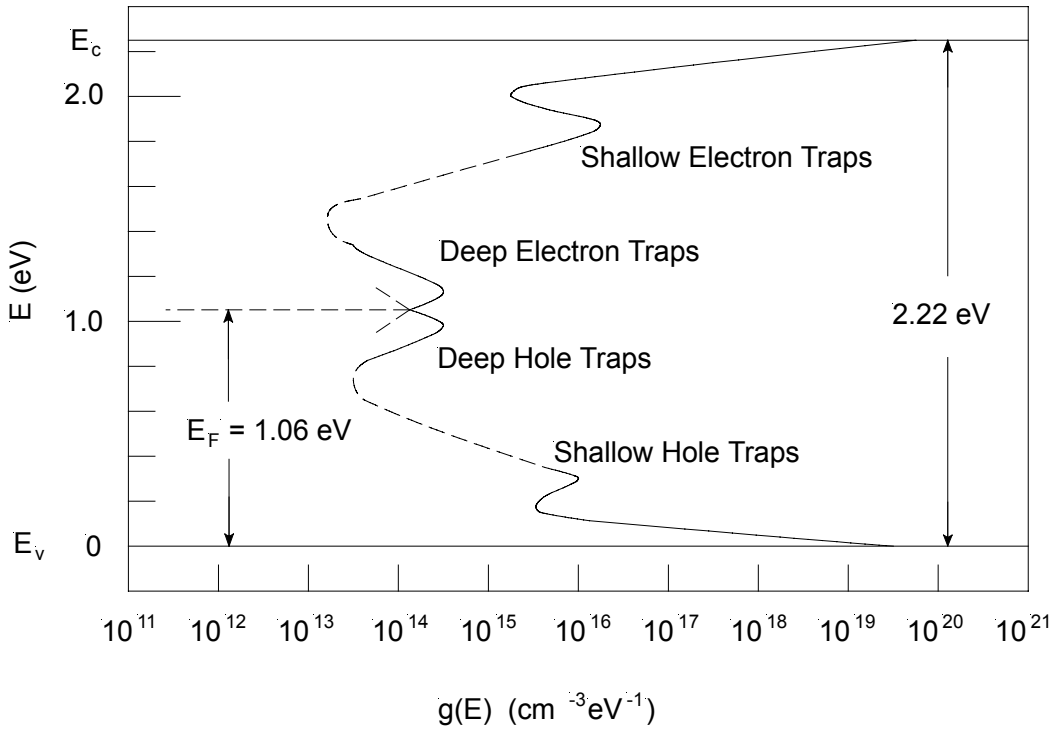

Figure 2.7: Density of states function for a-Se as derived from experimental measurements [21].

The electron and hole mobility in a-Se is believed to be shallow trap controlled [22]; the mobility of the carriers is affected by trapping and release from the shallow traps in the mobility gap. Therefore, the effective carrier mobility μ is the microscopic mobility μ_o reduced by the effects of trapping and release,

$$\mu = \theta\mu_o = \frac{p_{free}}{p_{free} + p_{trapped}}\mu_o \qquad (2.2)$$

where θ is the mobility reduction factor [23], p_{free} is the concentration of free carriers in the transport band, and $p_{trapped}$ is the concentration of trapped carriers in the shallow traps. In this equation, it is assumed that the p_{free} and $p_{trapped}$ are in equilibrium.

With a discrete set of monoenergetic shallow traps, the hole mobility is given by

$$\mu = \mu_o \left[1 + \frac{N_t}{N_v} \exp\left(\frac{E_t}{kT} \right) \right]^{-1} \approx \mu_o \frac{N_v}{N_t} \exp\left(-\frac{E_t}{kT} \right) \qquad (2.3)$$

where N_t is the shallow trap concentration, N_v is the density of states at the valence band edge E_v, and E_t is the energy depth of the shallow traps. By curve fitting mobility data for various temperatures [7] using equation 2.3, the location of the shallow traps in Figure 2.7, E_t, can be found. The peak in the concentration of shallow hole traps is at $E_t - E_v \approx 0.29\,\text{eV}$. Similarly, the electron peak can be found to be at $E_c - E_t \approx 0.35\,\text{eV}$.

The peaks for the deep traps have been measured using photoinduced discharge measurements and cycled-up xerographic residual voltage measurements. The hole deep trap peak was found to be at 0.87 eV from the valence band, and the electron deep trap peak was found to be at 1.22 eV from the conduction band. It should be noted that the total concentration of deep traps for holes and electrons in a-Se is still much less than similar amorphous semiconductors, making a-Se preferable to others for photoconduction. These deep traps are of particular importance because they control the carrier lifetimes. They can significantly alter the carrier schubweg $\mu\tau F$, and therefore the x-ray sensitivity of the photoconductor, as mentioned in Chapter 1.

Various researchers have examined the effects of impurities and alloying on the performance of a-Se. Pure a-Se is unstable on its own, and thus will crystallize over a period of time [7]. By alloying a-Se with small amounts of As (0.2%-0.5%), the crystallization process significantly slows down. Arsenic atoms are triply bonded, and thus bond together a-Se chains to increase the viscosity and help prevent crystallization. The resulting material is known as *stabilized a-Se*. Unfortunately, the addition of As adds additional defects which trap holes, decreasing overall hole lifetime. To counter this, a halogen (typically Cl) is added in the parts per million range. By balancing the amount of As and Cl added to a-Se, a thermally stable film with good electron and hole transport can be created. Table 2.1 summarizes the transport properties of a typical film of stabilized a-Se [11].

Table 2.1: Typical transport properties of stabilized a-Se (a-Se:0.2-0.5%As + 10-40ppm Cl) photoconductor films.

Property	Typical Range	$\mu\tau F$ @ 5V/μm	Comment
Hole Mobility, μ_h (cm^2/Vs)	0.12-0.14		Well reproducible, probably shallow trap controlled
Electron Mobility, μ_e (cm^2/Vs)	0.003-0.006		Decreases rapidly with As addition, probably shallow trap controlled
Hole Lifetime, τ_h (μs)	20-200	1.2-12 mm	Depends on the substrate temperature
Electron Lifetime, τ_e (μs)	200-1000	0.3-1.5 mm	Sensitive to small quantities of impurities
Hole Range, $\mu_h\tau_h$ (cm^2/V)	2×10^{-6} to 2×10^{-5}		Substantially higher than PbI_2
Electron Range, $\mu_e\tau_e$ (cm^2/V)	1×10^{-6} to 6×10^{-6}		Somewhat higher than PbI_2

2.6 Optical Properties of a-Se

a-Se is a photoconductor; its conductivity increases when exposed to light due to an increase in free charge carriers. This occurs because incident photons with enough energy can excite electrons from the valence band up into the conduction band. The optical absorption coefficient, α, determines the likelihood that incoming photons will be absorbed. This coefficient is dependent on the incident photon energy, as well as the magnitude of the DOS at the band edges of the conduction and valence bands. If an incident photon has less energy than the bandgap, it is highly unlikely that it will be absorbed. If the incident photon has more energy than the bandgap, it may be absorbed.

Consequently, the absorption coefficient increases rapidly as the incident photon energy increases to be greater than the bandgap.

It has been shown that the optical absorption coefficient of a-Se exhibits an Urbach edge of the form $\alpha(hv) = 7.35 \times 10^{-12} \exp(hv/0.058\text{eV})\text{cm}^{-1}$. This corresponds to the excitation of charge carriers from the mid-gap localized states into the extended states [24]. At higher photon energies, the absorption coefficient follows $\alpha(hv) \sim (hv - E_o)$ [25], where $E_o \approx 2.05$ eV is the optical band gap at room temperature. This has been attributed to the sharp rise in the density of states at the band edges.

When an optical photon is absorbed, an electron-hole pair (EHP) is generated. An electron from the valence band absorbs the energy of the incident photon and is excited into the conduction band, leaving a void, or hole, in the valence band. Both these generated carriers can contribute conduction current when under an applied field. The probability a generated EHP will be separated by the field (rather than recombining) is given by the quantum efficiency, η. The quantum efficiency is strongly dependent on the magnitude of the applied field, even for large incident photon energies well above the band gap energy. The dependence of α and η on the electric field and incident photon energy (hv) is shown in Figure 2.8.

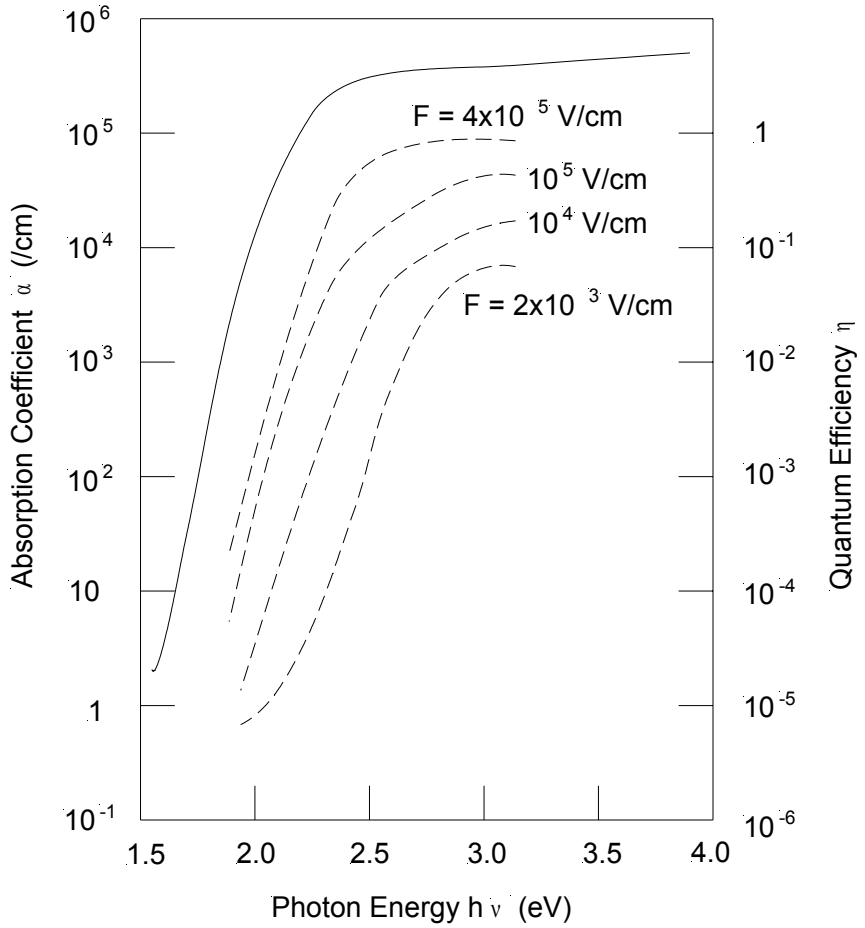

Figure 2.8: Absorption coefficient α (shown by solid line) and quantum efficiency η (shown by dashed lines) as a function of incident photon energy ($h\nu$) for various applied fields.

The Onsager theory for the dissociation of photogenerated EHPs can be used to explain the field dependence of the quantum efficiency [26]. The Onsager theory calculates the probablility that a generated EHP will diffuse apart for a given electric field F, temperature T, and the initial EHP separation r_o. The quantum efficiency can be expressed as

$$\eta = \eta_o f(F, T, r_o) \tag{2.4}$$

where η_o is the quantum efficiency of the intrinsic photogeneration process and $f(F, T, r_o)$ is the probability that an EHP will separate.

2.7 Summary

This chapter introduced the physical structure as well as the electrical and optical properties of amorphous selenium and its alloys. Even though an analytical band model for amorphous semiconductors could not be determined due to the complexity of the amorphous structure, by using experimental observations of the electrical and optical properties, several band models for amorphous semiconductors were generated.

a-Se was found to generate its random structure through variations in the dihedral angle. Thus, a-Se atoms bond together in what is known as the "random chain model". The random variations in this model led to the introduction of localized electronic states in the mobility gap of the density of states function. Additionally, thermodynamically stable VAP defects were shown to also contribute additional localized states within the mobility gap. The location and density of the localized states are of particular interest as they significantly affect the electronic and optical properties of a-Se.

The electrical and optical properties of a-Se depend on the density of states model for a-Se. In the currently accepted model, there are peaks in the density of localized states that occur within the mobility gap. The peaks closest to the conduction and valence bands, known as shallow traps, affect the mobility of carriers through multiple trapping and release events. The peaks in the middle of the mobility gap, known as deep traps, affect the carrier lifetime. These shallow and deep traps therefore heavily influence the carrier schubweg, $\mu\tau F$.

3. Time-of-Flight and Interrupted-Field Time-of-Flight Transient Photoconductivity

3.1 Introduction

As explained previously, amorphous semiconductors are very suitable for use in flat panel x-ray image detection. The charge transport properties within these semiconductors will determine device performance. Because of the complex nature of the amorphous structure, it is almost impossible to theoretically describe this class of materials. Therefore, most research work is done by experiments. The time-of-flight (TOF) and interrupted-field time-of-flight (IFTOF) transient photoconductivity measurements can provide accurate measurements of the drift mobility and deep trapping lifetime in amorphous semiconductors and in particular, in a-Se alloys. These experiments involve observing the current transient caused by the drift of carriers introduced by photoexcitation. This section presents the principles of the TOF & IFTOF techniques, as well as the theory needed for proper interpretation of the transient signals.

3.2 The Time-of-Flight Measurement Technique

The TOF technique measures the transient response generated by the drift of photoinjected carriers as they travel through a sample of highly resistive material. A schematic of the TOF technique is shown in Figure 3.1. A sample of material with thickness L is prepared with 2 metal electrodes, A and B. Electrode A is connected to the voltage supply, while electrode B is connected to ground through a small sampling resistor, R. The resistor R is small enough that the majority of the voltage drops across the high resistivity of the sample.

An excitation pulse of light is applied to electrode A, generating electron-hole pairs (EHPs). In order to have only one type of carrier travel through the sample, the

absorption depth (δ) of the excitation must be much less than the sample thickness, L. This ensures that the non-travelling carrier can be immediately collected at the top electrode and will not interfere with the experiment. In the example shown in Figure 3.1, the electrons will be collected immediately, leaving the holes free to drift across the sample. As the injected holes drift across the sample under the applied field, they will generate a photocurrent $i_{ph}(t)$ through the external resistor, R, which can be easily measured. By reversing the bias voltage applied to the sample, the transient response of electrons can be similarly measured.

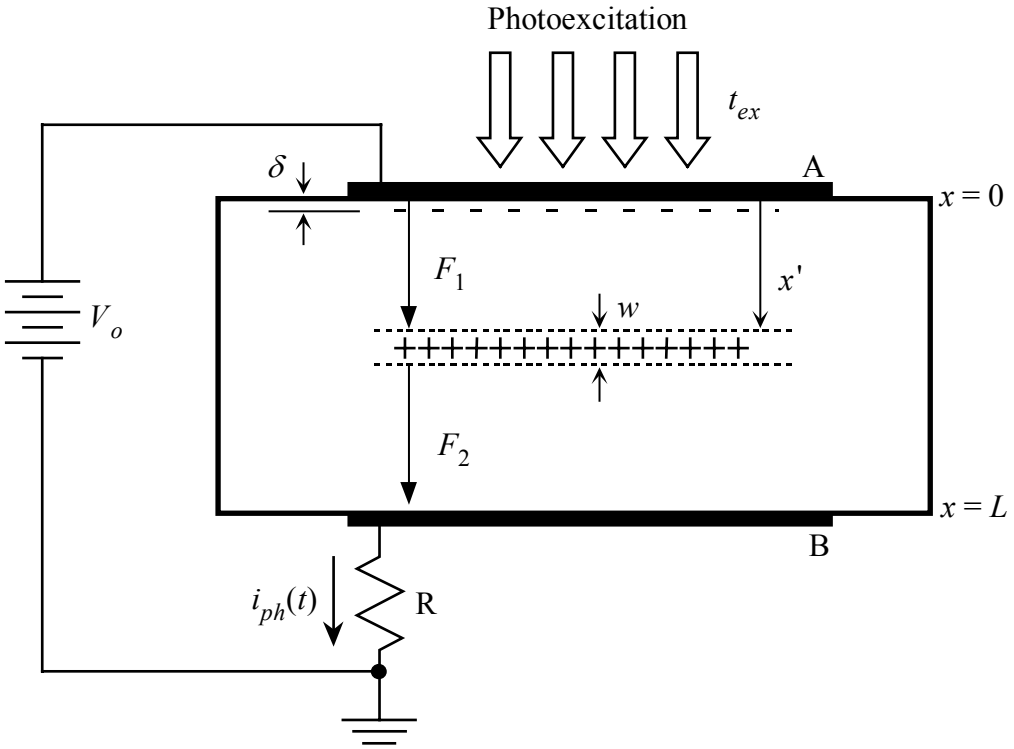

Figure 3.1: Schematic Diagram of the Time-of-Flight Measurement Technique

The photoexcitation source for the experiment is subject to several constraints. First of all, the duration of the excitation pulse must be much shorter than the transit time of the carriers across the sample. This ensures that the carrier packet that will travel through the sample has a very small width (w) and this width will be much less than the sample thickness, L. Next, the wavelength of the photoexcitation must be carefully selected so that the absorption depth of the light (δ) is much less than the sample thickness. This ensures that only one type of carrier will be drifting through the sample

at any one time. However, if the absorption depth is too small, then the carriers that are supposed to be drifting may be trapped by surface defects. Finally, the intensity of the photoexcitation source must be carefully adjusted so that not too many carriers are injected. If too many carriers are injected, it will disturb the internal electric field in the sample and will alter the drifting properties. The injection of a small number of carriers ensures that the experiment is under small signal conditions; required to simplify the mathematics involved in the analysis and the interpretation of the data.

In order to fully understand the photocurrent generated, it is important to first examine the effects of the carrier package on the internal electric field as it drifts through the sample. As stated before, the excitation pulse is kept very short to ensure the packet has a small width, $w << L$, as it drifts through the sample with a speed of v_d. For example, take the setup shown in Figure 3.1; holes make up the charge packet in this setup. At a position x' in the sample, in the absence of space charge, the electric fields F_1 and F_2 in Figure 3.1 will be constant [27]:

$$F_1 = F_o + \frac{ep_o w}{\varepsilon}\left[\frac{x'}{L} - 1\right] \tag{3.1}$$

and

$$F_2 = F_o + \frac{ep_o w}{\varepsilon}\frac{x'}{L} \tag{3.2}$$

where F_o is the applied field, $F_o = V_o/L$, p_o is the concentration of holes in the charge sheet, and ε is the dielectric permitivity of the material. These equations indicate that the electric field has been slightly disturbed by the charge packet; the electric field behind the packet (F_1) is reduced, while the field behind (F_2) is slightly increased. This slight change in the electric field generates the force to induce the transient photocurrent in the external circuitry.

For the TOF photocurrent to be used to determine the drift mobility of carriers, the internal electric field in the sample should be approximately uniform. For the electric field to be considered uniform, the effect of the injected charge packet must be minimal ($ep_o w/\varepsilon << F_o$). This will occur when the injected charge (Q_o) is much less than the

charge on the electrodes, $Q_o << V_o C_s$, where C_s is the capacitance of the sample. This is called the small signal condition, which approximates the internal electrical field as uniform, $F_o = F_1 = F_2 = V_o/L$, and the drift velocity of the carrier packet is considered to be constant [28]. If the small signal condition is not maintained throughout the TOF experiment, the analysis must take into account the effect of the space charge on the electric field and is far more complex [29].

The photocurrent produced by the drift of the charge sheet through the sample can be found using Ramo's theorem [30]. Take the simple diagram shown in Figure 3.2. In a sample of highly resistive material, such as that used for TOF, a charge, q, is generated at l within the sample. The charge is drifting at a constant velocity under the applied bias, $v_d = \mu F_o$, where μ is the mobility of the carrier in the material. As the charge travels across the sample, it induces a current in the external circuit until it reaches the opposite electrode and is collected by the battery, eliminating the external current. From this we can define the transit time as the time it takes the carrier to drift across the sample from the point it is created until it is collected at the electrode. From a simple distance equation, $t_T = l/v_d$.

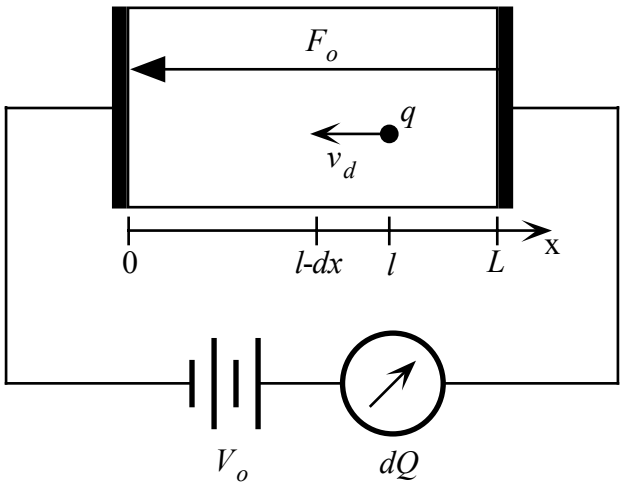

Figure 3.2: The motion of a charge, *q*, through a distance *dx* makes a charge, *dQ*, flow in the external circuit.

The work done by moving the charge q a distance dx is given by $dW = qF_o dx$. This work must be done by an external source, the battery, so the work done moving the

charge dx in a time dt is $dW = V_o i_{ph}(t)dt = qF_o dx$. Since $F_o = V_o/L$ and using $v_d = dx/dt$, it can be shown the external photocurrent is

$$i_{ph}(t) = \begin{cases} \dfrac{qv_d(t)}{L} & \text{for } 0 < t < t_T \\ 0 & \text{for } t \geq t_T \end{cases} \tag{3.3}$$

This equation can be applied to the TOF experiment pictured in Figure 3.1, as long as the small signal condition is met. In which case, the total number of injected holes in the depicted TOF experiment is given by

$$Q_o = ep_o wA \tag{3.4}$$

where p_o is the concentration of injected holes, w is the width of the charge sheet (approximately the absorption depth, δ) and A is the area of the charge sheet (corresponding to the exposure area). From the previous constraints listed, it can be seen that the width of the charge sheet is much less than the sample thickness, L. Therefore, the charge packet will drift across the entire length of the sample. Under the small signal conditions, the drift velocity will be constant at $v_d = \mu_h V_o/L$, so the transit time of the charge sheet can be found from

$$t_T = \frac{L}{v_d} = \frac{L^2}{\mu_h V_o} \tag{3.5}$$

where μ_h is the mobility of the holes injected into the sample. The photocurrent in the external sampling resistor is therefore

$$i_{ph} = \begin{cases} \dfrac{ep_o wAv_d}{L} = \dfrac{ep_o wA}{t_T} & \text{for } 0 < t < t_T \\ 0 & \text{for } t \geq t_T \end{cases} \tag{3.6}$$

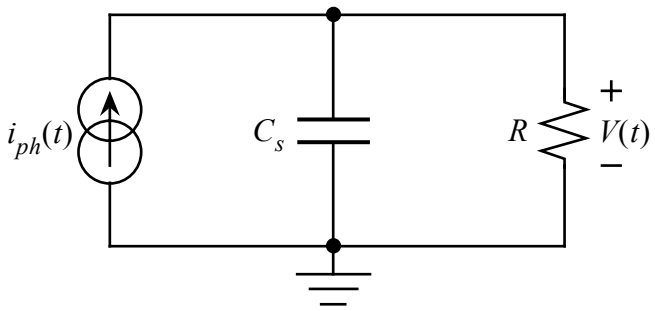

Figure 3.3: A simplified small signal AC equivalent circuit for the TOF experiment. C_s is the combination of the sample capacitance and any parasitics in the external electronics.

The characteristics of the external circuit in Figure 3.1 will affect the transient response. The small signal AC equivalent circuit of Figure 3.1 is shown in Figure 3.3. In the small signal equivalent, C_s is a combination of the sample capacitance, as well as any parasitics present in the external electronics. The photocurrent provides a voltage by passing through a combination of the C_s and the external resistor, R. Using the Laplace transform and setting $I_{ph}(s)$ and $V(s)$ be the Laplace transforms of the current and voltage signals respectively, they are related by

$$V(s) = \frac{R}{sRC_s + 1} I_{ph}(s) \tag{3.7}$$

By taking the inverse Laplace transform, an expression for the transient signal, $v(t)$, can be found. If the bandwidth of the measured signal is arbitrarily defined as the reciprocal of the transit time, then there are two solutions depending on R and C_s. If $RC_s << t_T$, then equation (3.7) leads to

$$v(t) \approx \begin{cases} Ri_{ph}(t) & 0 < t < t_T \\ 0 & t \geq t_T \end{cases} \qquad \text{for } RC_s << t_T \tag{3.8}$$

This is called the I-mode signal because the magnitude of the received signal is directly proportional to the photocurrent. An ideal I-mode signal looks similar to a square wave pulse; it rises sharply at the start and remains constant as the photogenerated carriers drift through the sample, then drops back to zero.

If $RC_s >> t_T$, then equation (3.7) becomes

$$v(t)=\begin{cases}\dfrac{1}{C_s}\dfrac{ep_o wA}{t_T}t & 0<t<t_T \\ \dfrac{1}{C_s}ep_o wA & t\geq t_T\end{cases} \tag{3.9}$$

which can be simplified to be

$$v(t)=\frac{1}{C_s}\int_0^t i_{ph}(t')dt' \qquad \text{for } RC_s >> t_T \tag{3.10}$$

This is known as the V-mode signal, and it is the integral of the I-mode signal. This signal begins at zero and will increase linearly as the carriers travel through the sample. After the carriers reach the collection electrode, the signal will flatten and remain constant at a value proportional to the total number of injected charges.

The previous discussion assumes that the sample is free of carrier traps. This is generally untrue for amorphous semiconductors, as the disordered nature of the semiconductors generates localized states within the mobility gap. These localized states form shallow and deep traps that can capture and hold a mobile carrier, removing them from the transport. Thus, the observed photocurrent will decrease as the mobile carriers are trapped as they travel through the sample.

Adding a set of traps at a discrete energy level in the mobility gap with a mean trapping time of τ_c has a significant effect. If the mean trapping time is assumed to be much longer than the transit time, then any carriers trapped will not be released in the time of the experiment. It can be shown that the number of carriers in the charge sheet will decay exponentially as they travel through the sample, and are captured by the traps. Equation 3.6 can be adjusted with this new factor to be

$$i_{ph}(t)=\frac{ep_o wA\exp(-t/\tau_c)}{t_T} \tag{3.11}$$

The new I-mode signal can be found by substituting equation 3.11 into equation 3.8:

$$v(t)=\begin{cases} R\dfrac{ep_o wA}{t_T}\exp\left(-\dfrac{t}{\tau_c}\right) & 0<t<t_T \\ 0 & t\geq t_T \end{cases} \tag{3.12}$$

The V-mode expression can be found by integrating equation 3.12 to find

$$v(t)=\begin{cases} \dfrac{ep_o wA\tau_c}{C_s t_T}\left(1-\exp\left(\dfrac{-t}{\tau_c}\right)\right) & 0<t<t_T \\ \dfrac{ep_o wA\tau_c}{C_s t_T}\left(1-\exp\left(\dfrac{-t_T}{\tau_c}\right)\right) & t\geq t_T \end{cases} \tag{3.13}$$

A comparison of trap free and with trapping I-mode and V-mode signals is shown in Figure 3.4. The case with trapping (dashed line) is significantly different from the case with no traps (solid lines). The exponential shapes of the waveforms can be used to determine the deep trap capture time i.e. the carrier lifetime.

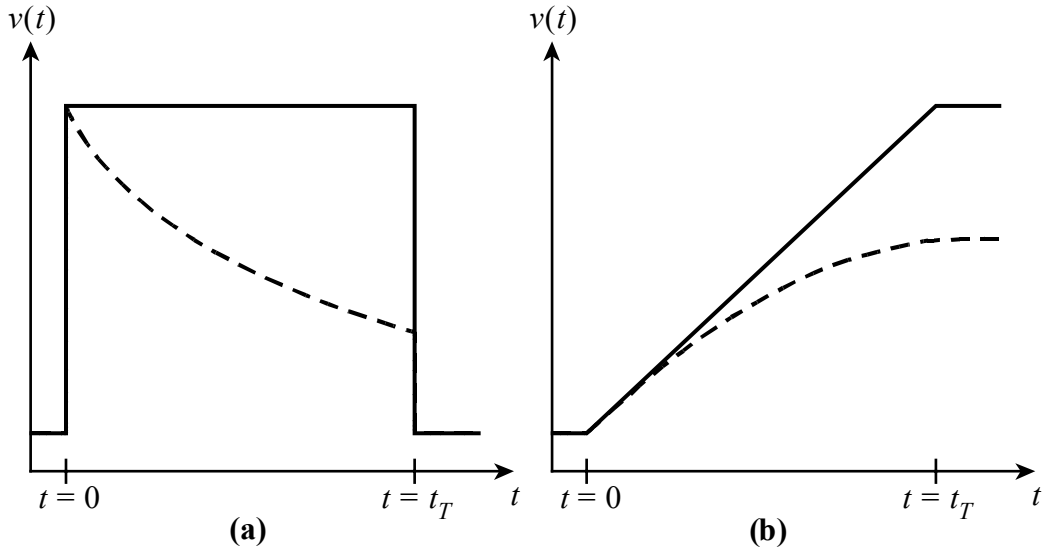

Figure 3.4: TOF transient signals for (a) I-mode and (b) V-mode. Solid lines are the case of sample with no traps, and the dashed lines represent a sample with deep traps.

3.3 The Interrupted-Field Time-of-Flight Technique

The interrupted-field time-of-flight technique is a method to determine the deep trapping lifetime in high resistivity materials. It is based on the time-of-flight technique described in the previous section. A short photoexcitation pulse is applied to a sample

with thickness L under an applied bias V_o, generating electron-hole pairs in the sample. As before, the one carrier (for example, electrons) is immediately collected at the contact, and the remaining carrier (holes) forms a carrier sheet that drifts through the sample, generating a photocurrent measured through the external sampling resistor R. Assuming the small signal condition discussed in the previous section is maintained, the charge packet will drift through the sample with a constant velocity $v_d = \mu V_o/L$ because the electric field is uniform throughout the sample and the mobility, μ, is a material property.

The IFTOF technique measures the deep trapping lifetime of the carriers by interrupting the drift of the carriers and allowing them to interact with the deep traps in the semiconductor. At some time during the drifting of the charge packet, t_1, the bias is removed and the drift of the packet stops, causing the photocurrent to drop to 0. This time t_1 must be before the charge packet has started to reach opposite electrode, i.e. $0 < t_1 < t_T$. The carriers remain stopped at this position, found from $\ell \approx t_1 L/t_T$, and will interact with the localized states deep in the mobility gap, that is, with the deep traps. The bias is re-applied at a time, t_2, and the carriers resume their drift across the sample, generating a post-interruption photocurrent in the external circuit. However, the post-interruption current will be less than the pre-interruption current due to carriers being captured by the deep traps at ℓ during the interruption time $t_i = t_2 - t_1$.

Finding the deep trapping lifetime from this is as follows. If there is a discrete set of traps deep in the mobility gap with lifetime τ_c, then the photocurrent can be found from Equation 3.11. If the bias is adjusted so that the transit time t_T, is much greater than the mean trapping time τ_c, then magnitude of the photocurrent will be

$$i_{ph} = \frac{e\mu N_{oh} F_o}{L} \tag{3.14}$$

where $N_{oh} = p_o A w$, the number of holes injected into the sample to form the charge sheet. Equation 3.14 indicates that the photocurrent is directly proportional to the number of charges injected.

If the traps at ℓ are characterized with the capture time τ_c, then the charge carrier concentration after the interruption $p(t_2)$ can be related to the concentration of carriers before the interruption $p(t_1)$ by

$$\frac{p(t_2)}{p(t_1)} = \exp\left(-\frac{t_i}{\tau_c}\right) \tag{3.15}$$

Since the photocurrent is proportional to the number of carriers, as shown in equation 3.14, it can be inferred that the current before and after the interruption would be related by

$$\frac{i(t_2)}{i(t_1)} = \exp\left(-\frac{t_i}{\tau_c}\right) \tag{3.16}$$

This indicates that the relation between the current before and after the interruption will show the amount of trapping in the material during the interruption. Typical TOF and IFTOF waveforms for a sample with a well-defined trapping time that is larger than the transit time are shown in Figure 3.5. To get the mean carrier lifetime from the IFTOF experiment, several IFTOF waveforms are collected with varying interruption times. The mean carrier lifetime, τ, can be found by taking the slope of a semilogarithmic plot of $i(t_2)/i(t_1)$ versus t_i.

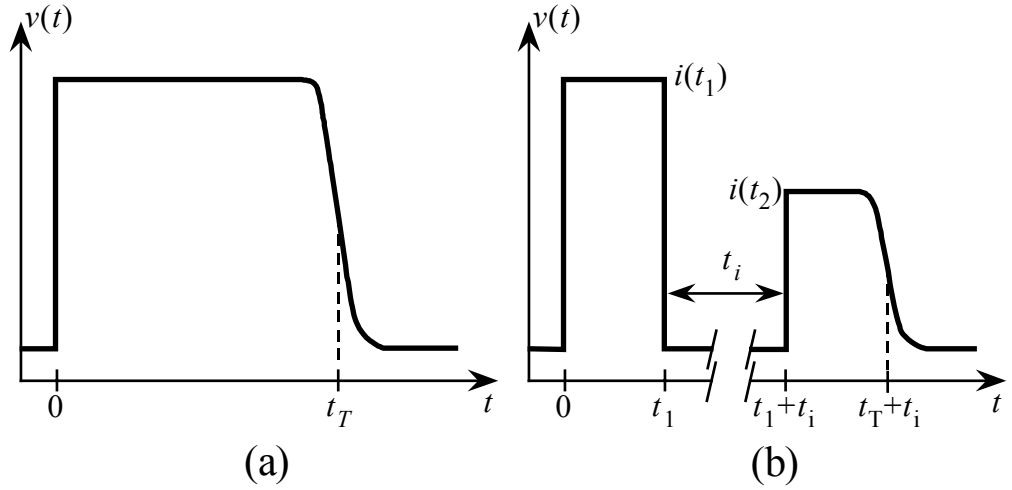

Figure 3.5: (a) Typical TOF waveform. (b) Typical IFTOF waveform. The magnitude of the photocurrent drops after the interruption due to carriers being trapped.

3.4 Transient Trap Limited Theory

The previous sections detailed the principles of the TOF and IFTOF experiments. Expressions for I-mode and V-mode transient responses were also developed. However, these expressions do not match actual transient responses received from measurements on amorphous semiconductors. This is due to the large number of localized states within the mobility gap in actual semiconductors. These states act as shallow and deep traps that can capture a carrier as it is travelling in the sample and significantly alter the transport properties from the ideal. It is important to understand the effects of these traps and their effects on charge transport in the material. In this section, a transient trap-limited theory is developed to explain the transient response in amorphous materials for two cases: monoenergetic trap distribution, and a binary trap distribution.

3.4.1 Monoenergetic Trap Level

This model consists of a set of localized states at a single energy within the mobility gap of a semiconductor. Analysis of this system starts from taking a small slice, *dx*, from a known semiconductor, illustrated in Figure 3.6. The number of free holes in the slice is due to the current flowing through the slice, as well as the thermal release of trapped holes within the slice. The rate of change in the number of holes in the slice can be expressed by the continuity equation as

$$\frac{\partial p(x,t)}{\partial t} = -\frac{1}{e}\frac{\partial J(x,t)}{\partial t} - \frac{\partial p_t(x,t)}{\partial t} \tag{3.17}$$

where $p(x, t)$ is the concentration of free holes, $J(x, t)$ is the net current density flowing, and $p_t(x, t)$ is the concentration of trapped holes in the slice.

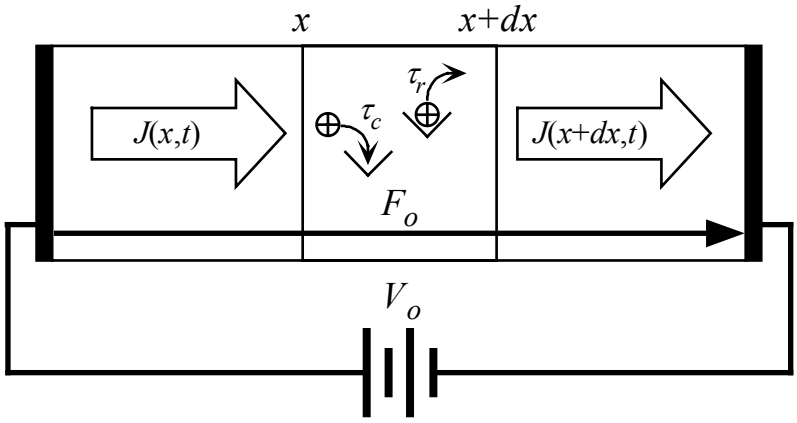

Figure 3.6: Current flow of holes in a semiconductor involving trapping and release within a slice, *dx*.

This current density, $J(x, t)$ is made up of the sum of the conduction current component and the diffusion current. The conduction current is caused by the drift of holes under the applied field, so $J_C(x,t) = e\mu_o p(x,t)F(x,t)$, where e is the charge of an electron, μ_o is the conduction mobility, and $F(x, t)$ is the applied field. The diffusion current is due to spatial variations in the concentration of charge carriers and is given by $J_D(x,t) = -eD\,\partial p(x,t)/\partial x$, where D is the diffusion coefficient. The total current density is the sum of the conduction current and the diffusion current so is given by:

$$J(x,t) = e\mu_o p(x,t)F(x,t) - eD\frac{\partial p(x,t)}{\partial t} \qquad (3.18)$$

Substituting this into equation (3.17) leads to the one dimensional continuity equation for holes:

$$\frac{\partial p(x,t)}{\partial t} = -\mu_o F(x,t)\frac{\partial p(x,t)}{\partial x} - \mu_o p(x,t)\frac{\partial F(x,t)}{\partial x} + D\frac{\partial^2 p(x,t)}{\partial x^2} - \frac{\partial p_t(x,t)}{\partial t} \qquad (3.19)$$

The one-dimensional continuity equation for electrons is similarly derived and is

$$\frac{\partial n(x,t)}{\partial t} = \mu_o F(x,t)\frac{\partial n(x,t)}{\partial x} + \mu_o n(x,t)\frac{\partial F(x,t)}{\partial x} + D\frac{\partial^2 n(x,t)}{\partial x^2} - \frac{\partial n_t(x,t)}{\partial t} \qquad (3.20)$$

where $n(x, t)$ is the concentration of free electrons, and $n_t(x, t)$ is the concentration of trapped electrons.

The rate equations for electrons and holes represent the difference in instantaneous trapping and release rates and involve the rates of change in the

concentration of trapped holes ($\partial p_t(x, t)/\partial t$) and electrons ($\partial n_t(x, t)/\partial t$). The rate equations are as follows:

$$\frac{\partial p_t(x,t)}{\partial t} = \frac{p(x,t)}{\tau_c} - \frac{p_t(x,t)}{\tau_r} \tag{3.21}$$

for holes and

$$\frac{\partial n_t(x,t)}{\partial t} = \frac{n(x,t)}{\tau_c} - \frac{n_t(x,t)}{\tau_r} \tag{3.22}$$

for electrons, where τ_c is the capture time and τ_r is the release time.

An expression for the time dependence of the charge carrier packet can be found by simultaneously solving the rate equation and the continuity equation for the desired carrier. First, a number of simplifying assumptions can be made. First of all, if the small signal condition is maintained, then the electric field ($F(x, t)$) is uniform throughout the sample; therefore, $\partial F(x, t)/ \partial x = 0$. The diffusion portion of the current density can also be safely ignored because the diffusion of the charge carrier packet is assumed to be negligible compared with the drift.

What follows is the derivation for hole transport; the electron transport derivation can be developed with a similar discussion. Boundary conditions to help solve equation 3.19 and 3.21 can be found from the TOF experiment detailed previously. At time t = 0, the photoexcitation pulse generates the carriers at position $x = 0$. If the absorption depth is small relative to the length of the sample, mentioned previously as a constraint for the TOF experiment, then the shape of the generated holes can be approximated with a delta function. Therefore,

$$p(x,0) = N_{oh}\delta(x,0) \tag{3.23}$$

where N_{oh} is the total number of generated holes. Furthermore, the hole traps should be unoccupied since no holes have traveled through the sample yet;

$$p_t(x,0) = 0 \qquad \text{for } x > 0 \tag{3.24}$$

Once the carrier packet has drifted across the sample, the carriers will be collected at the electrode. Therefore,

$$p(x,t) = 0 \qquad \text{for } x > L \tag{3.25}$$

It also follows that there can't be any traps outside of the sample, so

$$p_t(x,t) = 0 \qquad \text{for } x > L \tag{3.26}$$

Equations 3.19 and 3.21 can be solved using these boundary conditions and the Laplace transform techniques, shown in [31, 32]. This gives an expression for the free hole density as the packet travels through the sample:

$$p(x,t) = \frac{N_{oh}}{\mu_o F}\exp\left(-\frac{z}{\tau_c}\right)\delta(t-z) + \frac{N_{oh}}{\mu_o F}\exp\left[-\frac{z}{\tau_c} - \frac{(t-z)}{\tau_r}\right]\frac{\xi}{2}\frac{I_1(\xi)}{(t-z)}U(t-z) \tag{3.27}$$

where $z = x/\mu_o F$, $I_1(\xi)$ is the 1st order hyperbolic Bessel function, $U(x)$ is the unit step function, and $\xi = \left(2\sqrt{\tau_c z(t-z)/\tau_r}\right)/\tau_c$. The first term, involving the delta function $\delta(x)$, represents the charge carriers remaining in the injected packet as it drifts across the sample. These carriers are not delayed by trapping and release as they travel through the sample, but do decrease exponentially as $\exp(-t/\tau_c)$. The second term, involving the Bessel function, represents carriers that have been trapped and removed from the packet. They are released at a later time, t, into the transport band, contributing to a photocurrent after the transit time of the carrier packet, $t_T = L/\mu_o F$ where μ_o is the conduction mobility.

The time dependence of the number of free holes in the charge packet can be found by integrating equation 3.27 over the entire sample length. Unfortunately, an explicit expression for the number of free carriers is far too complex to work with. Therefore, the transient current response is usually examined in two specific cases: low field drift and high field drift. These cases do not create problems for predicting the transient response in TOF experiments since they can be easily met by appropriate choices of sample thickness, bias voltage, and temperature.

3.4.1.1 Low Fields: Shallow Trap Controlled Transport

In this case, it is assumed that the transit time of the carriers t_T is much longer than carrier capture time τ_c and is comparable to the carrier release time, τ_r, i.e. $\tau_c << L/\mu_o F \approx \tau_r$. Carriers in the charge packet will be captured by a set of localized traps close to the band edge and once released, will continue drifting towards the

collecting electrode. Thus the carriers traverse the sample through many capture and release events. With the transit time and release time comparable, the time derivative of the total charge in the conduction band in Equations 3.18 and 3.19 vanishes over a large period of time [33], i.e. the number of free carriers eventually enters steady state. By making use of the principle of conservation of charge, the total free holes P can be related to the total injected charge by

$$P = N_{oh} \frac{\tau_c}{\tau_c + \tau_r} \tag{3.28}$$

where $N_{oh} = p_o A w$ is the total number of injected holes. The I-mode photocurrent signal can be found by substituting this into Equation 3.6. The result is

$$i_{ph} = \frac{eN_{oh}\mu_o F}{L} \frac{\tau_c}{\tau_c + \tau_r} = \frac{eN_{oh}\mu F}{L} \tag{3.29}$$

This resembles the equation for trap free I-mode photocurrent signal with the mobility μ_o reduced to μ by

$$\mu = \frac{\tau_c}{\tau_c + \tau_r} \mu_o = \theta \mu_o \tag{3.30}$$

where $\theta = \tau_c / \tau_c + \tau_r$. The I-mode signal for this system with traps can be found by simply substituting equation 3.29 into equation 3.8. A comparison of the I-mode signals for the trap free mobility and shallow trap controlled transport models is presented in Figure 3.7.

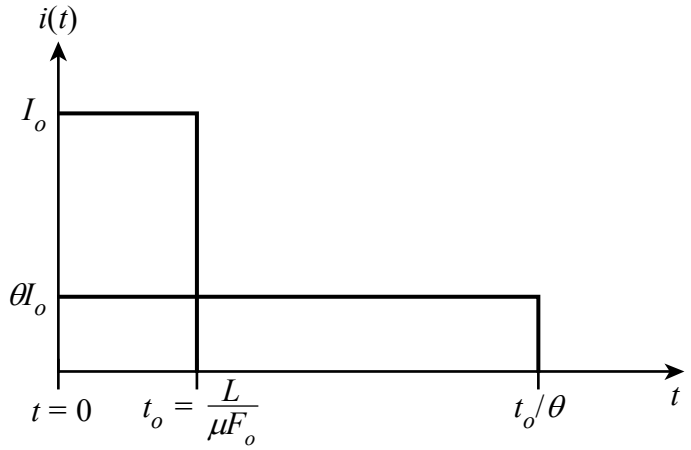

Figure 3.7: Comparison the I-mode signals for the trap free drift mobility and shallow trap controlled models.

The effective carrier drift mobility is reduced from the trap-free drift mobility (the mobility in the band) because the carriers are delayed by capture and release events. This transport mechanism is known as *shallow trap-controlled transport*, and the scalar θ is referred to the *shallow trap-controlled transport factor*.

3.4.1.2 High Fields

With a large bias, a portion of the carriers in the charge packet may be able to travel across the sample without being trapped, i.e. $L/\mu_o F << \tau_c$. Expressions for the TOF transient signal were developed in two different time ranges by [34]. The first expression is

$$i_{ph}(t) = \frac{eN_{oh}}{t_T}\left[\frac{\tau_c}{\tau_c+\tau_r} + \frac{\tau_r}{\tau_c+\tau_r}\exp\left(-\frac{\tau_c+\tau_r}{\tau_c\tau_r}t\right)\right] \quad \text{for } 0 < t < \frac{L}{\mu_o F} \tag{3.31}$$

If detrapping is neglected so that $\tau_r \rightarrow \infty$, then Equation 3.31 reduces to the simple case of deep trapping only, shown in Equation 3.11.

The second expression is for the carriers that were trapped and released into the transport band. The carriers will likely be able to exit the sample without trapping again because they would have travelled a portion of the sample before being trapped. The transient response due to the released carriers can be shown to be [34]

$$i_{ph}(t) = \frac{eN_{oh}}{2}\frac{t_T}{\tau_c\tau_r}\exp\left(-\frac{t}{\tau_r}\right) \qquad \text{for } t > L/\mu_o F \tag{3.32}$$

These two equations indicate that the transient photocurrent will initially decay exponentially until $t = L/\mu_o F$, where a step down in magnitude will occur, followed by another exponential decay to zero as the trapped carriers are released and collected. This response is shown in Figure 3.8.

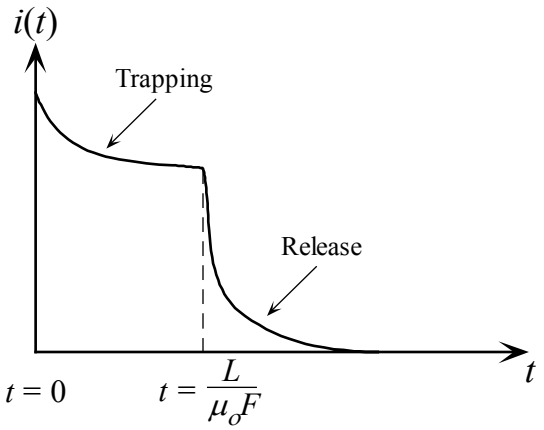

Figure 3.8: Diagram of the photocurrent in the high fields model.

3.4.2 Binary Trap Distribution

This distribution involves two localized states in the transport band with two separate capture times, τ_{c1} and τ_{c2}, and two release times, τ_{r1} and τ_{r2}. This distribution is clearly more complicated than the previous distribution with only one set of capture and release times. To simplify the analysis, it is assumed that the concentration of injected charge is much less than the concentration of traps at each energy state. Thus, the effects of trap filling can be ignored because there can never be enough free carriers to ever fill all the traps. It is also assumed that the number of carriers trapped at a particular level can only increase by the trapping of a free carrier moving in the transport band; carriers being released from the other level of traps cannot be captured until they are considered to be in the transport band again. The hole rate equations for this trap distribution are

$$\frac{\partial p_{t1}(x,t)}{\partial t} = \frac{p(x,t)}{\tau_{c1}} - \frac{p_{t1}(x,t)}{\tau_{r1}} \tag{3.33}$$

and

$$\frac{\partial p_{t2}(x,t)}{\partial t} = \frac{p(x,t)}{\tau_{c2}} - \frac{p_{t2}(x,t)}{\tau_{r2}} \tag{3.34}$$

An expression for the time dependence of the concentration of holes in the charge packet can be found by simultaneously solving equations 3.33, 3.34 and the continuity equation for holes, equation 3.19. The total trap concentration in this case will actually be a combination of the concentration at each trap level, i.e. $p_t(x,t) = p_{t1}(x,t) + p_{t2}(x,t)$.

An expression for the transient photocurrent with a binary trap distribution was developed by Blakney and Grunwald [35] and is as follows:

$$j(t) = A\exp(-\alpha t) + B\exp(-\beta t) + j_\infty \tag{3.35}$$

where

$$\alpha + \beta = \frac{1+\theta_1}{\tau_{c1}} + \frac{1+\theta_2}{\tau_{c2}} \tag{3.36}$$

$$\alpha\beta = \frac{\left[\theta_1 + \theta_2(1+\theta_1)\right]}{\tau_{c1}\tau_{c2}} \tag{3.37}$$

$$\alpha A + \beta B = \frac{j_o}{\tau_{c1}} + \frac{j_o}{\tau_{c2}} \tag{3.38}$$

$$A + B + j_\infty = j_o \tag{3.39}$$

and

$$j_\infty = \frac{j_o\theta_1\theta_2}{\left[\theta_1 + \theta_2(1+\theta_1)\right]} \tag{3.40}$$

where $\theta_1 = \tau_{c1}/\tau_{r1}$ and $\theta_2 = \tau_{c2}/\tau_{r2}$. j_∞ represents the steady state current that flows when the drifting free carriers are in equilibrium with the traps.

The case when one series of traps has a release time that is far higher than the transit time, i.e. $\tau_{r2} \rightarrow \infty$ is of particular interest. In this case, $\theta_2 \approx 0$ so equation 3.35 reduces to

$$j(t) = A\exp\left(-\frac{t}{\tau_{c1}}\right) + B\exp\left(-\frac{\theta_1 t}{\tau_{c2}}\right) \tag{3.41}$$

This transport mechanism is called *shallow-trap controlled transport with deep trapping*, and is often used to describe transport in a-Se [36, 37]. The first term indicates a spike that will decay exponentially until the carriers reach equilibrium with the shallower traps. This is followed by a slower decaying exponential with a decay rate given by τ_{c2}/θ_1.

It is important to mention that the measured lifetime, τ, from IFTOF experiments is actually θ/τ_{c2}. τ_{c2} is the deep trapping time into a set of traps from which there is no release. τ_{c2} depends on the total concentration of deep traps through the relation

$$\frac{1}{\tau_{c2}} = \sigma u N_T \tag{3.42}$$

where σ is the capture cross section, u is the mean speed of the carriers, usually taken as the thermal velocity (10^7 m/s) and N_T is the total trap concentration. The latter involves integrating the density of localized states $N_t(E)$ over energies in which there are deep traps, i.e.

$$N_T = \int_{E_1}^{E_2} N_t(E) dE \tag{3.43}$$

where E_1 and E_2 define the energy range where the localized states are deep (there is no release).

Further, the TOF/IFTOF experiments provide an effective lifetime, τ, which is τ_{c2}/θ. Thus,

$$\frac{1}{\tau} = \frac{\theta}{\tau_{c2}} = \theta \sigma u N_T \tag{3.44}$$

It is apparent that the calculation of N_T from the measurement of τ requires that we know, θ, σ and u. Usually θ can be found from μ/μ_o and σ can be taken as a typical capture cross section for the particular capture process that is assumed to exist. E.g. trapping by neutral traps or trapping by charge traps. It is important to note also that the product $\mu\tau$ does not depend on θ:

$$\mu\tau = \mu_o \tau_{c2} = \frac{\mu_o}{\sigma u N_T} \tag{3.45}$$

3.5 Summary

The principles behind the time-of-flight and interrupted-field time-of-flight experiments were introduced in this chapter. Both techniques involve measuring the transient response caused by the drift of photogenerated carriers through a highly resistive material. The time-of-flight technique allows for determination of the carrier

mobility, while the interrupted-field time-of-flight technique can be used to accurately determine the lifetime of the carrier in the material. Since the carrier mobility and carrier lifetime are so important for device performance, accurate determination of each is quite important for device fabrication.

This chapter also examined transient responses for simple but different theoretical trap distributions to elucidate the dependence of the photocurrent shape on the trap distributions. Energetically shallow traps were found to delay the transit time by trapping a free moving carrier for a short time before release, and therefore decrease the mobility of the carriers. Deeper traps were found to cause the signal to decrease exponentially, in relation to the carrier trapping time τ_c. Because of their ability to measure the mobility and lifetime in a material quite accurately, the TOF and IFTOF techniques can be used to investigate the distribution of gap states in amorphous Selenium alloys in which the transport is not dispersive. Therefore, both the TOF and IFTOF techniques are important tools for the investigation of amorphous semiconductors.

4. Experimental Procedure

4.1 Introduction

The experimental procedure used to measure the electrical properties of different alloys of amorphous selenium (a-Se) is described in this chapter. In section 4.2, the procedure used to create different a-Se alloy samples is described. In section 4.3, the basic experimental setup for the TOF and IFTOF techniques is described, the procedure for determining electronic properties from the measurements, as well as the difficulties present in transient photoconductivity measurements are presented. In section 1.4, the exact experimental system built for this study is described in detail.

4.2 Sample Preparation

Samples of various alloys of a-Se were fabricated using standard vacuum deposition techniques. Selenium in the form of vitreous pellets is placed in a molybdenum boat and is heated to evaporation. The Selenium vapour rises in the vacuum-sealed chamber and condenses on a substrate to form a layer of a-Se. In this work, alloys of a-Se contained various levels of Arsenic (As) to form "stabilized" a-Se, and one sample also contained Chlorine (Cl) as a dopant. Arsenic levels varied from 0 - 5%As and one set of samples of a-Se:0.3%As contained 5ppm Cl. All samples were made from original source material supplied by Anrad Corporation of Montreal. The quoted compositions are nominal values, and are expected to be within 25-30%.

Cleaned Corning Glass substrates coated with a layer of aluminum were used as substrates for the samples. The aluminum served as the "bottom" electrode for the TOF/IFTOF measurements. To deposit the a-Se samples, the substrates were placed into an NRC 3117 stainless steel vacuum coater system, shown in Figure 4.1. After adding the source material to the molybdenum boat, the system was sealed and the chamber was

evacuated to a base pressure of ~10^{-6} Torr. The boat was then heated to ~250 ºC by the application of a large AC current. Two thermocouples, one connected to the boat and the other connected to the substrates were used to carefully monitor the deposition temperature. A digital quartz crystal rate monitor was used to monitor the evaporation rate of the source Selenium material. A simple mechanical shutter was used to prevent deposition from occurring until a steady deposition rate was attained.

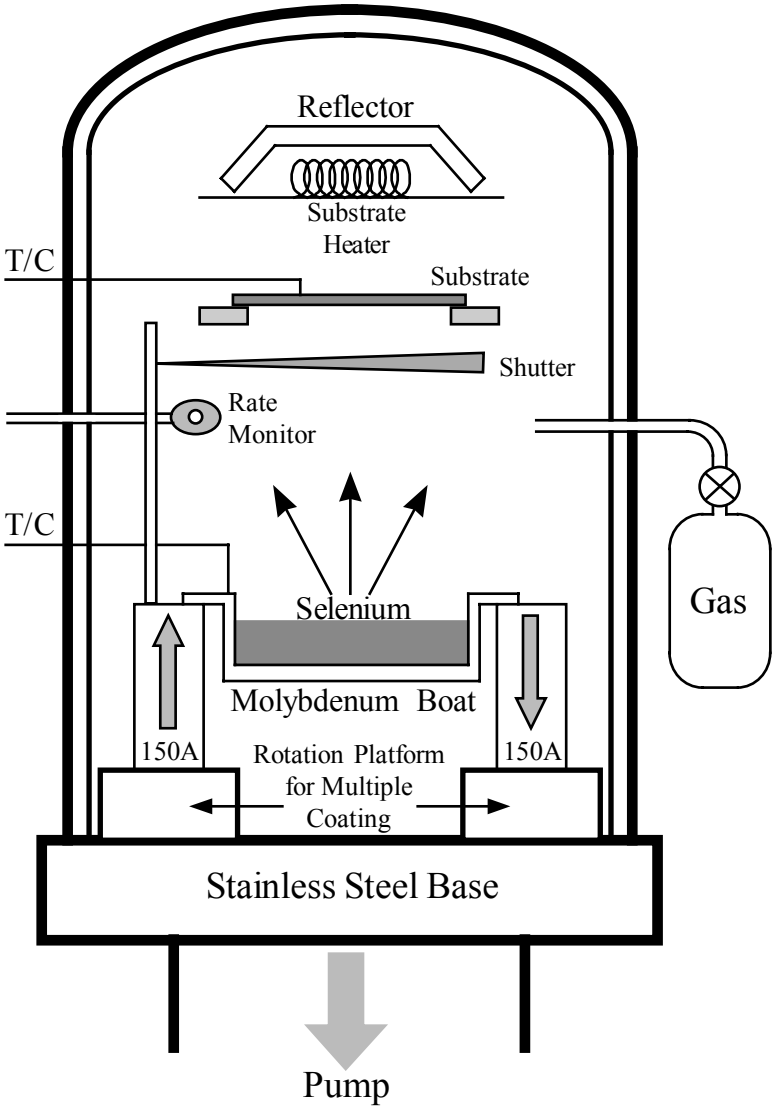

Figure 4.1: Schematic diagram of the NRC 3117 vacuum deposition system used to make the samples in this study. From [11].

The temperature of the substrates was maintained above the glass transition temperature of Selenium during the deposition. To generate homogeneous samples, the

deposition had to be carefully controlled to ensure it was even; the mechanical shutter was not opened until a steady deposition rate was achieved and was closed before all the Se source material was evaporated. The substrate and boat heaters were then turned off to cool while the system was re-pressurizing. The samples were then removed from the system and their thicknesses were measured using a digital micrometer.

Semitransparent Gold contacts were then sputtered onto the samples to allow for connection in the TOF/IFTOF apparatus. These contacts were generated with the use of a Hummer VI sputtering system, shown in Figure 4.2. To ensure an even contact, the a-Se samples were covered with an aluminum mask exposing a small circular area of 0.2 cm^2 before being placed into the sputtering system. The chamber was pumped to a pressure of 100 mTorr and flooded with Argon gas. A high voltage was then applied to ionize the argon gas molecules; the positively charged ions collided with the negatively charged gold target, causing small particles of gold to fall and uniformly cover the exposed part of the sample.

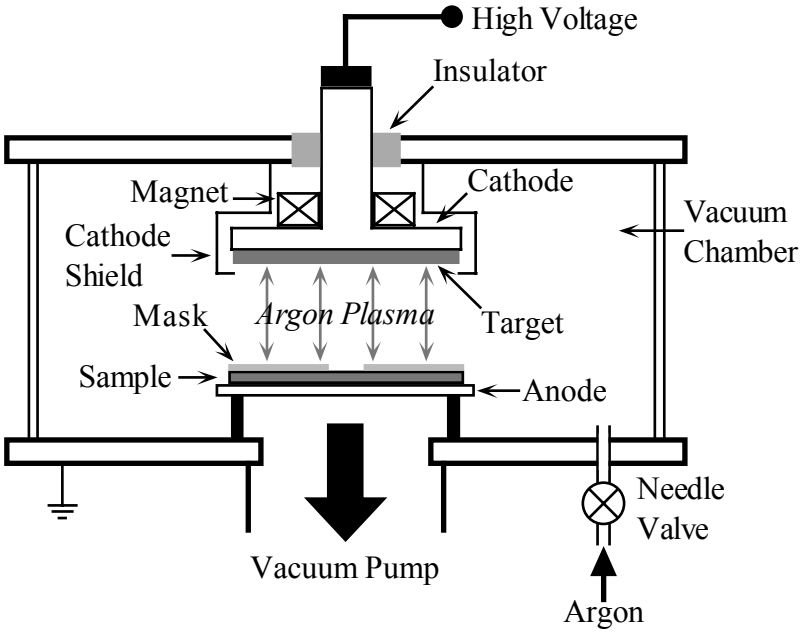

Figure 4.2: Schematic diagram of the Hummer VI sputtering system used to generate contacts on the a-Se samples. From [11].

With the top contact applied to the sample, the sample was ready for TOF/IFTOF measurements. The sample was then loaded onto the sample holder of the apparatus and electrical connections were established using stainless steel connectors and small bits of indium to protect the sample and improve the electrical connections.

4.3 Charge Transport Measurements

The charge transport properties of the a-Se used in the experiments were measured using conventional Time-of-Flight (TOF) and Interrupted-Field Time-of-Flight (IFTOF) measurements. These measurements involve measuring the transient response caused by a photocurrent injected into a semiconductor, as discussed in the theory section. A simplified system capable of these measurements is depicted in Figure 4.3. A high voltage bias, V, is applied to the sample. A short pulse of light is applied to the sample to inject electron-hole pairs. The one carrier, electrons in the case shown in Figure 4.3, is immediately absorbed at the contact, while the other carrier, holes in Figure 4.3, is free to drift through the sample. The drifting of these carriers creates a photocurrent $i(t)$ which can be converted to a voltage by passing it through a sampling resistor, R. This voltage is then passed through an amplifier before being recorded on the oscilloscope. The oscilloscope is triggered just before the application of the light pulse in order to collect the entire photocurrent response.

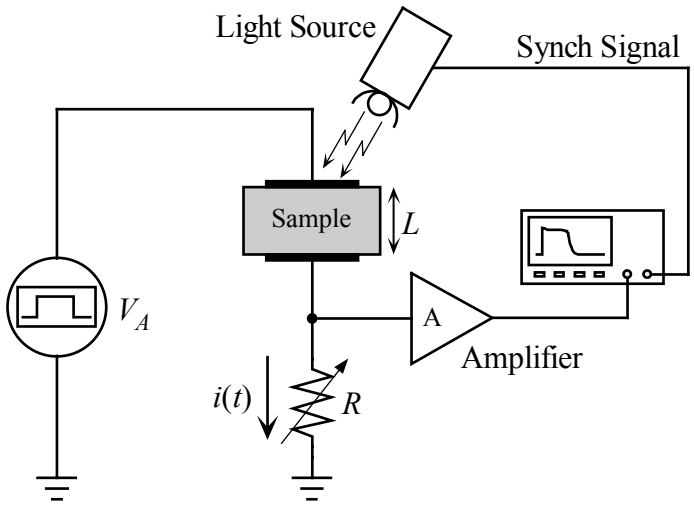

Figure 4.3: A briefly simplified schematic of a system for transient photoconductivity measurements. The voltage supply *V* will supply constant or pulsed bias for TOF and IFTOF measurements respectively. The oscilloscope is synchronized with the light source in order to effectively capture the transient photocurrent signal.

The magnitude of the received photocurrent is directly proportional to the magnitude of the sampling resistor, from $v(t) = Ri(t)$. Increasing the value of R can therefore increase the received signal. This will unfortunately increase the RC time constant of the apparatus, with C being a combination of the sample capacitance and any stray capacitance from the wires, connectors, and other electronics in the circuit. If the RC constant is too large, the resulting signal will become distorted. For a proper TOF experiment, R must be balanced such that $RC << t_T$, where t_T is the transit time of the TOF pulse.

The TOF technique works well for determining the drift mobilities of both holes and electrons in high resistivity semiconductors. The technique was first introduced by Spear [22], Kepler [38], LeBlanc [39], and Brown [40], and several modifications have appeared over time such as: different photoexcitation sources, different high voltage bias schemes, or advanced photoexcitation schemes such as those used to study bulk space charge buildup effects [41]. The most common photoexcitation source involves using a short pulse of strongly absorbed light specifically chosen so that its photogeneration is very near the semitransparent electrode. For a-Se, excitation sources have included such

photoexcitation sources as a xenon flash lamp [42], a nitrogen laser [11], and a pulsed electron beam [43].

A typical timing and resulting I-mode waveform for a TOF experiment is shown in Figure 4.4 (a). The waveform shown is due to drifting holes in the sample; to measure electrons, the polarity of the bias voltage simply needs to be reversed. At time $t = 0$, a pulse of light is injected into the sample, generating electron-hole pairs. In this case, the electrons are immediately collected at the top contact of the sample while the holes form a charge sheet that traverses the sample. This motion of the carriers generates a transient photocurrent that is measured by the electronics. The mobility of the carriers is found from the time width of the transient pulse, which corresponds to the transit time t_T of the charge sheet. The transit time is the time it takes for the carriers to drift from the point of creation to the collecting electrode.

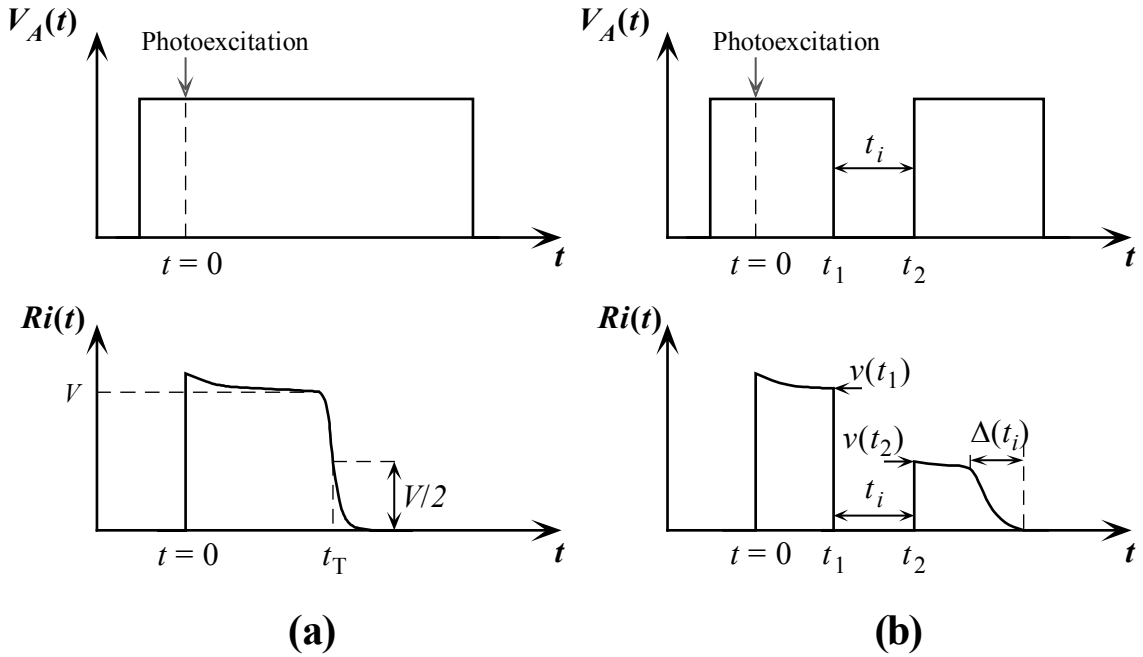

Figure 4.4: Typical timing and resulting transient photocurrent for drifting holes for (a) TOF experiment and (b) IFTOF experiment. The hole drift mobility is found using the transit time of the TOF transient. The hole lifetime is found from the ratio of the recovered photocurrent to the initial photocurrent after an interruption time t_i in the IFTOF transient.

The falling edge on a TOF pulse typically is slightly spread out, as shown around t_T in Figure 4.4 (a). This is called a photocurrent tail and is due to the dispersion of the

carriers in the charge sheet as they travel through the sample. It may be attributed to carrier dispersion, mutual Coulombic repulsion between the charges of the sheet, and multiple trappings in the shallow states mentioned in the previous chapter. The carrier transit time is found at the half magnitude point on the photocurrent tail, shown in Figure 4.4 (a). This is the time when approximately half of the injected carriers have been collected, and is good approximation for the mean transit time.

Finding the drift mobility from the waveform depicted in Figure 4.4 (a) is simple. Since the holes are generated near the surface of the sample, it can be safely assumed that the distance they travel before being collected is the length of the sample, L. Therefore, the average drift velocity can be found from a simple distance equation, $v_{dh} = L/t_T$. If the internal electric field ($F = V/L$) is assumed to be uniform, the drift velocity will be constant and related to the drift mobility by $v_{dh} = \mu_h F$. Therefore,

$$\mu_h = \frac{L^2}{Vt_T} \tag{4.1}$$

where V is the magnitude of the applied bias. The drift mobility for electrons, μ_e, can be calculated using the same arguments.

A typical timing and resulting waveform for an IFTOF experiment is shown in Figure 4.4 (b). The waveform shown is for holes, but similar results can be achieved for electrons by simply reversing the bias. The IFTOF experiment begins much like the regular TOF experiment; at time $t = 0$ a short pulse of light is injected into the sample, generating electron-hole pairs. Again, the electrons are collected at the top contact of the sample, while the holes drift across the sample. However, at time $t = t_1$, the bias is removed from the sample, halting the drift of the holes and causing the transient photocurrent to drop to 0. The bias is reapplied at time $t = t_2$, and the drifting of the holes commences again, generating another transient pulse.

The interruption time in the IFTOF experiment is defined as $t_i = t_2 - t_1$. During this time, the carriers are stopped at a point within the sample, where they are able to interact more easily with the varying levels of traps in the sample. Some of the carriers

will become trapped in localized states deep in the mobility gap and will be effectively removed from the rest of the charge sheet. The loss of carriers to these localized states is easily seen in the decrease of magnitude from before to after the interruption. For a distinct set of traps with an average capture time of τ_h, the fractional recovered photocurrent signal ($v(t_2)/v(t_1)$) is related to the interruption time by [44]

$$\frac{v(t_2)}{v(t_1)} = \exp\left(-\frac{t_i}{\tau_h}\right) \tag{4.2}$$

With repeated IFTOF experiments with the same interruption starting point used (t_1), but varying t_i, the effect on $v(t_2)/v(t_1)$ can be seen. By plotting $v(t_2)/v(t_1)$ vs. t_i on a logarithmic scale, the graph will approximately generate a straight line. The slope of this line gives the mean carrier lifetime, τ_h.

During the interruption time, the charge sheet does not move. However, the width of the carrier sheet will increase as the carriers spread out due to thermal diffusion and mutual Coulombic repulsion. This spreading is clearly visible in Figure 4.4 (b), and is represented by $\Delta(t_i)$. Because of this spreading, it is possible that the carriers could spread out enough to be collected by the contacts. If this occurs, the decrease in recovered signal will be due to not only the loss of the carriers due to traps in the samples, but also the loss of the carriers due to collection at the contact. As long as the width of the tail of the recovered pulse does not increase to the width of the interruption time, it can be assumed that no charges were lost due to collection at the contacts.

The IFTOF technique is experimentally difficult to implement. The difficulty comes from large transients generated by switching the high voltage on and off. This is demonstrated for a simple system shown in Figure 4.5. The sample is made of high resistivity dielectric material between two metal contacts, essentially a parallel-plate capacitor with capacitance, C_s. This capacitance, when combined with the external sampling resistor, R, creates an RC time constant which will generate large displacement currents from switching the high voltages. This displacement current is quite large (a signal >100V on the sampling resistor), and will completely dwarf the transient signal being measured, which is on the order of ~20mV.

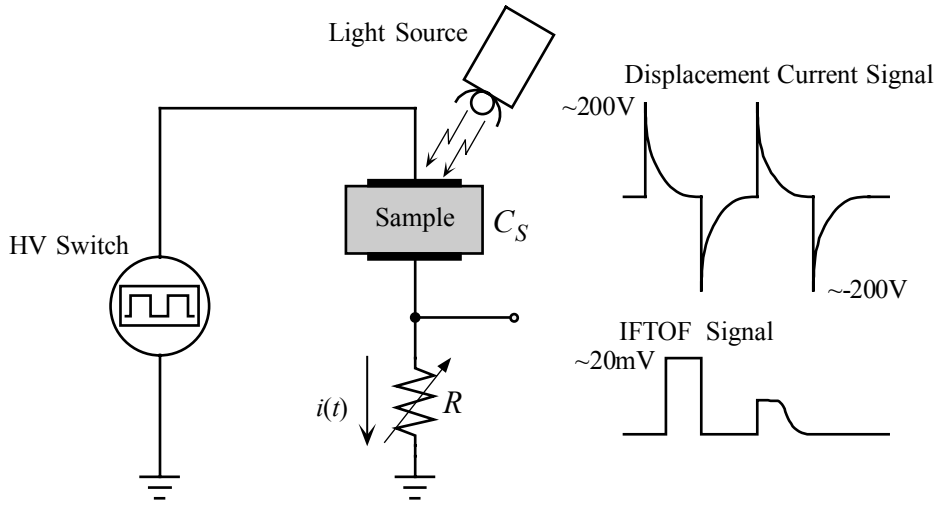

Figure 4.5: The rapid switching of the HV Bias generates a large displacement current that must be dealt with for the IFTOF technique to work properly.

Several methods for eliminating this displacement current have been used. Kasap and coworkers used a complementary pulsed bias technique [37]. This technique, while allowing the use of grounded supplies and thus good shielding, required that two high voltage supplies be switched at the same time. This is difficult to do as bias voltage increases and switching times decrease. Later, Polischuk and Kasap used a floating Schering bridge network to use a single high voltage supply to apply a large bias up to 1 kV [45]. However, the voltage supply in this case had to be a floating supply, generating stray capacitances that made balancing the bridge difficult.

For the experiments done here, a grounded bridge network was used to deal with the displacement current. This system is shown in Figure 4.6. The variable capacitor, C_N, is adjusted to match the sample capacitance C_s. Once the capacitances are matched, the two transients will be equal, and by using a differential amplifier the transient photocurrent signal, which will only occur on the sample side, can be extracted. Unfortunately, the large transient signals create harsh restrictions on the amplifier; it needs a very large CMRR (~100dB) over a large bandwidth, and it must be able to withstand the large input voltages without saturating. To reduce amplifier constraints, two back-to-back rectifiers are added across the sampling resistors ($D_1 - D_4$). The rectifiers will limit the transient signal to 0.7V (the voltage drop across a forward biased

diode), thus preventing the amplifier from going into saturation. Consequently, only about 60dB CMRR is needed with this setup, as long as the sampling resistors are closely matched.

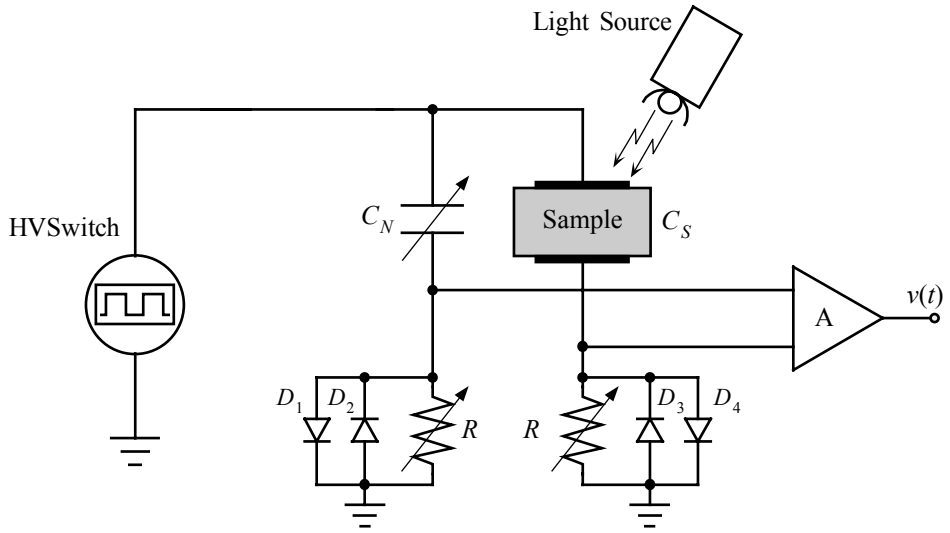

Figure 4.6: A grounded bridge network to eliminate the large displacement currents caused by switching the high voltage in IFTOF measurements.

4.4 TOF/IFTOF Experimental System

4.4.1 Overview

The TOF/IFTOF system used in the experiments is depicted in Figure 4.7. The system uses an internal EMCO high voltage DC-DC converter to generate the high voltage for the experiments; the voltage is applied through a fast switching HV HEXFET switch. To eliminate the switching transients, a grounded bridge network is used containing a high voltage open-air variable plate capacitor (C_N) along with MUR120 ultra-fast rectifiers across the sampling resistors. A differential amplifier connected to the bridge extracts the transient photocurrent signal; to protect the amplifier from the transients, a CMOS analog switch shorts the inputs of the amplifier while the high voltage is being switched. The light source used for the system was a xenon flash passed through a blue filter. The signal was captured on a Tektronix TDS210 digital oscilloscope.

A computer running custom software on Windows 98 controlled the experiment. The user could specify the timing for the experiment, and the pulses to control the various parts were generated using a PCI-CTR05 timer/counter board, along with some additional electronics. The waveforms from the experiment were passed from the oscilloscope to the computer using the serial port and were saved for further analysis.

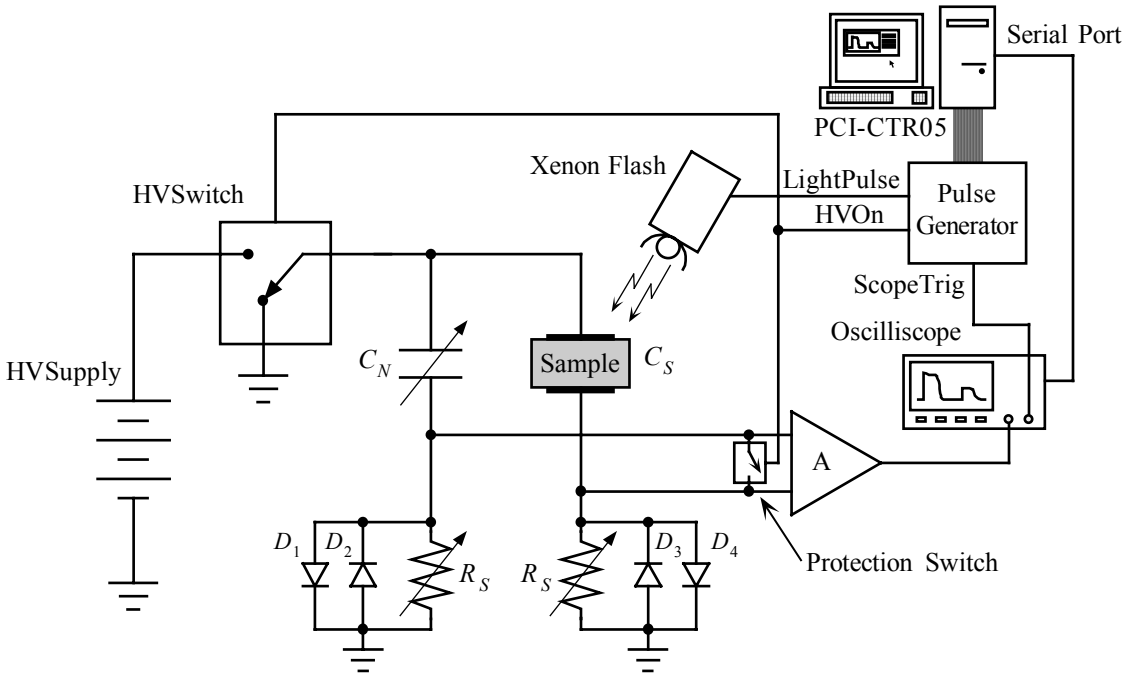

Figure 4.7: The TOF/IFTOF system used in the experiments. The system uses an internal HV supply and a grounded bridge network to reduce switching transients. Timing for the experiment is controlled by the computer and the transient response is recorded onto a connected TDS210 oscilloscope.

The HV supply, HV switch, bridge network, and sample holder were all contained in a metal experimental box that could be sealed to allow no light to enter. The pulse generator and amplifier were kept in separate metal boxes. Co-axial cables provided external connections between parts of the apparatus, such as trigger signals, as well as the power supply lines for the main apparatus.

Through careful adjustment of the variable capacitor, it was possible to eliminate most of the displacement current signal, but not all. The samples of a-Se have a slight dark current that will increase with increasing applied field. This dark current also typically decays with time. This dark current is equivalent to having a time-dependent

resistor $R_s(t,F)$ in parallel with the sample that is dependent on both time and the applied field. This $R_s(t,F)$ combined with the sample capacitance (C_s) make it extremely difficult to completely nullify the transient signal. Therefore, the system was adjusted until the effects of the switching transients were minimized, on the order of the transient photocurrent signal. To obtain a switching-transient free signal, a digital subtraction method was used. Each measurement involved the capture of two waveforms: one signal involving no light pulse to determine the switching transients, and another signal with the light pulse to capture the transient photocurrent signal. The net displacement current-free signal was obtained by subtracting the two waveforms digitally in the computer. The digital subtraction method has successfully been utilized for capturing IFTOF signals before [11, 44].

A typical IFTOF waveform generated by the system is shown in Figure 4.8. The waveform shown is for holes in a 105 μm thick sample of a-Se:0.5%As, demonstrating how the digital subtraction method has completely removed the displacement current effects. In this case, the interruption time is 10 μs and an estimated hole lifetime from this waveform is 20.7 μs. The interruption time may appear to be slightly different than indicated, but this slight delay is actually generated by the protection circuitry for the amplifier.

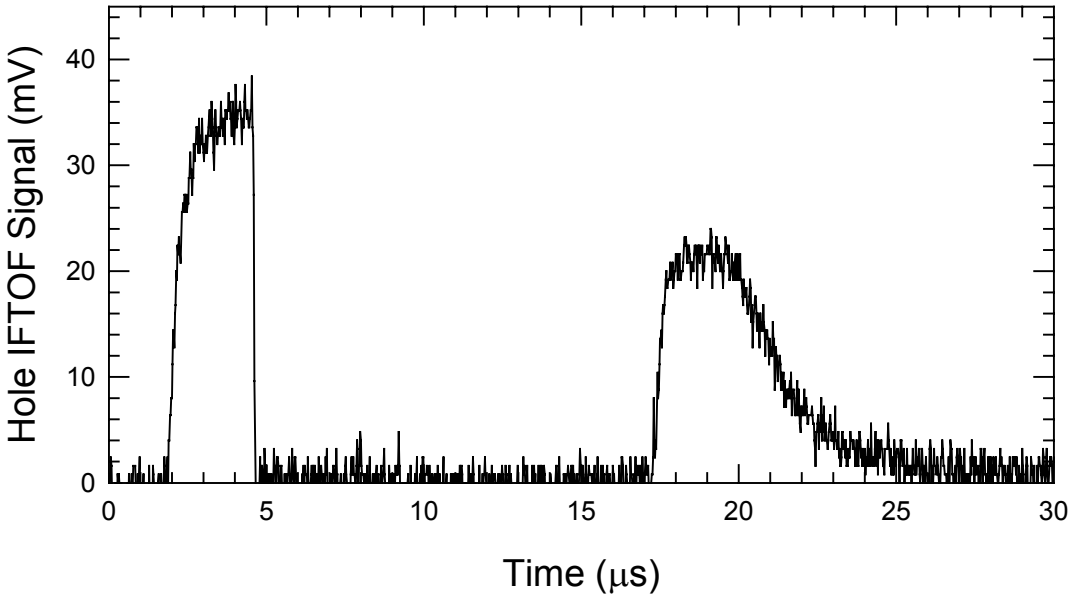

Figure 4.8: Typical displacement current free IFTOF signal for holes after the digital subtraction has been performed. This sample was a-Se:0.5% As with a thickness of 105 μm.

4.4.2 Pulse Generator

The pulses used to control the IFTOF apparatus were generated using a PCI-CTR05 counter board installed on the PCI bus of a computer combined with some external timing circuitry. The counter board is based on an AMD9513 timer/counter chip containing 5 programmable up/down counters. The counter board was controlled using Universal Libraries provided with the board to enable high-level control of the timers. Specific C++ code for controlling the timer/counter board was generated and integrated into the TOF/IFTOF GUI to easily control the experiment.

The output of the timer/counter board was passed to the pulse generator circuitry to tweak it to control the TOF/IFTOF apparatus. The pulse generator circuitry is shown in Figure 4.9. The circuit was kept in a small aluminum box separate from the IFTOF apparatus and connected to the computer using a ribbon cable and 39-pin D-sub connector. The PC provided the 5V supply for the circuitry. A manual control switch for

the HV switching was included in the form of a SPDT switch with a center not connected position. The switch provided 3 manual settings for the HV: on, off and pulsed (used for normal IFTOF operation). An LED connected to the HV control line provided visual feedback coinciding with when the HV was applied to the sample.

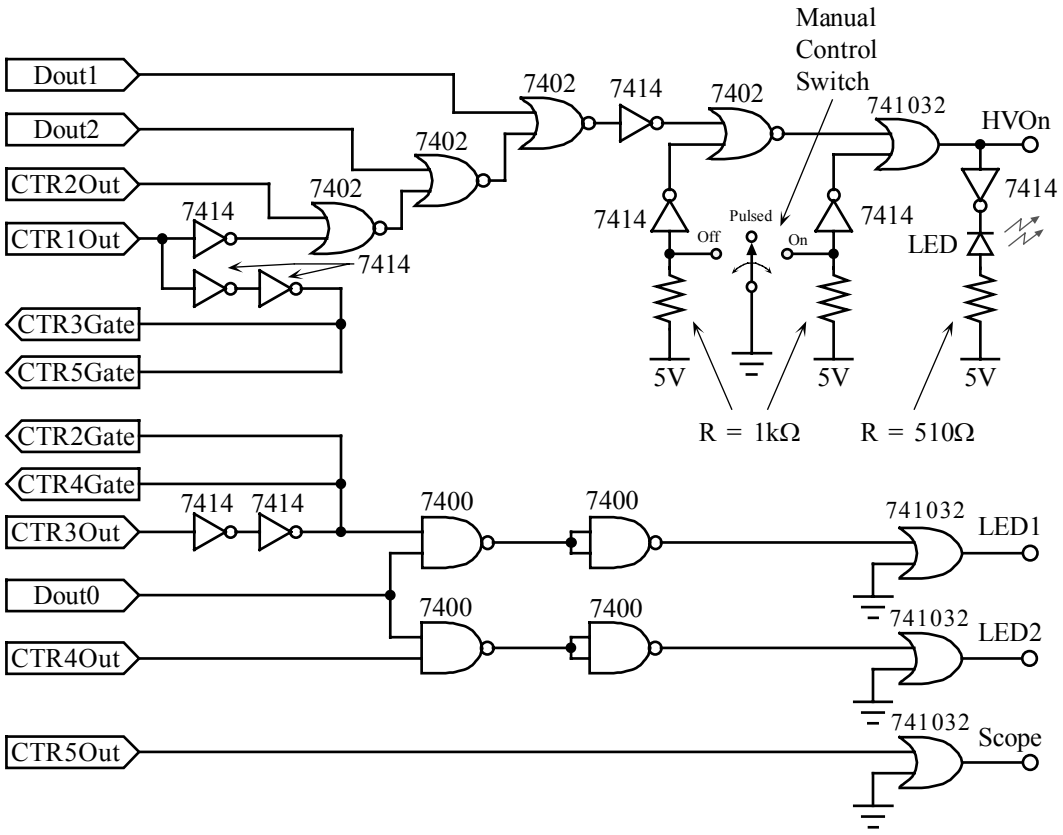

Figure 4.9: The pulse generator circuit used to interface the PCI-CTR05 timer board and the IFTOF apparatus.

The timing of pulses used in a typical IFTOF experiment, assuming the manual control switch is set to "pulsed", is shown in Figure 4.10. The "HVOn" signal output controls the application of the HV bias to the sample. CTR1 controls a general application of the high voltage; it turns on for the duration of the experiment. A delay time of t_{HVPreset} before the start of the experiment allows the switching transients to completely settle out before the experiment starts. Following this, the pulse to trigger the oscilloscope and the pulse to spark the xenon flash are generated. The scope trigger has a pulse width of 300 μs, and the pulse width for the xenon flash is user-defined in the GUI

with a width of t_{LED1On} (set to 3000 μs for all experiments). These pulses firing coincide with the beginning of the experiment.

For the TOF experiment, the HVOn signal is not interrupted, and is therefore constantly on for a sufficient time to ensure all of the charge carriers are collected. In the IFTOF experiment, the interruption is controlled by CTR2 and two user-defined variables: t_d and t_i. The first variable (t_d) is a delay from the start of the experiment until the interruption and the second (t_i) sets the length of the interruption time for the experiment. Following the interruption, the bias is re-applied and remains on for a sufficient time again to ensure all the charge carriers are collected.

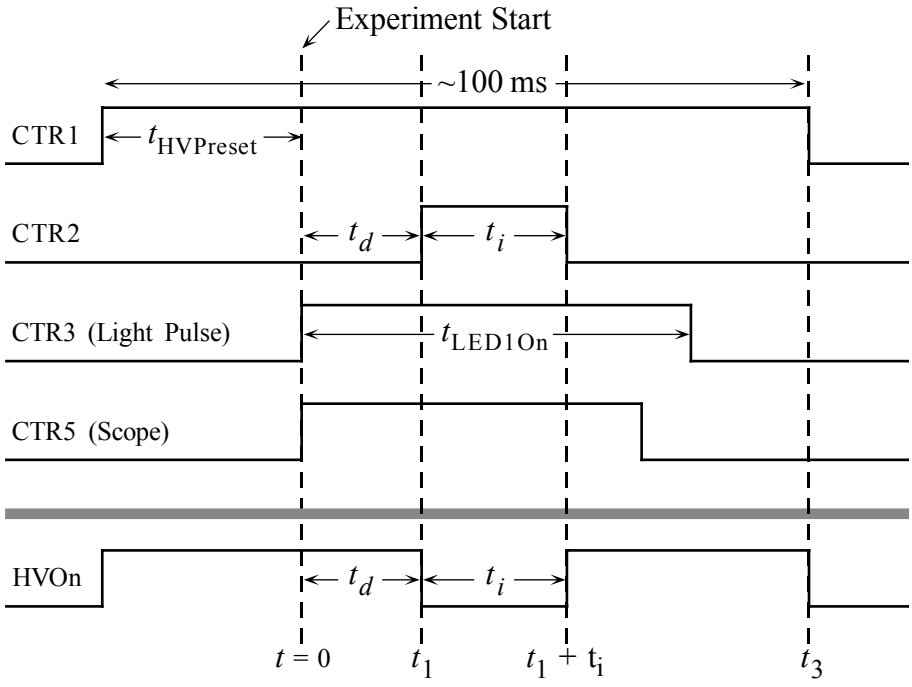

Figure 4.10: Timing of Pulses using in a typical IFTOF experiment, manual control switch is set to "Pulsed"

4.4.3 Xenon Flash

To generate a short pulse of light for a photoexcitation pulse, a xenon flash source was used. Xenon flash bulbs from EG&G and Hammamatsu with a short arc length (1.5 mm) were used with specialized circuitry to obtain a short pulse of light. The circuitry

for obtaining the short pulse from the xenon flash lamps is shown in Figure 4.11. The high voltage capacitor C_H, connected across the electrodes of the xenon flash is charged up to around 1600V. The capacitor C_T is also charged up, and will discharge when the silicon controlled rectifier (SCR) is triggered by the triggering circuitry. As C_T discharges, a high voltage spike (5-7 kV) is applied between the trigger probes of the xenon flash bulb, causing some of the xenon gas in the spark gap to ionize, lowering the impedance of the spark gap. When the impedance has lowered enough, C_H will discharge through the spark gap, causing a light pulse. The light pulse travels through a $CuSO_4$ solution to filter out the undesirable red wavelengths from the pulse. This light pulse from the Xenon flash apparatus will then pass through a neutral density filter, if necessary, before passing through a focusing lens and a blue filter to make the light pulse in the blue spectrum only. The light is coupled into a fiber optic cable for transfer into the TOF/IFTOF apparatus. This focusing system is shown in Figure 4.12. It should be noted that the xenon flash circuitry is contained within well-grounded shielding and is separate from the TOF/IFTOF box; the triggering connection is done via optocouplers to minimize RF feedback and hence disturbance to the scope.

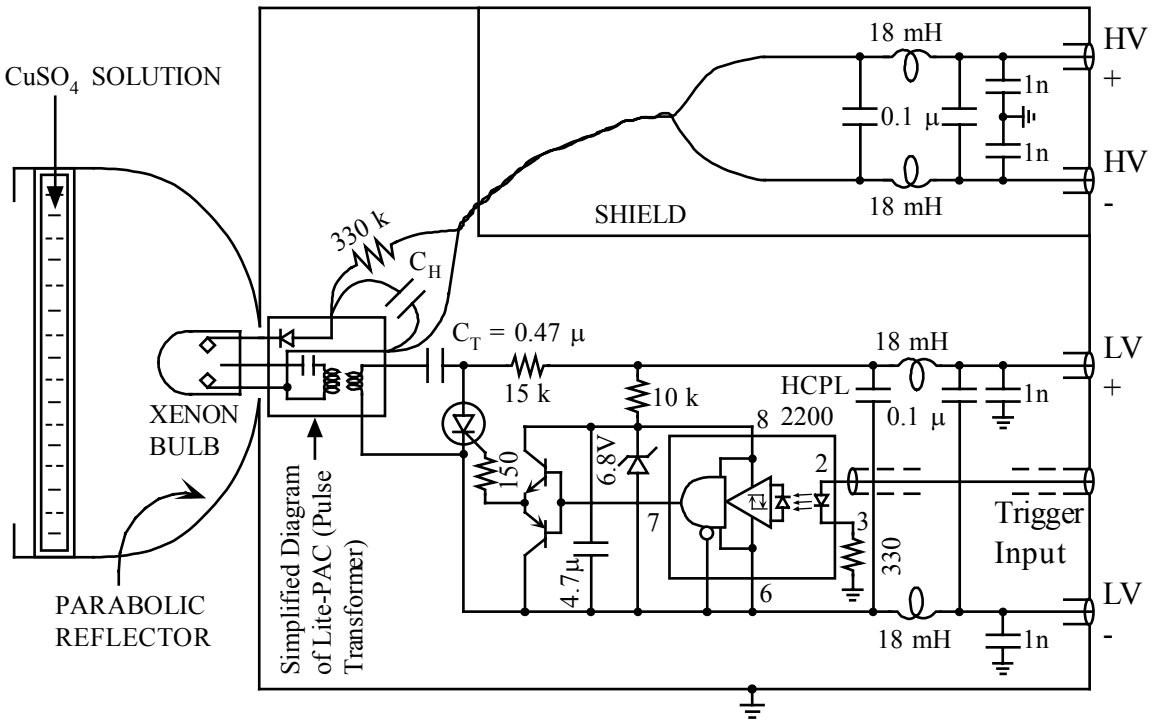

Figure 4.11: Schematic sketch of the xenon flash circuit.

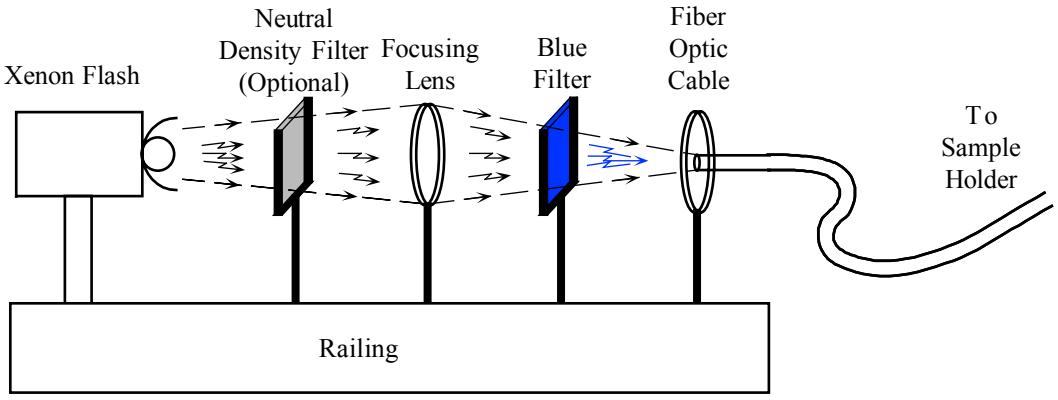

Figure 4.12: Optical system used to filter and focus the light pulse from the xenon pulse. The resulting blue light pulse is transferred to the TOF/IFTOF system by way of a fiber optic cable.

4.4.4 High Voltage Switch & Supply

A large bias is required to measure the mobility of low mobility semiconductors such as a-Se. For holes, a typical mobility is ~0.12 cm^2/Vs and for electrons, ~3.0×10^{-3} cm^2/Vs. When this is combined with relatively thick samples, ~100μm, a fairly large bias is needed, up to 1kV. The transit times for holes and electrons are a few μs, so the IFTOF system must have very rapid rise and fall times <0.1 μs.

The internal high voltage bias was supplied with the system depicted in Figure 4.13. The EMCO C20, a DC/DC converter, generates a high voltage up to 2kV with 0-0.5 mA of current from a 15V input. The output is varied with the use of a 10-turn 100k potentiometer supplying a control voltage of 0-5V, relating to an output of 0-2kV. On the output of the C20 is a V1G package from EMCO, a 1000:1 balanced voltage divider. This package outputs the exact bias voltage to be read by a connected multimeter, though at a significantly reduced voltage (1V on multimeter is equivalent to 1kV output). A switch to select an attached external HV supply was also included, but never used in this work.

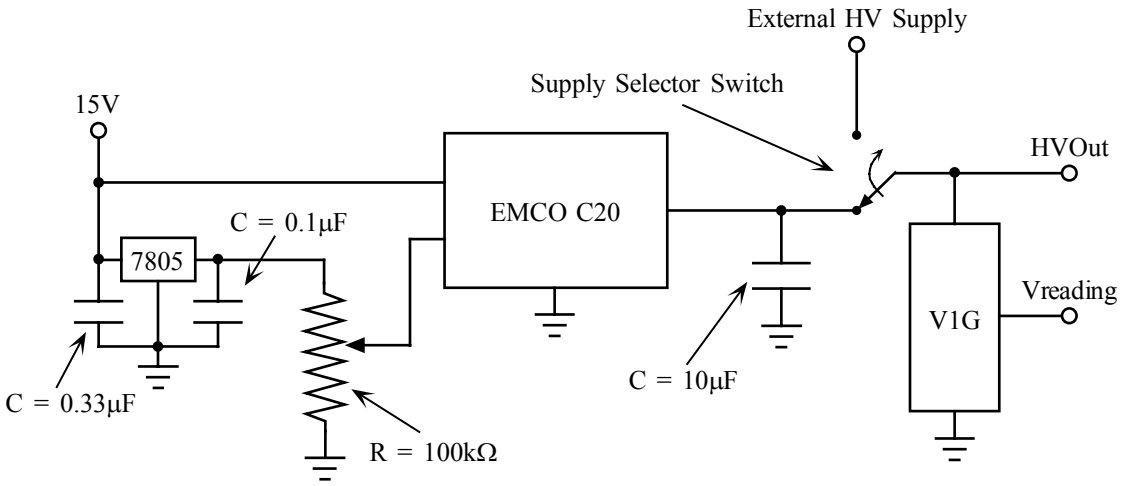

Figure 4.13: A high voltage supply capable of delivering 2KV

Figure 4.14 shows the high voltage switch designed for the IFTOF experiment. It uses two fast n-channel IRFBG30 MOSFETs connected in a totem pole configuration. The MOSFETS are driven by two HCPL-3140 optocoupler MOSFET drivers, which also serve to isolate the control circuitry from the high voltages being used in the rest of the system. A simple transformer-based DC supply regulated to 18V is used to provide a power supply to the higher optocoupler; this 18V line must float on the output of the high voltage switch. A simple grounded 18V supply provides power for the other optocoupler.

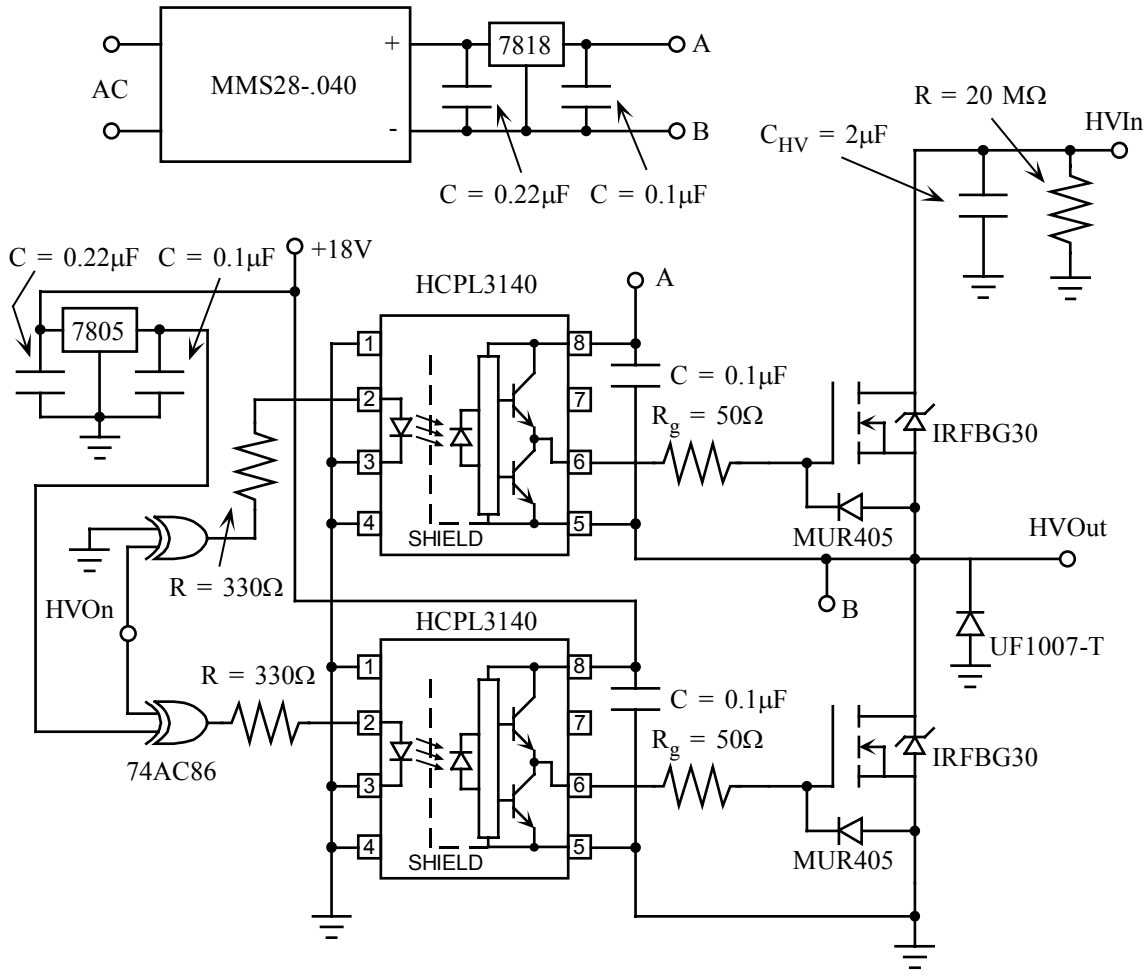

Figure 4.14: A high voltage switch capable of switching 1KV

The HV switch itself functions as a SPDT switch, with output of either 0V or whatever bias voltage is desired. On the input of the high voltage switch, a +5V signal on HVOn will cause the high voltage switch to turn on and pass the set bias voltage on to the rest of the apparatus. A simple system using XNOR digital logic ensures that only one of the two MOSFETS is on at once. The HV switch and the connected supply can only generate a positive bias. In order to generate a negative voltage for electron TOF/IFTOF measurements, the connections to the sample must be swapped. This is accomplished with the use of a high voltage DPDT switch connected so that it can swap which contact will receive the high voltage, either the “top” or “bottom” electrode.

4.4.5 Amplifier

The differential amplifier for the experimental apparatus is shown in Figure 4.15. The amplifier consists of two stages to generate 16 dB of gain on the photocurrent signal. The first stage provides the differential amplification. This is provided from an Analog Devices AD830 amplifier, a single package differential amplifier with unity gain bandwidth of 85 MHz and a CMRR of 60dB at 4 MHz. The second stage is a non-inverting amplifier using a high speed Analog Devices AD827 amplifier to drive the output through the coaxial cables to the oscilloscope. This generates 16 dB of gain on the photocurrent signal to bring it above the noise floor of the oscilloscope.

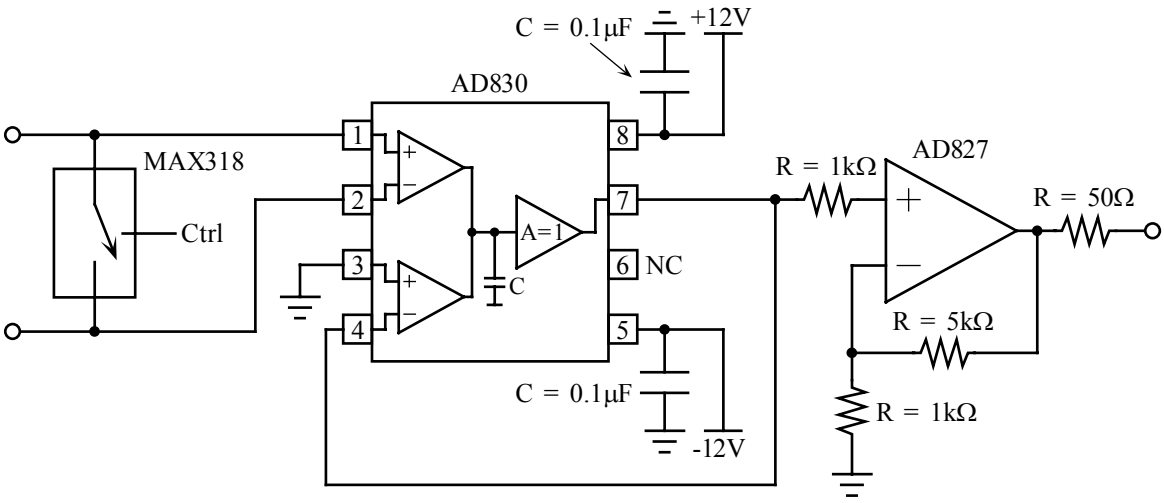

Figure 4.15: A two-stage differential amplifier with 16dB of gain.

Protection from the amplifier is provided with the use of a Maxim MAX318, a normally open SPST CMOS analog switch. The switch is kept closed during the switching of the high voltage and for a short time afterwards; the timing is controlled using an LS123 monostable multivibrator and an LS74 positive-clocked D flip-flop. The circuitry to generate the timing pulse is shown in Figure 4.16 (a) and the timing of the pulse is shown in Figure 4.16 (b). The delay from high voltage switching until the amplifier is activated (t_s) is controlled by adjusting the variable resistor in the resistor-capacitor network that determines the pulse width from the multivibrator. Not shown in

the figures are two small diodes (1N914) connected in series with the supply pins on the MAX318 to provide overvoltage protection for the switch.

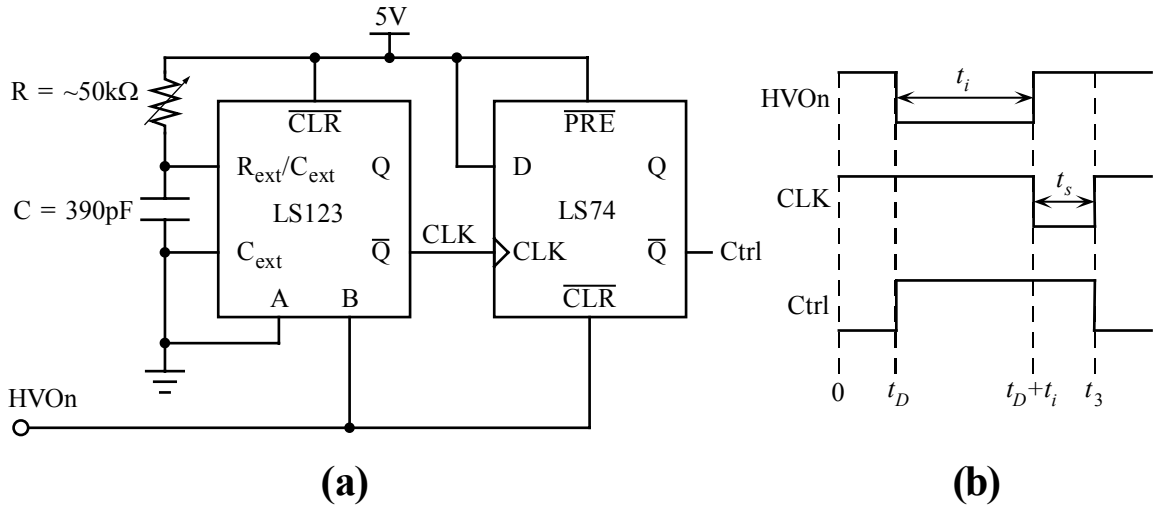

Figure 4.16: A circuit to generate a delay to control the application of the amplifier protection. The circuit is shown in (a), the timing diagram is shown in (b). Adjusting the 50k potentiometer controls the delay, t_s.

4.4.6 Signal Capture and GUI

The photocurrent signal from the experiment was captured using a Tektronix TDS210 digital oscilloscope with a sampling rate of 1GS/s. Before capturing the signal, the user could freely adjust the horizontal and vertical setting to enable the best possible view of the captured signal. The captured signal was then transferred to the computer using the serial port. To limit noise on the waveforms, the oscilloscope bandwidth was limited to 20 MHz.

Custom software was programmed in C++ to control the experiment with the use of a graphical user interface (GUI). The GUI for the program used in shown in Figure 4.17. The user has full control over the delay before interruption, t_d, and the interruption time, t_i. Also included was the ability to vary the pulse width for different light sources (such as LEDs) and the ability to control a second light source. Though these functions were unused in this work, the apparatus is capable of using these features at a later date. In this work, the pulse time for the first light source (LED1) was set to 3000 μs for all

experiments; pulse time for the second light source (LED2) was set to 0 to disable the feature. In a normal experiment, the user set the desired delay and interruption time (both set to 0 for regular TOF experiments) and clicked the Run button to start the experiment. For IFTOF experiments, the apparatus was run twice: first without any photoexcitation to establish the remaining transients, which were saved into the computer, followed immediately by another run with photoexcitation to capture and save the transient photoconductivity signal. With both signals saved, the two waveforms were subtracted in the software to generate the transient-free waveform that would be displayed in the GUI. The final signal could be saved into tab delimited text files for export and analysis in other programs, such as Excel and Matlab.

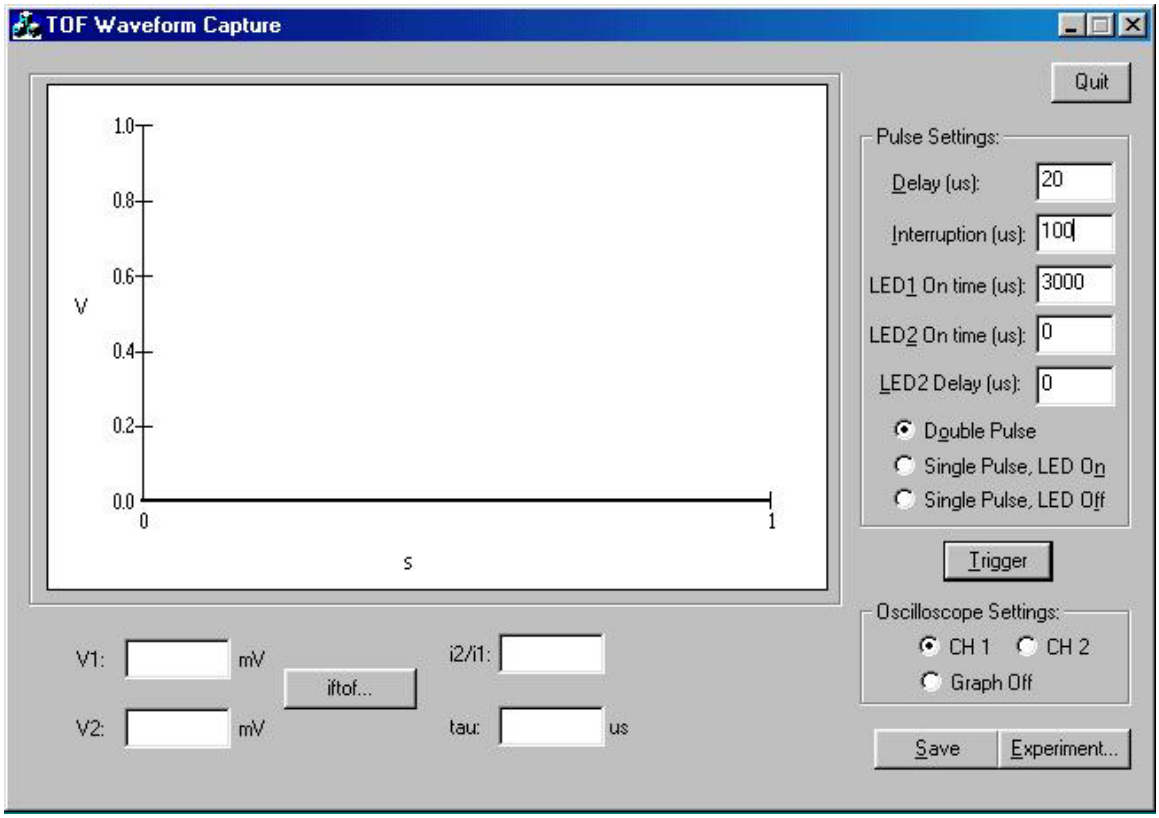

Figure 4.17: Graphical user interface (GUI) used to control the TOF/IFTOF experiment.

4.5 Annealing Chamber

In order to measure the relaxation of the samples, they needed to be annealed. The apparatus used for annealing is shown in Figure 4.19. The sample was placed on the sample holder and then the top was placed on the container to seal out any ambient light. An Omega Cni3252-C24 temperature controller in PID mode using a 50 Ω heater controlled the heating of the sample. To eliminate the temperature overshoot caused by PID controllers, the initial temperature setpoint was set at 53.5 ºC. When the sample reached a temperature of 55 ºC from the overshoot, the temperature setpoint was changed to 55 ºC to be maintained for the duration of the annealing. As can be seen in Figure 4.18, this almost completely eliminated the overshoot. Once the sample had reached this temperature, it was maintained at this temperature for a minimum of 30 minutes. After which, the heating was removed and a water-cooling system was applied to cool the system down to room temperature as quickly as possible. The sample was left with the water cooling system running for 20 minutes, at which point the cooling was switched off and compressed air was used to maintain the cooling, as well as to remove any leftover water from the system. The air was applied for 10 minutes, and the sample was then removed to rest in the dark before measurements would begin.

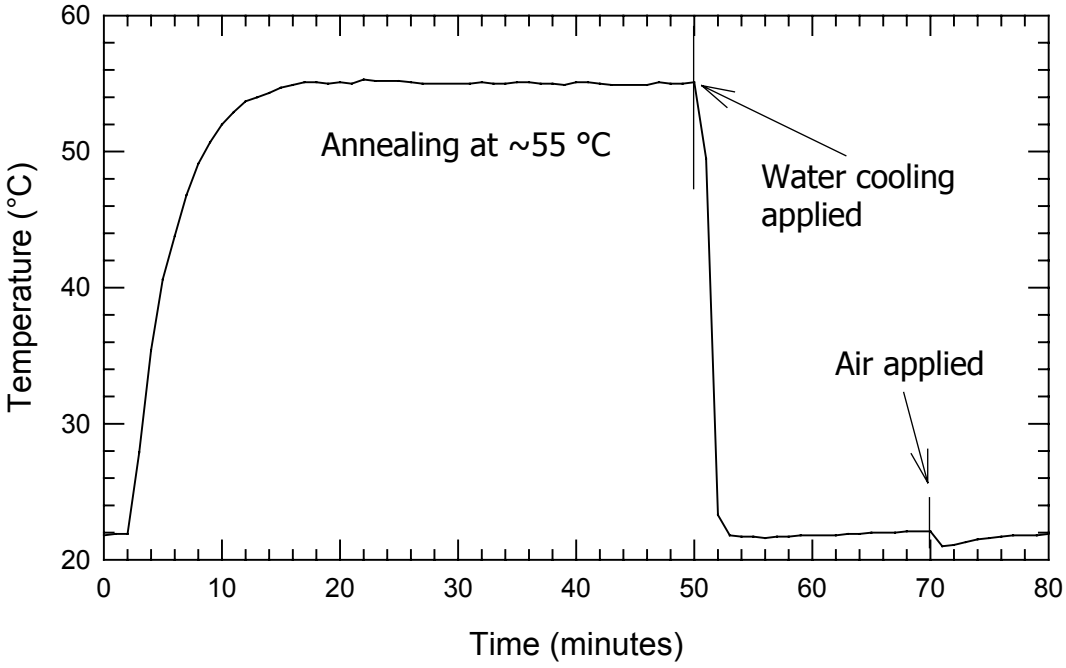

Figure 4.18: Typical Temperature Curve for an Annealing Experiment

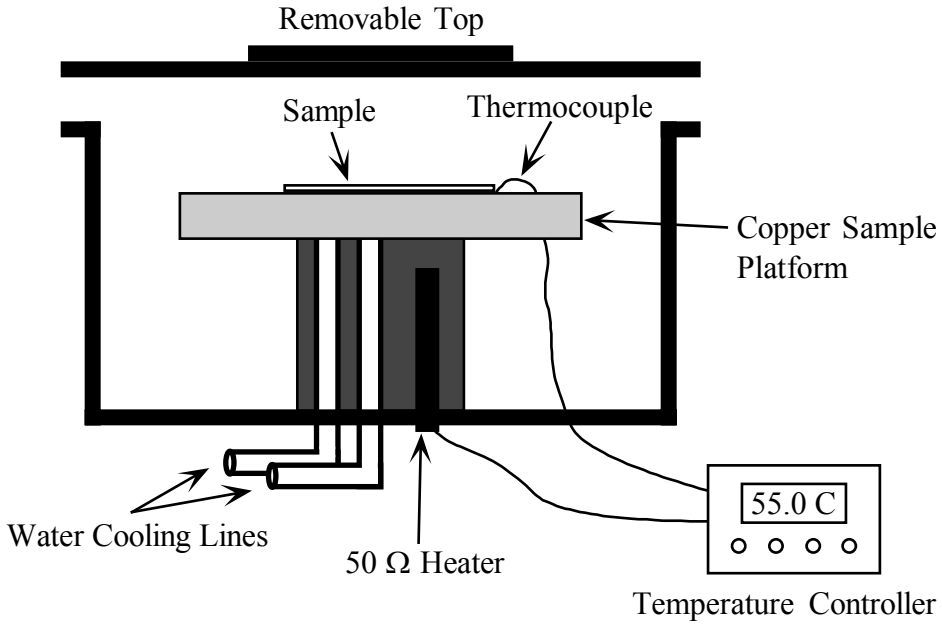

Figure 4.19: Annealing chamber used to anneal samples for relaxation. The water-cooling lines are actually interspersed inside the copper sample platform.

4.6 Summary

In this chapter, the experimental procedures used throughout the course of this work were outlined. The samples used in the experiments were prepared using conventional vacuum techniques, followed by having a semi-transparent gold top contact sputtered on. In the TOF experiment, the drift mobility is found by examining the duration of the transient pulse generated by a carrier charge sheet drifting across the sample. In the IFTOF experiment, the bias used to cause the carrier sheet to drift is removed at some point while the carriers are within the sample and later reapplied. By examining the ratio of the transient photocurrent after the interruption and before the interruption, the carrier lifetime can be found. The rapid switching of the high voltage bias creates difficulties in implementation however, as the displacement currents from switching can completely dwarf the photocurrent signal. To overcome this, a grounded bridge network was used to eliminate the displacement carrier, and some high-speed rectifier diodes used in conjunction with a differential amplifier extracts the photocurrent signal. A detailed description of the TOF/IFTOF system used in these experiments was also outlined. The system used for annealing the samples in this work was also described.

5. Results and Discussion

5.1 Introduction

In the previous chapters, the theory behind the TOF and IFTOF experiments was discussed, followed by the description of the experimental setup. In this section, the results of the experiments involving the relaxation of several a-Se alloys using these experimental methods will be discussed. The charge carrier drift mobility and trapping time were measured using the TOF and IFTOF techniques. The product of the two gives the charge carrier range, which determines how far a created charge can travel, on average, in an x-ray photoconductor. From a set starting point, either after sample creation or immediately after annealing, repeated TOF & IFTOF measurements were performed to observe how these parameters change as the sample relaxes ("ages"). After multiple measurements, the measurements were examined as a set to see if a pattern emerged. This pattern was checked for several different compositions for both electrons and holes.

5.2 Measuring charge carrier transport properties in a-Se

The TOF and IFTOF techniques are quite useful in measuring the charge transport properties of a-Se. Both techniques observe the transient response of a sample under bias after it has been pulsed with a light source. The bias determines the carrier that will travel across the sample, either electrons or holes; the other carrier will be immediately neutralized at the top electrode. In the TOF experiment, the applied bias is constant and the carrier drift mobility, μ, corresponds to the width of the I-mode pulse. In the IFTOF experiment, the applied bias is completely removed while the carriers are drifting through the sample. This causes a break in the drifting of the carriers, and a subsequent drop in the photocurrent signal. Once the bias is re-applied, the drifting of the carriers resumes, though the magnitude of the photocurrent will be decreased due to some carriers being

trapped during the interruption. The average lifetime of the carriers in the sample, τ, is found by examining the ratio of the photocurrent after the interruption to that before the interruption.

The analysis of the TOF waveforms revolves around the assumption that the electric field through the sample is uniform. Once the bias is applied, a small amount of charge is injected into the sample and becomes trapped during drift. Eventually, there are enough trapped charges to alter the electric field in the sample. This occurs at a time known as the transition time, t_{sc}, on the order of ~100ms for a-Se [28]. Before this time the electric field can be assumed to be uniform, so the photoexcitation for TOF experiment is started a few milliseconds after the bias is applied to ensure uniform bias.

If the photoexcitation occurs after t_{sc}, then the internal field will no longer be uniform. The internal field will be altered by the trapped space charges, determined from the Poisson equation, $dE/dx = \rho/\varepsilon$ where ρ is the density of the trapped space charge. The nonuniform charge causes the photocurrent to experience significant change, demonstrated by Kasap and Juhasz [41]. Repeated TOF experiments on the same sample can have a similar effect over a long period of time, as shown in [11]. To eliminate any bulk space charge in the experiments, the sample was shorted and pulsed several times with light. The photogenerated carriers recombine with any trapped space charges to eliminate them. Thus, in the experiment, the sample was discharged and rested for ~5 minutes between TOF/IFTOF measurements.

In order to determine a sufficient resting time between measurements, a quick experiment was performed. The IFTOF experiment was performed on a sample of a-Se, a-Se:0.5%As + 40 ppm Cl, and was repeated with different resting times. The results of the experiment are shown in Figure 5.1. As the resting time between measurements was increased, the spread in the fractional recovered photocurrent was decreased. The spread decreased from over 20% with only one minute resting to being consistently under 8% spread for resting times of 5 minutes or more. From these results, a resting time of 5

minutes between measurements was selected to balance a minimal spread while still being able to repeat the measurements quickly.

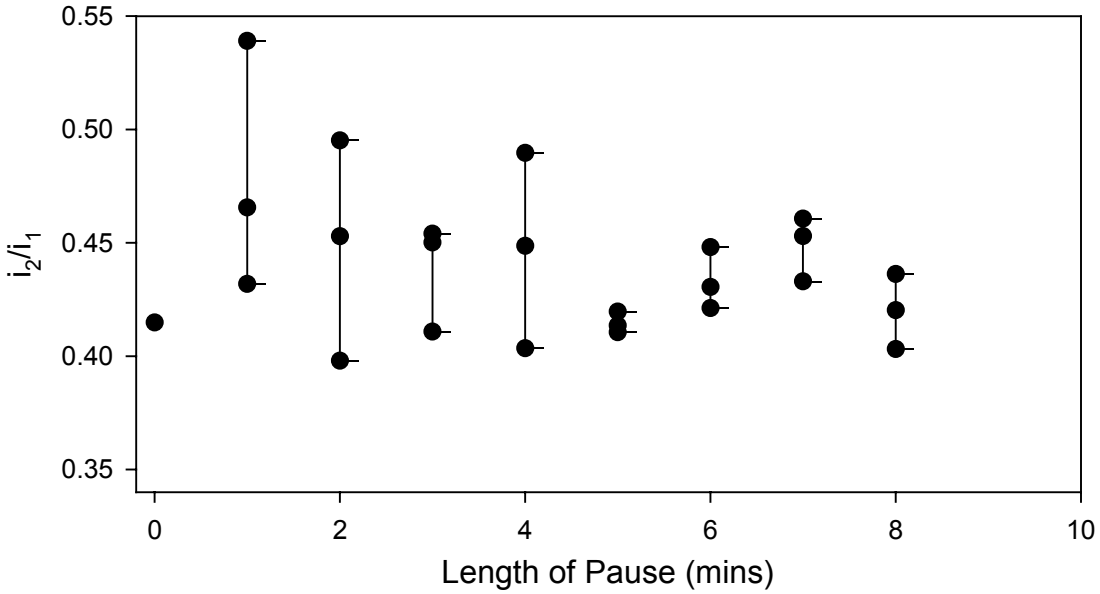

Figure 5.1: Fractional recovered photocurrent as it varies with resting time between IFTOF firings. $t = 0$ corresponds with the initial measurement on a fully rested sample.

Typical I-mode TOF waveforms for both holes and electrons are show in Figure 5.2. The samples used have a composition of a-Se:0.5% As with a sample thickness of 105 μm for holes and 86 μm for electrons. In the case of holes, shown in Figure 5.2 (a), the shape of the waveform is nearly rectangular, indicating that the bulk charge has had no effect, and that trapping during the whole transit time is minimal. The electrons shown in Figure 5.2 (b), on the other hand, have an initial spike that settles down to a constant value before the transit time.

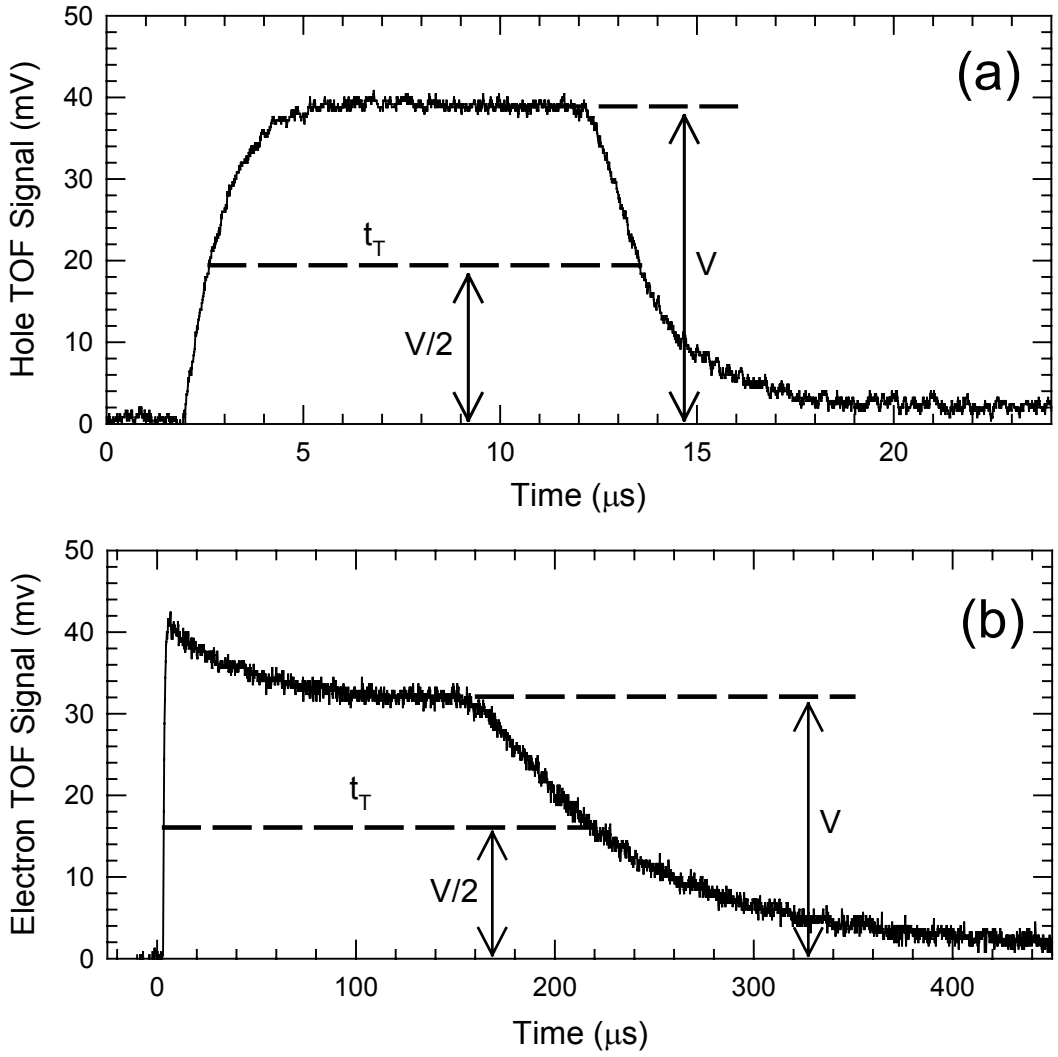

Figure 5.2: I-mode waveforms for samples of a-Se:0.5% As. (a) Hole waveform captured with an applied field of 1 V/μm with a thickness of 105 μm; transit time was measured to be 8.5 μs. (b) Electron waveform captured with an applied field of 1.93 V/μm with a thickness of 86 μm; transit time was measured to be 228.2 μs.

In Figure 5.2, it is apparent that for both electrons and holes there is a photocurrent tail at the end of the waveform. This is due to the spreading of the charge packet of carriers as it travels through the sample. The spread is due to two fundamental effects: (i) multiple trapping transport and (ii) coulombic repulsion between the injected photocarriers. This spreading, and therefore the length of the tail, increases with a longer transit time, t_T, as seen in the electron TOF waveform compared to the waveform for

holes. With this spread of the photocurrent tail, having a set method for determining the transit time, t_T, is helpful. For these experiments, the half-peak magnitude method was used for determining the transit time [11]. This method takes the peak magnitude for the waveform, and then finds the transit time from the leading edge of the waveform and the point on the tail that is at one half the peak magnitude, as show in Figure 5.2. The "maximum" point used for the TOF waveforms was the "knee" in the waveform, immediately before the tail.

Once the transit time has been determined, the carrier mobility can be found from:

$$\mu = \frac{L^2}{Vt_T} \tag{5.1}$$

where L is the sample thickness, V is the applied voltage, and t_T is the transit time. From Figure 5.2 (a), for a sample of a-Se:0.2% As with thickness $L = 105 \pm 3$ μm, the hole transit time was found to be $t_T = 8.5 \pm 0.2$ μs, resulting in a hole mobility of $\mu_h = 0.124 \pm 0.004$ cm^2/V·s. For electrons the sample thickness was $L = 105 \pm 3$ μm, the transit time was $t_T = 228 \pm 5$ μs, resulting in an electron mobility of $\mu_e = 2.0 \pm 0.2 \times 10^{-3}$ cm^2/V·s. All mobility calculations in this work were done in this manner.

IFTOF measurements were used to determine the mean carrier lifetime in a-Se samples. In the IFTOF experiment, after a time t_1, the applied field is removed and the drift of the carriers is halted within the bulk of the sample. Here, the carriers are able to interact with the trapping centers and some are lost. When the bias is re-applied at time t_2, the drift of the carriers resumes, but the magnitude of the photocurrent is decreased due to the loss of some of the carriers during the interruption. The number of carriers lost to trapping during the interruption can be found by measuring the magnitude of the photocurrent before and after the interruption, since $i(t_2)/i(t_1) = n(t_2)/n(t_1)$. With a set of traps with a defined capture time of τ, it can be shown that $n(t_2)/n(t_1) = \exp(-t_i/\tau)$ where $t_i = t_2 - t_1$ is the interruption time. Several measurements of $i(t_2)/i(t_1)$ are taken for varying interruption times and are plotted semi-logarithmically. This plot will generate a straight line, the slope corresponding to the deep trapping lifetime, τ.

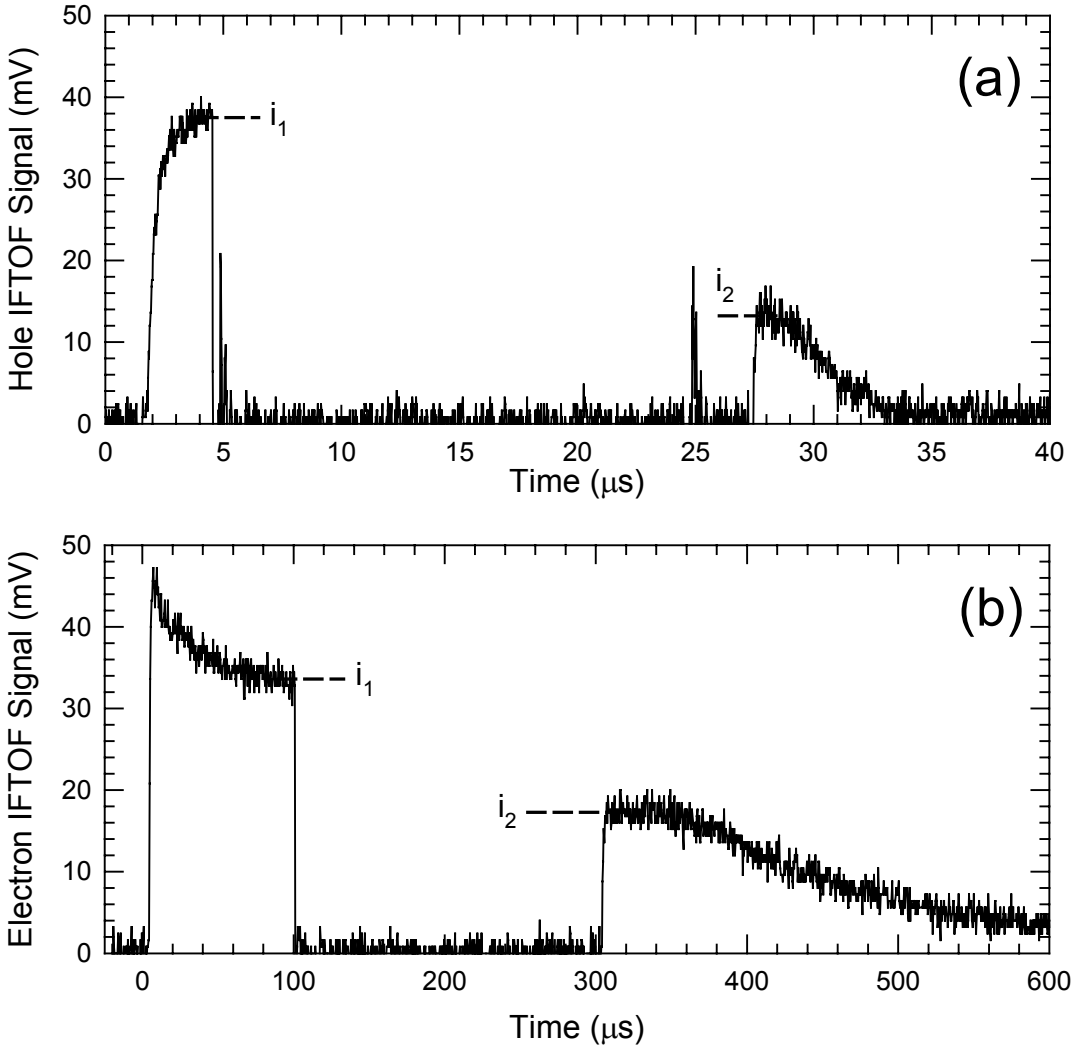

Figure 5.3: IFTOF waveforms for samples of a-Se:0.5% As. (a) Hole IFTOF waveform with interruption time of 20 μs. (b) Electron IFTOF waveform with interruption time of 200 μs.

Typical IFTOF waveforms for both holes and electrons are show in Figure 5.3; the samples used were a-Se:0.5%As with a thickness of 105 ± 3 μm for holes and 86 ± 3 μm for electrons. The interruption time in Figure 5.3 (a) was 20 μs for holes, and in Figure 5.3 (b) was 200 μs for electrons. Note that the interruption time in Figure 5.3 (a) appears slightly longer than 20 μs; this is due to a slight delay introduced in the protection circuit for the amplifier. The IFTOF measurements were repeated on the same sample with varying t_i in order to get different values for the fractional recovered photocurrent $i(t_2)/i(t_1)$. A semilogarithmic plot of the fractional recovered photocurrent

vs. t_i was plotted and is shown in Figure 5.4. As expected, the plot demonstrates an exponential dependence, indicated by a straight line as the best fit line. The hole and electron lifetimes found from the slope were found to be 19.9 ± .8 μs for holes and 375 ± 10 μs for electrons.

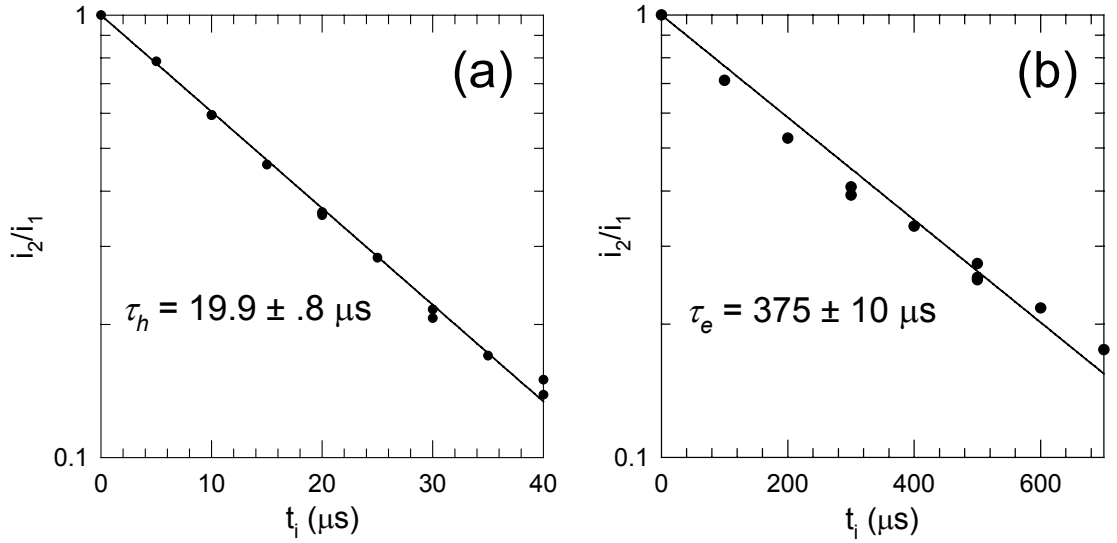

Figure 5.4: Semilogarithmic plots of fractional recovered photocurrent i_2/i_1 vs. interruption time for samples of a-Se:0.5% As. (a) The resulting hole lifetime, τ_h, was 19.9 ± .8 μs. (b) The resulting electron lifetime, τ_e, was 375 ± 10 μs.

It is important to note that this exponential dependence is consistent for varying magnitudes of the lifetime for both holes and electrons. This can be seen in Figure 5.5 for holes and Figure 5.6 for electrons. In both cases, even though the resultant lifetime changes, the exponential dependence remains consistent. These fits all follow the form $i_2/i_1 = \exp(-t_i/\tau)$. Plotting i_2/i_1 vs. t_i/τ can therefore further demonstrate that the fits are exponential; the closer a fit is to a true exponential, the closer these plots will be to a plot of $y = \exp(-x)$. These plots can be seen in Figure 5.7 for holes, with $R^2 = 0.9906$, and in Figure 5.8 for electrons, which has $R^2 = 0.9749$. The high quality of fit given by the R^2 value proves that the carrier lifetimes do have an exponential dependence.

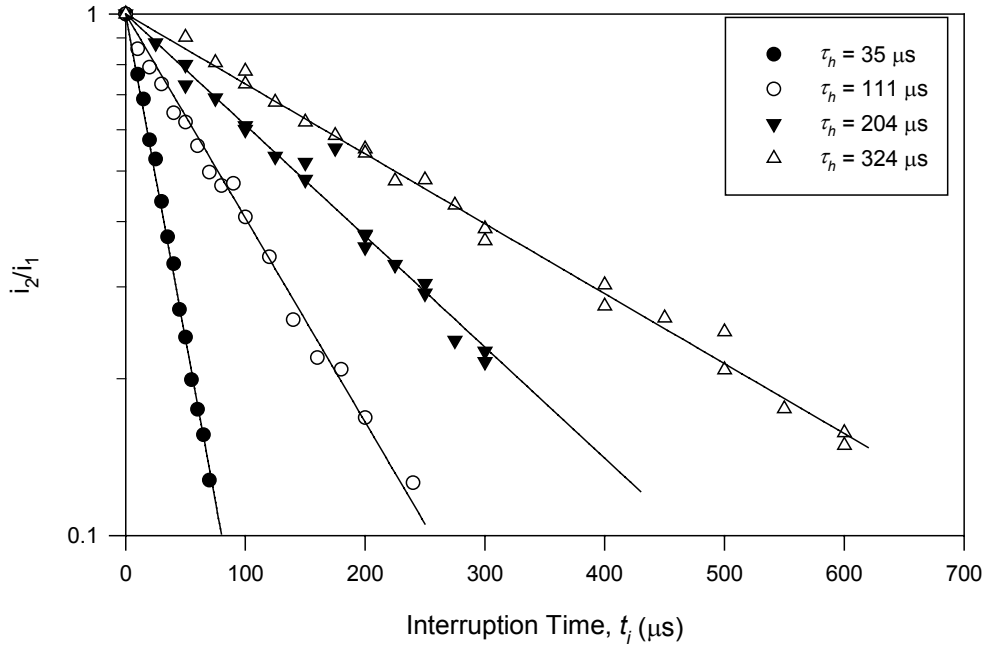

Figure 5.5: Semilogarithmic plots of i_2/i_1 vs. t_i for different samples with varying hole lifetimes. The exponential fit remains applicable for all hole lifetimes.

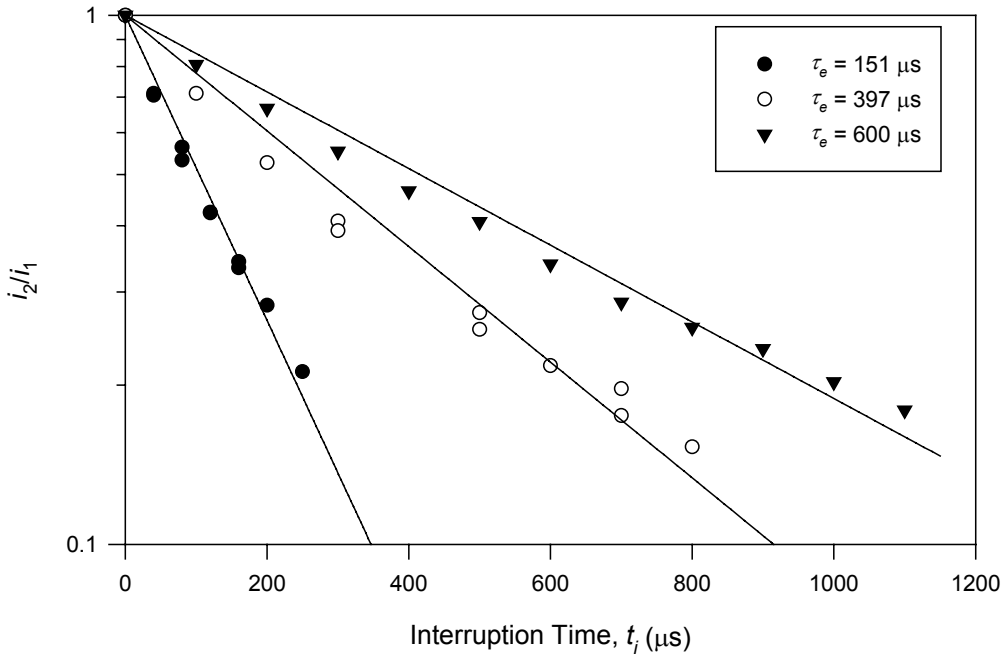

Figure 5.6: Semilogarithmic plots of i_2/i_1 vs. t_i for different samples with varying electron lifetimes. The exponential fit remains applicable for all electron lifetimes.

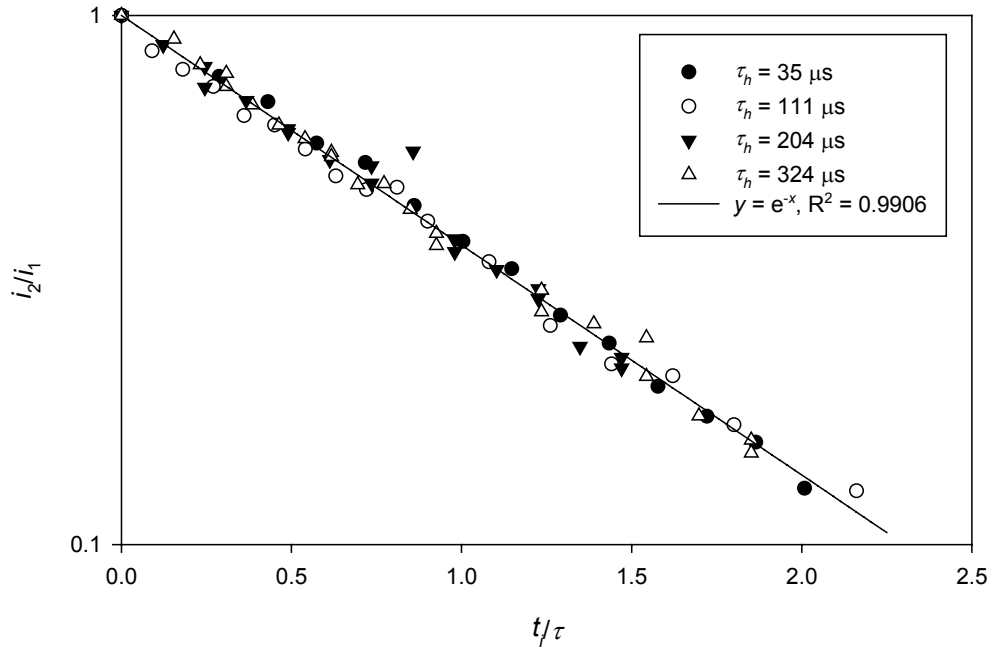

Figure 5.7: Semilogarithmic plot of i_2/i_1 vs. t_i/τ for holes. The high R^2 value indicates that the hole lifetime follows an exponential dependence.

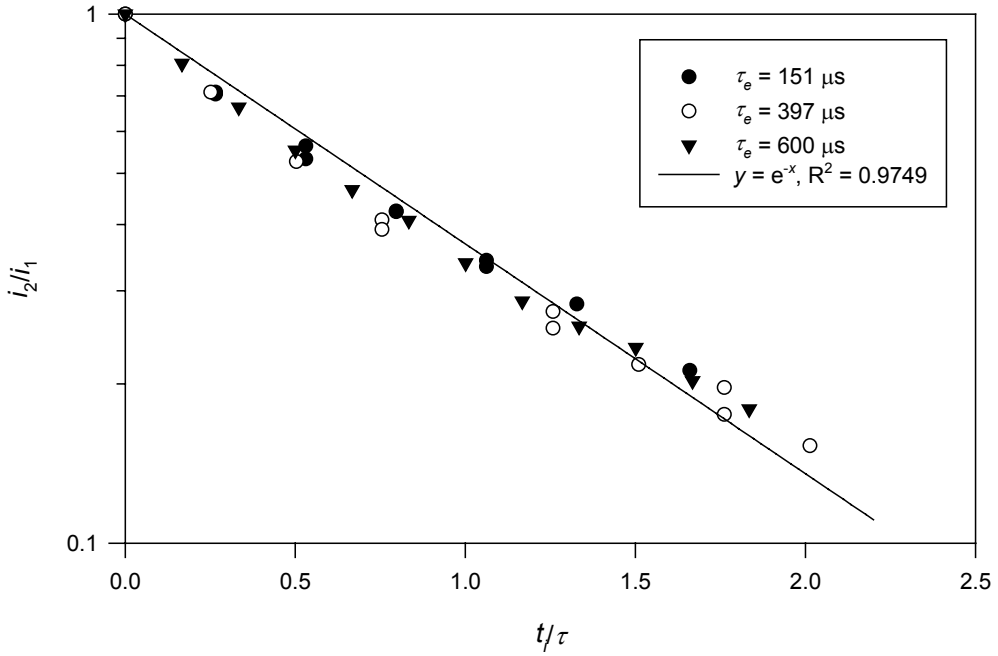

Figure 5.8: Semilogarithmic plot of i_2/i_1 vs. t_i/τ for electrons. The high R^2 value indicates that the electron lifetime follows an exponential dependence.

5.3 The Relaxation of the Carrier Transport Properties in a-Se

The a-Se used for x-ray detectors is a typical glass, and hence exhibits typical glass characteristics [46, 47], including the relaxation of electrical properties. From creation, the electrical properties, mobility and lifetime, change over time (relax) from a starting value until they reach a stable state. The mobility-lifetime product gives the carrier range, and thus the sensitivity of the photoconductor. Therefore, any device based on these photoconductors will perform very differently when it is first made compared to when it has reached steady state.

This section investigates the relaxation of the mobility and lifetime of both holes and electrons in a-Se alloys. The relaxation is observed for a particular alloy of a-Se, and compared to the relaxation of other a-Se alloys. The mobility and lifetime relaxations were fit to a stretched exponential, with a time constant, τ_{sr}, and stretching factor, β. The time constant, τ_{sr}, is especially important because it gives an indication of how much time is needed for the photoconductor to reach steady state.

5.3.1 Background

The fact that the carrier range relaxes over time has been observed before, but knowledge of the relaxation has been limited to observation of a change from an initial to a final state. Samples were merely left in the dark for a given amount of time until they reached steady state before attempting to determine their properties [10]. No detailed studies have been done to determine the nature of the relaxation process, or how varying the composition of the a-Se alloy affects the relaxation.

The TOF and IFTOF experiments have proved to be effective in determining the mobility and lifetime for various different alloys of a-Se [48]. The IFTOF technique can accurately measure both the mobility and lifetime in the sample at the time of the

measurement. Therefore, with repeated measurements of μ and τ as they change over time, the relaxation of the range of a given material can be observed.

The composition of the samples was varied in order to examine the effects of composition on the relaxation. The samples consisted of a-Se with 0 - 0.5% As added (to form stabilized a-Se) and one set of samples with ~5ppm Cl added. Source material for the samples was provided by ANRAD Corporation. The samples were deposited onto cleaned Corning glass substrates using conventional vapour deposition, as described in Chapter 4. Semitransparent gold contacts were added afterwards, as described in Chapter 4 as well.

5.3.2 Technique

Relaxation of a glass begins immediately after its formation. The properties of the glass will change over time from their initial properties and will eventually reach a steady state. This relaxation is the same immediately after the glass has been annealed above the glass transition temperature, T_g and subsequently cooled below T_g. When a sample is heated above T_g, the bonds within the sample gain energy and are free to move around. Once the sample is cooled below T_g, the atomic or molecular motions become "frozen", in a similar fashion as when the sample was first fabricated. This work involves monitoring the changes in the electrical properties as the "glass structure" in a-Se changes (that is relaxes) from state G towards A in Figure 5.9. This change in the structure should be the same whether the sample has just been fabricated, or whether it is annealed above T_g.

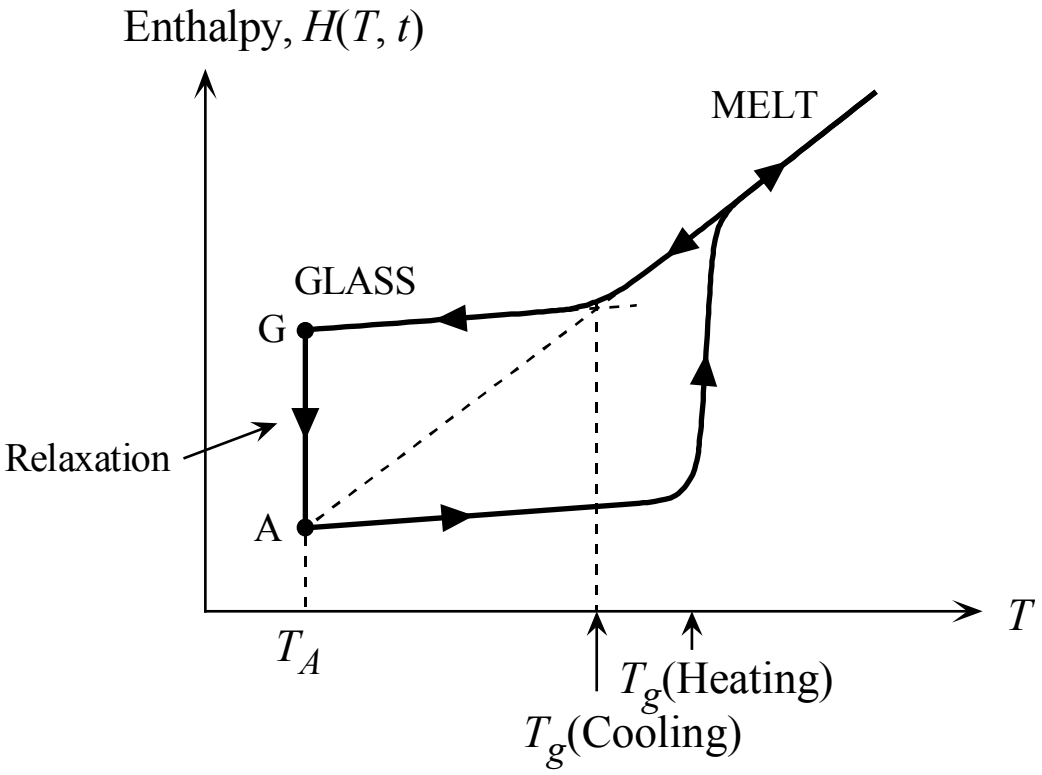

Figure 5.9: Enthalpy vs. temperature for a-Se. Once a sample is heated or fabricated above T_g and cooled to room temperature, it is at state G. From there it relaxes towards the equilibrium steady state at A. By heating the sample up from state A above T_g, the process can be repeated.

Since there are two possible starting points for the relaxation, right after deposition and after annealing, measurements were performed from both starting points. For an experiment from the fabrication point, immediately after the deposition, gold contacts were applied to the samples and measurements began. For an experiment from annealing, a rested sample was heated to 55 ºC and held there for 30 minutes. The sample was then cooled to room temperature and allowed to rest. Measurements began about one hour after the sample had begun cooling. For both starting points, the sample would relax towards steady state at room temperature.

In this investigation, TOF and IFTOF experiments were used to examine the relaxation of the mobility (μ) and lifetime (τ) of various alloys of a-Se as they relaxed. Each relaxation experiment consisted of several sets of mobility and lifetime measurements to track how they changed as the sample relaxed. For a single set of

measurements, one TOF experiment was performed to determine the mobility and 4 IFTOF measurements were performed to get an accurate idea of the lifetime. These measurement sets were repeated as time progressed, starting with a delay between measurements of about 1 hour, slowly increasing until only 2 sets of measurements were performed per day. Two measurements per day were performed until a two-day break on the 5th and 6th days after the sample was fabricated/annealed. One more set of measurements was performed 7 days after and 8 days after fabricated/annealing.

With the data from all these TOF and IFTOF measurements, it was informative to check the shape of the relaxation. The lifetime data was fit with a stretched exponential equation of the form:

$$\tau = \tau_{\infty} + (\tau_o - \tau_{\infty})\exp\left(-\left(t/\tau_{sr}\right)^{\beta}\right) \tag{5.2}$$

where τ_{∞} is the steady state lifetime, τ_o is the initial lifetime (immediately after fabrication or annealing), τ_{sr} is the relaxation time constant, and β is the stretching factor. It was already known that τ_{∞} and τ_o would vary with the composition of the a-Se [11], so this work concentrated more on observing how τ_{sr} and β would be affected by changing the sample composition. The mobility data was fit to a similar exponential, using μ in place of τ.

5.3.3 Results

The effects of relaxation on the resulting TOF and IFTOF waveforms were quite noticeable. The change in a typical TOF waveform for a sample of a-Se:0.2% As from the beginning of the experiment till the end is shown in Figure 5.10 for electrons and Figure 5.11 for holes. The waveform can be seen to be "improving" as time goes on, indicating the charge transport properties are improving as the sample relaxes.

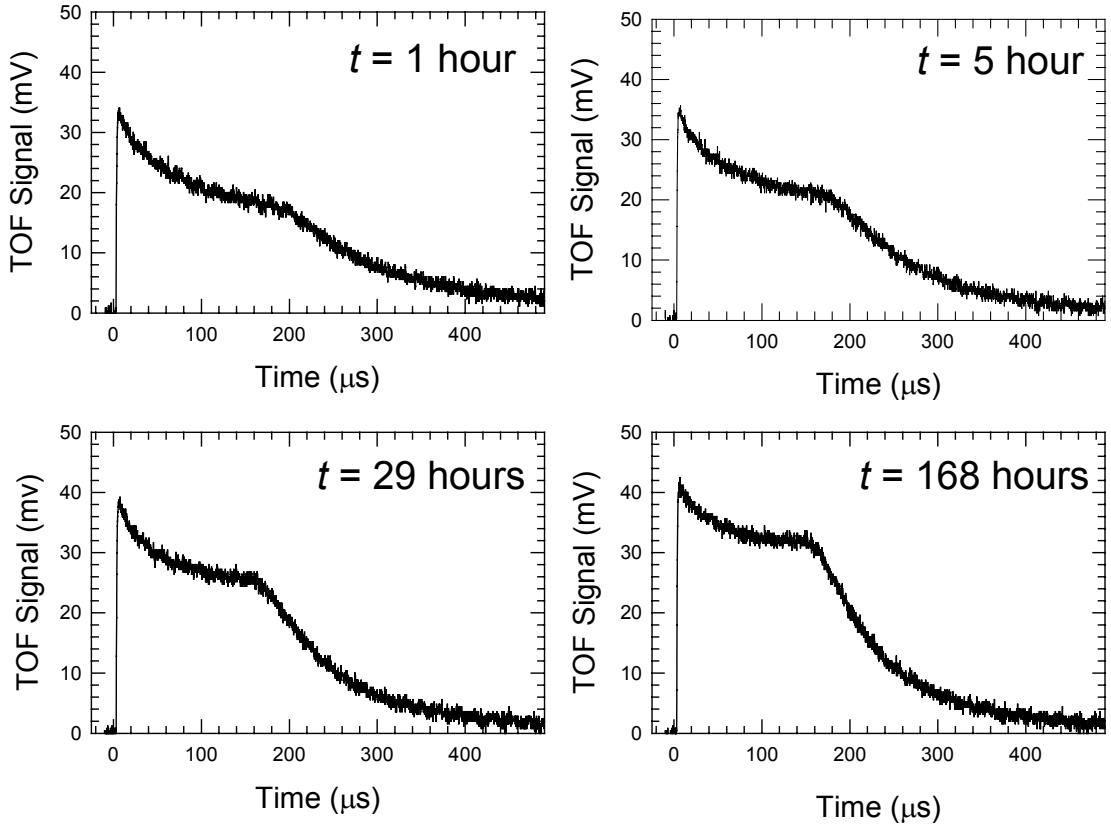

Figure 5.10: Change in the electron TOF waveform as the relaxation experiment progresses in a sample of a-Se:0.2% As.

Over the course of a measurement, the mobility improves. The progress of the improvement in mobility as time goes on for a sample of a-Se:0.3% As +5 ppm Cl is shown in Figure 5.12 (a) for electrons and in Figure 5.12 (b) for holes. This general improvement was fitted with the stretched exponential equation (equation 5.2). For the fit in Figure 5.12 (a), the electrons were determined to have $\mu_{e\infty} = 2.85 \times 10^{-3}$ cm^2/Vs, $\mu_{oe} = 2.25 \times 10^{-3}$ cm^2/Vs, $\tau_{sr} \approx 25$ hours, and $\beta \approx 0.65$. For holes, $\mu_{h\infty} = 0.126$ cm^2/Vs, $\mu_{oh} = 0.115$ cm^2/Vs, $\tau_{sr} \approx 35.0$ hours, and $\beta \approx 0.6$. Unfortunately, the R^2 values, indicating the quality of the fit, for the stretched exponential fit were only 0.8283 and 0.7475 for electrons and holes respectively.

The fits listed for Figure 5.12 are the "best" fits, however, there is a relatively large play on what can be considered a fit for the mobility relaxation. Figure 5.13 gives a comparison of how changing the fitting parameters change the quality of the fit for the

electron mobility. Even a very large swing of the fitting parameter τ_{sr} (from τ_{sr} = 20 – 30 hours) does not cause a very significant decrease in fitting quality, indicating that the "best" fit has significant error, τ_{sr} = 25 ± 5 hours. Similarly, β can be in the range 0.4-0.7 and still maintain high R^2 values.

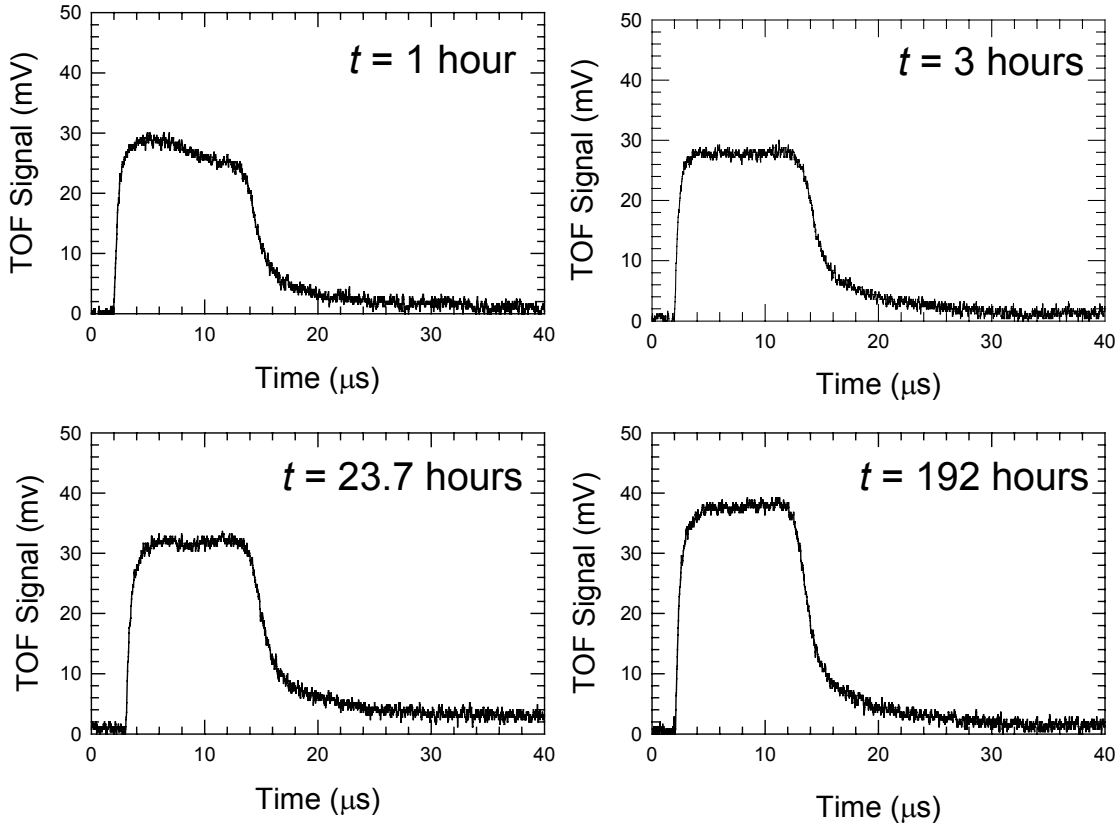

Figure 5.11: Change in the hole TOF waveform as the relaxation experiment progresses in a sample of a-Se:0.2% As.

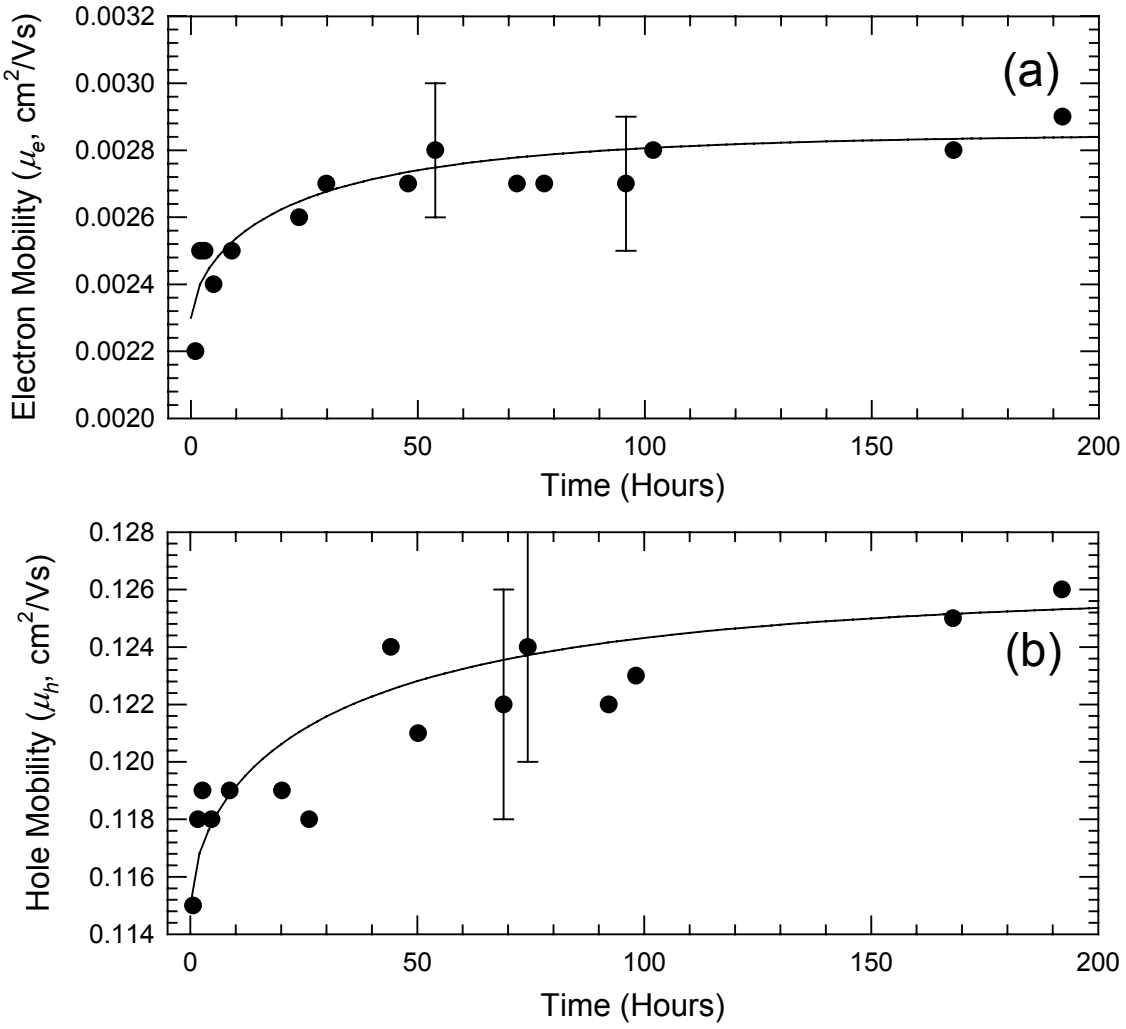

Figure 5.12: Relaxation of the mobility of electrons and holes in samples of a-Se:0.3% As + 5ppm Cl.

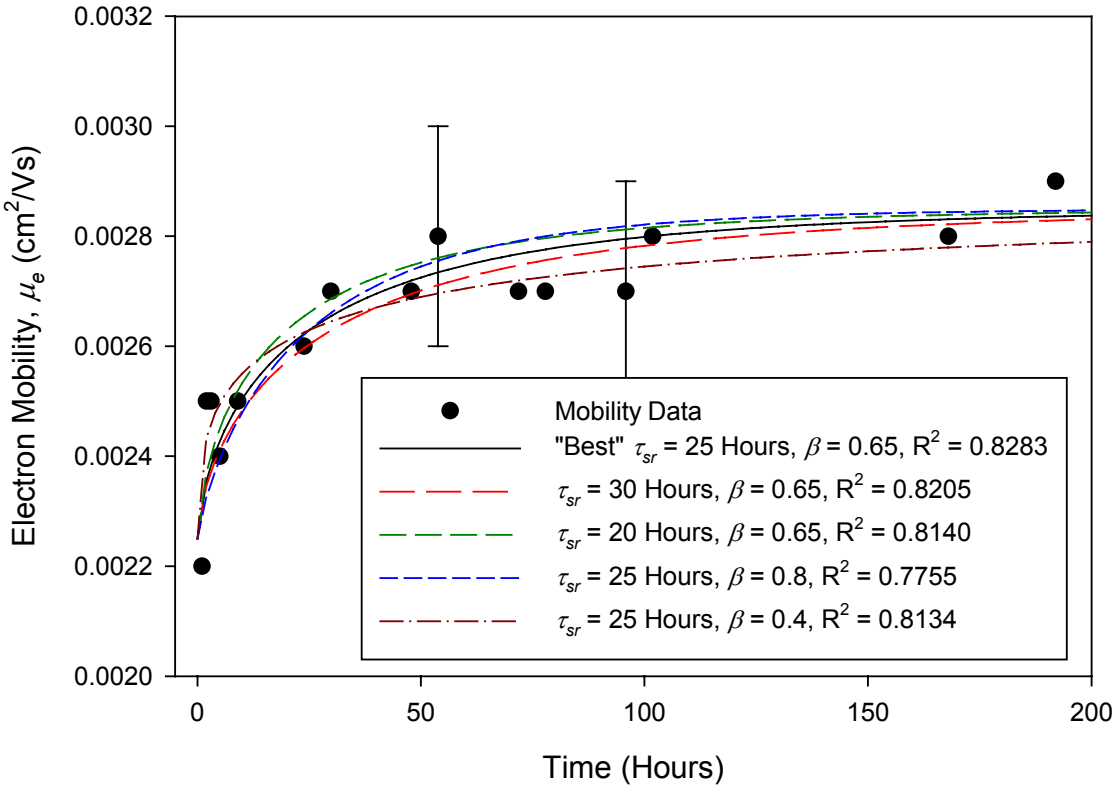

Figure 5.13: Comparison of different fitting parameters on the electron mobility fit.

Even though the relaxation of the mobility with a stretched exponential has a very large error range, the overall improvement in the mobility for both holes and electrons over the course of the relaxation is nonetheless informative to examine. In Figure 5.12, the electron mobility increased by 31.8%, while the hole mobility only increased by 9.57%. This indicates that the electron mobility is far more affected by the relaxation than the hole lifetime. A list of the increases in mobility for both electrons and holes, as well as the "best" values for τ_{sr} and β are shown in Table 5.1 for all materials used in this experiment. As seen in Table 5.1, the electron mobility increases about 20-40% while the hole mobility increases by < 10% for all compositions. Comparing all the values of the "best" τ_{sr} and β, it is interesting to note the repetition of the "best" values of τ_{sr} = 25 hours and β = 0.65. Furthermore, when the "best" values do not match, if the fit is forced to have τ_{sr} = 25 hours and β = 0.65, they maintain comparable fit quality. This seems to indicate that the mobility has a consistent method for relaxation that is independent of the

sample composition. If the mobility relaxation does follow the stretched exponential, then it seems likely that τ_{sr} = 20-30 hours and β = 0.4-0.7.

Table 5.1: Overall improvements in Mobility and "best" τ_{sr} and β for all samples used in this work

Material	Initial Mobility ($cm^2V^{-1}s^{-1}$)	Final Mobility ($cm^2V^{-1}s^{-1}$)	"Best" τ_{sr} (Hours)	"Best" β	% Change in Mobility
Holes, Pure a-Se (Annealing)	0.120	0.125	**5**	**0.6205**	**4.17**
Holes, a-Se+7ppm O (Annealing)	0.125	0.136	**25**	**0.65**	**8.80**
Holes, a-Se:0.2%As (Sample A, Annealing)	0.107	0.116	**21.84**	**0.6**	**8.41**
Holes, a-Se:0.3%As+5ppm Cl (Deposition)	0.115	0.126	**35**	**0.6**	**9.57**
Holes, a-Se:0.5%As (Annealing)	0.12	0.122	**N/A**	**N/A**	**1.67**
Electrons, Pure a-Se (Annealing)	3.4×10^{-3}	4.1×10^{-3}	**25**	**0.65**	**20.6**
Electrons, a-Se:0.2%As (Sample B, Annealing)	2.5×10^{-3}	3.3×10^{-3}	**25**	**0.65**	**32.0**
Electrons, a-Se:0.2%As (Sample B, Deposition)	2.8×10^{-3}	3.4×10^{-3}	**25**	**0.65**	**21.4**
Electrons, a-Se:0.2%As (Sample A, Annealing)	2.4×10^{-3}	3.0×10^{-3}	**25**	**0.65**	**25.0**
Electrons, a-Se:0.3%As+5ppm Cl (Annealing)	2.2×10^{-3}	2.9×10^{-3}	**25**	**0.65**	**31.8**
Electrons, a-Se:0.5%As (Annealing)	1.4×10^{-3}	2.0×10^{-3}	**25**	**0.65**	**42.9**

One possible explanation for the poor fit quality is that the thickness of the samples does change as they relax. Work by Tan [49] recently showed that thickness actually decreases by 3% as a sample ages. For the mobility calculations in this work, it was assumed that the thickness of the sample remained constant in order to simplify the measurements. To check if a decreasing thickness would improve the quality of the fit, a sample of a-Se:0.3% As + 5ppm Cl was used which had rested thickness, L_∞ = 120 μm. Since the thickness would have decreased 3% from the initial value, $L_o = L_\infty/0.97$ = 123.7 μm. It was assumed that the thickness would relax with a stretched exponential with τ_{sr} =

25 hours and $\beta = 0.65$, the "best" fit values for the original mobility relaxation. The new, changing thickness is shown in Figure 5.14. The mobility was then re-calculated using the new changing thickness, but keeping the transit time and applied voltage the same as before, and then re-fit with the stretched exponential. The new fit is shown in Figure 5.15. For this new fit, the electrons had $\mu_{e\infty} = 2.85 \times 10^{-3}$ cm^2/Vs, $\mu_{oe} = 2.36 \times 10^{-3}$ cm^2/Vs, $\tau_{sr} \approx 22$ hours, and $\beta \approx 0.5$ with $R^2 = 0.7919$. Surprisingly, using the adjusted thickness actually reduced the R^2 value, from $R^2 = 0.8283$. This decrease indicates that the changing thickness was not likely the largest source of error in the mobility relaxation fit.

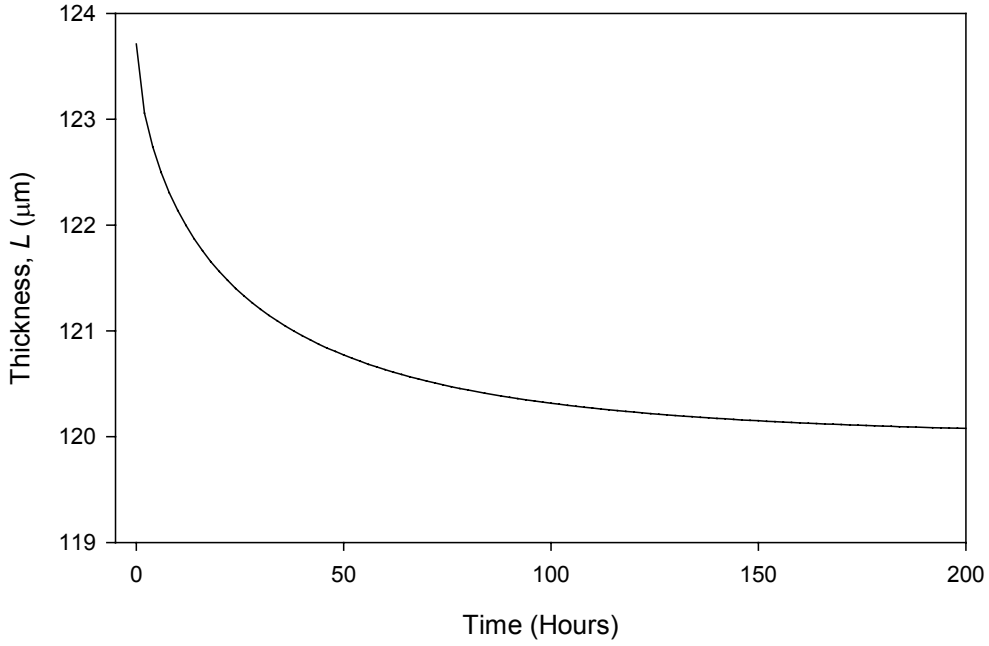

Figure 5.14: Adjusted sample thickness vs. time.

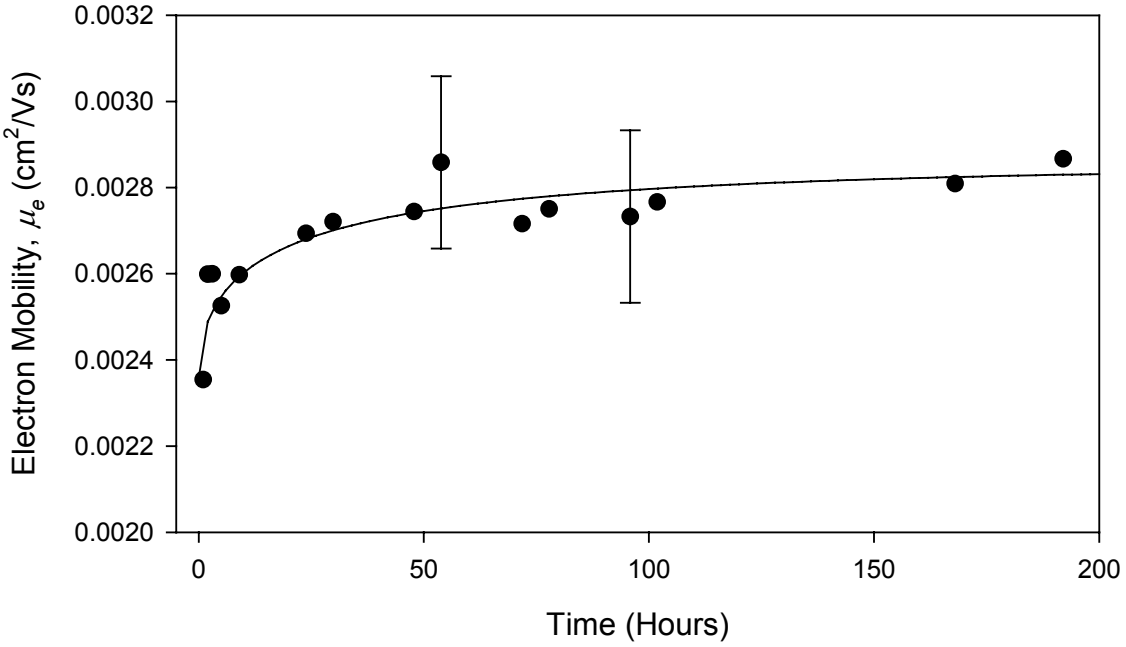

Figure 5.15: Electron mobility relaxation taking into account changing sample thickness.

The lifetime also improves over the course of the experiment. The relaxation of the lifetimes of electrons and holes in samples of a-Se:0.2% As are shown in Figure 5.16. The lifetime starts from an initial value and slowly relaxes to a steady state. The relaxation was found to fit to the stretched exponential function (Equation 1.2). For the electrons in Figure 5.16, $\tau_{e\infty}$ = 179 μs, τ_{eo} = 129 μs, $\tau_{sr} \approx$ 14.6 h, and $\beta \approx 0.6$; for the holes, $\tau_{h\infty}$ = 32.7 μs, τ_{ho} = 18.2 μs, $\tau_{sr} \approx$ 17.1 h, and $\beta \approx 0.7$. These fits had r-squared values of 0.9881 and 0.9761 for electrons and holes respectively. Therefore, the stretched exponential equation works quite well for modelling the lifetime.

The fit shown in Figure 5.16 is the "best fit", which can be achieved with a slight change in the structural relaxation constant, τ_{sr} and the stretching factor, β. For electrons, comparable quality of fit can be achieved with a range of values for τ_{sr}(=14.6-16.5 hours) and β (= 0.6-0.7). The values for the initial and final lifetime, in contrast, do not change more than a few percent for all the best fits. A comparison of the effect of changing τ_{sr} and β is shown in Figure 5.17, where it is apparent that τ_{sr} can be changed by ±2 hours without significantly altering the quality of the fit.

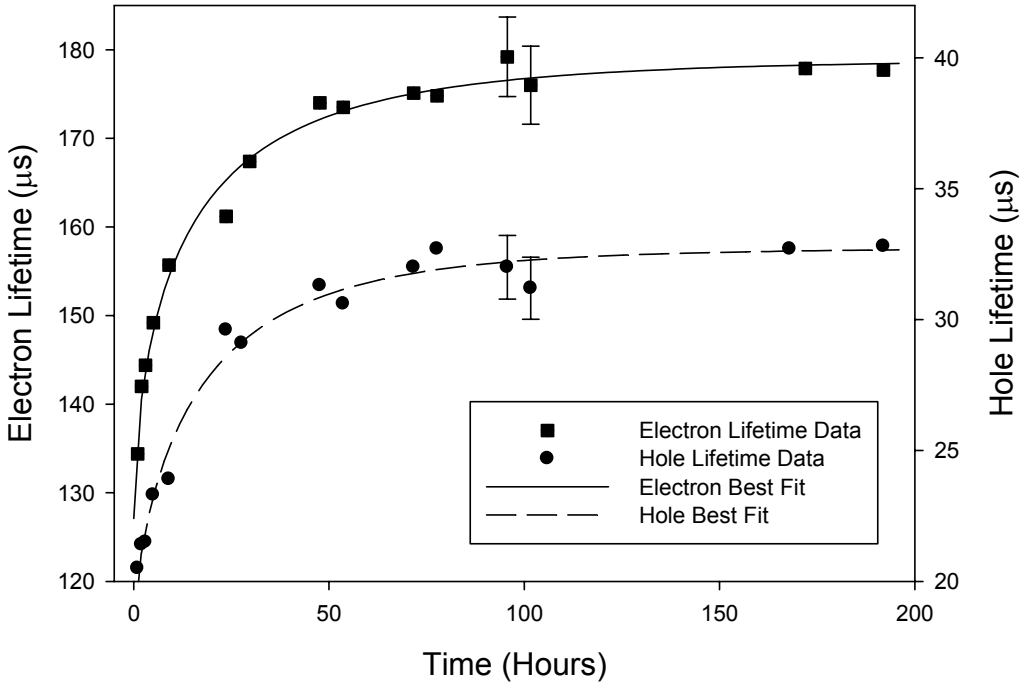

Figure 5.16: Relaxation of the lifetime of electrons and holes in samples of a-Se:0.2% As.

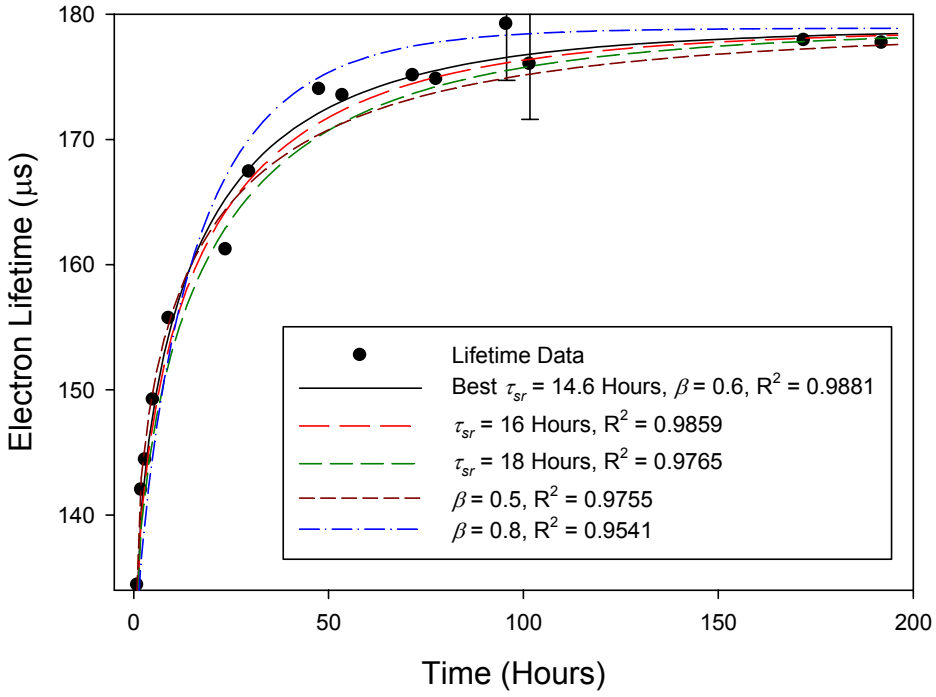

Figure 5.17: Comparison of different fitting parameters. Effects of changing τ_{sr} and β on the curve fits.

The relaxation of a particular sample is comparable whether the sample comes from annealing or deposition. The relaxation of the same sample of a-Se:0.2% As from deposition and annealing is shown in Figure 5.18. From deposition, the sample relaxed with a time constant, τ_{sr}, of 15.6 ± 2 h, while from annealing, the sample relaxed with a time constant of 14.6 ± 2 h. For both relaxations, the "best fit" value of β was 0.6. These values for τ_{sr} are well within the ± 2 h range that can apply to the "best fit" values. Thus, film deposition at a substrate temperature about T_g has a relaxation characteristic that is equivalent to annealing above T_g.

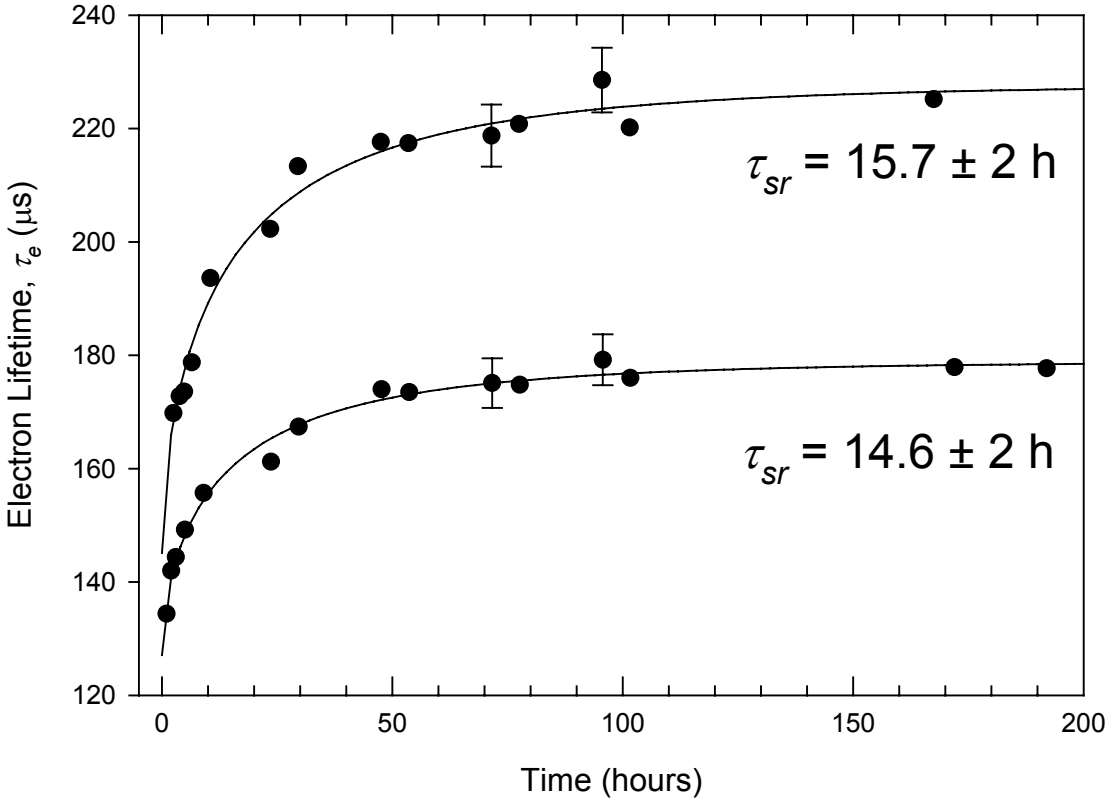

Figure 5.18: Relxation of the lifetime of electrons of a sample of a-Se:0.2% As from both depostition and annealing. τ_{sr} =15.7 h for the deposition measurements and τ_{sr} = 14.6 h for the annealing measurement.

The structural relaxation time for holes and electrons for a given sample composition are practically the same. For example, in Figure 5.16 for samples of a-Se:0.2% As, the electrons have a structural relaxation time, τ_{sr} = 14.6 ± 2 h and stretching factor β = 0.6 while the holes have τ_{sr} = 17.1 ± 2 h and β = 0.7. Similarly, in Figure 5.19

for samples of pure a-Se, electrons have a relaxation time $\tau_{sr} = 7.7 \pm 2$ h and $\beta = 0.6$ while the holes have $\tau_{sr} = 7.5 \pm 2$ h and $\beta = 0.7$. This indicates that the factors affecting the relaxation of the lifetimes of electrons and holes are quite similar.

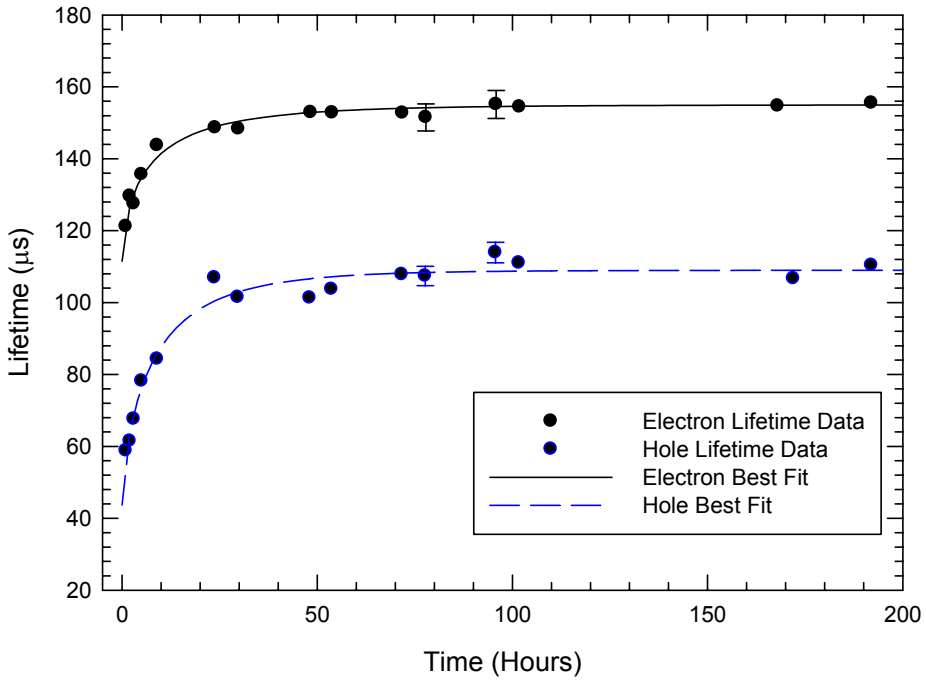

Figure 5.19: Relaxation of the lifetime of electrons and holes in samples of pure a-Se.

The relaxation of the lifetime for both electrons and holes varies with sample composition. Comparing the relaxation of pure a-Se shown in Figure 5.19 with the relaxation of a-Se:0.2% As in Figure 5.16, it is clear that the addition of As has caused the relaxation to slow down. The structural relaxation time for electrons increased from $\tau_{sr} = 7.7 \pm 2$ h in pure a-Se to $\tau_{sr} = 14.6 \pm 2$ h in a-Se:0.2% As. Similarly, the structural relaxation time for holes increased from $\tau_{sr} = 7.5 \pm 2$ h in pure a-Se to $\tau_{sr} = 17.1 \pm 2$ h in a-Se:0.2% As. On the other hand, the stretching factor, β, seems independent of sample composition. For both holes and electrons, the best fits for all relaxations consisted of $\beta = 0.6$-0.7; electrons tended towards $\beta = 0.6$ and holes tended towards $\beta = 0.7$.

The structural relaxation time for electron and hole lifetimes changes with sample composition. A plot of how τ_{sr} changes with sample composition is shown in Figure 5.20. As can be seen, τ_{sr} increases with increasing Arsenic content. Simply adding 0.2%

As to the pure a-Se almost doubles τ_{sr} to ~15 h from ~8h, and increasing the As content to 0.5% more than doubles τ_{sr} to ~38 h. This pattern was followed by both electrons and holes, retaining comparable τ_{sr} values for the various compositions.

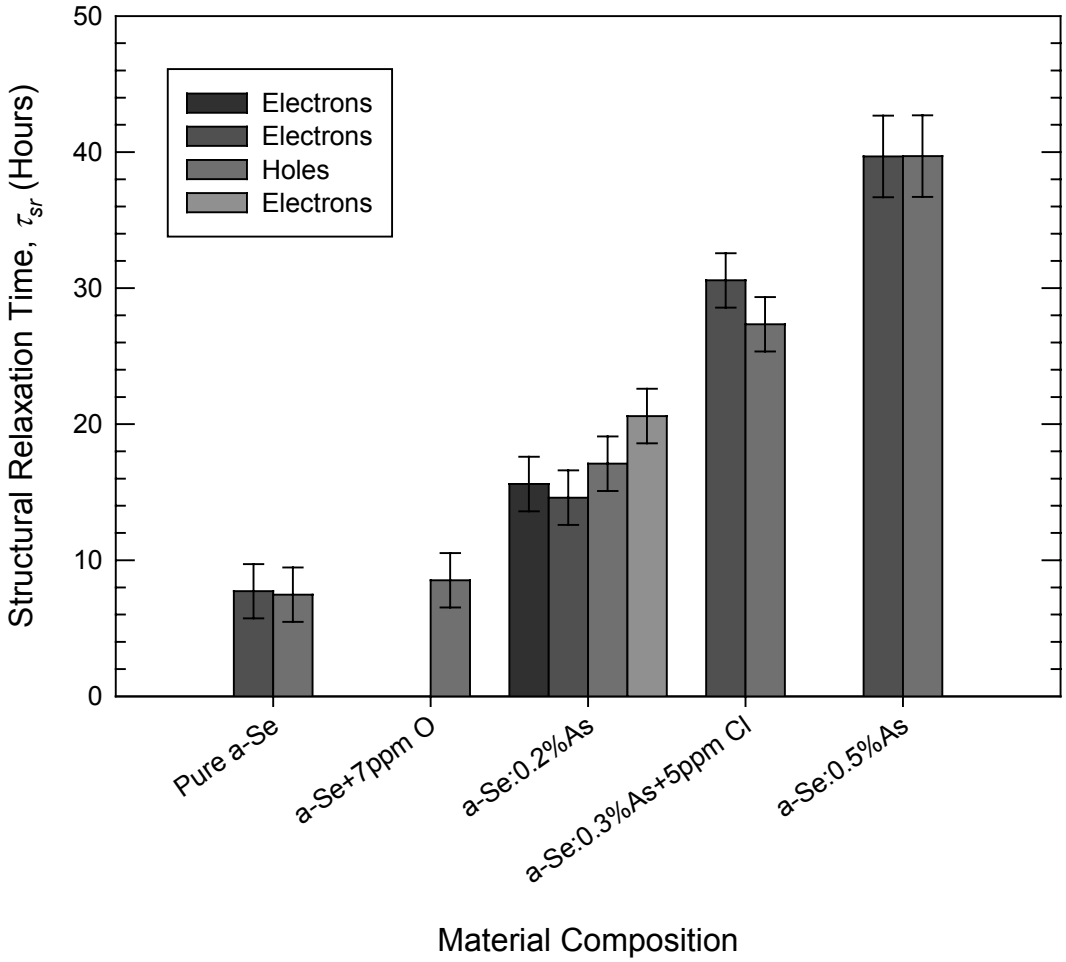

Figure 5.20: Structural relaxation time, τ_{sr}, for the lifetimes of the samples of various compositions measured in this work.

The magnitude of the lifetime also changes significantly from the beginning of the experiment to the end. Table 5.2 lists the initial and final lifetimes for all the samples measured in this work. For holes the overall change was an increase of 34.2 - 167%; for electrons the increase was 36-54.4%. This increase in lifetime is significantly higher than the increase in mobility, listed in Table 5.1. For holes, the mobility only increased by less than 10% in magnitude compared to an average change of 85% in the lifetime. Since the overall increase in lifetime is so much higher than the mobility, the relaxation of the

hole range, $\mu_h\tau_h$, is almost entirely dominated by the change in lifetime. Similarly for electrons, the mobility changed on average 29% compared to the lifetime increasing on average by 45%.

Table 5.2: Overall change in lifetime for all samples used in this work

Material	Initial Lifetime (μs)	Final Lifetime (μs)	% Change in Lifetime	Structural Relaxation Time (hours)
Holes, Pure a-Se (Annealing)	7.6	10.2	**34.2**	**7.5**
Holes, a-Se+7ppm O (Annealing)	40.9	109	**167**	**8.5**
Holes, a-Se:0.2%As (Sample A, Annealing)	18.2	32.7	**79.7**	**17.1**
Holes, a-Se:0.3%As+5ppm Cl (Deposition)	49.9	77.6	**55.5**	**27.3**
Holes, a-Se:0.5%As (Annealing)	12.7	23.8	**87.4**	**39.7**
Electrons, Pure a-Se (Annealing)	114	155	**36.0**	**7.7**
Electrons, a-Se:0.2%As (Sample B, Annealing)	129	179	**38.8**	**14.6**
Electrons, a-Se:0.2%As (Sample B, Deposition)	147	227	**54.4**	**15.6**
Electrons, a-Se:0.2%As (Sample A, Annealing)	363	559	**54.0**	**20.6**
Electrons, a-Se:0.3%As+5ppm Cl (Annealing)	238	342	**43.7**	**30.6**
Electrons, a-Se:0.5%As (Annealing)	262	378	**44.3**	**39.7**

This large change in range over the course of the relaxation can alter the performance of any device using these materials. Device tests performed immediately after the a-Se is deposited will perform worse than those allowed to rest a few days while the a-Se relaxes. Furthermore, if any detector is exposed to high temperatures above T_g, such as in transport in a container, it will need to rest to recover its proper performance. Ninety percent relaxation corresponds to a time $t_r = (2.303)^{1/\beta}\tau_{sr}$. For a-Se:0.2% As, with a $\tau_{sr} \approx 15$ h, and $\beta \approx 0.6$, $t_r \approx 60$ h or 2.5 days, a significant time to wait. It is therefore informative to determine the exact change in sensitivity of a detector using a-Se as a photoconductor. The following formula, which is described in more detail in the

appendix, was used to calculate the sensitivity of a detector using the materials studied in this work.

$$S = \frac{5.45\times10^{13}\times e}{(\alpha_{\text{air}}/\rho_{\text{air}})W_{\pm}}\left(\frac{\alpha_{\text{en}}}{\alpha}\right)\times\left\{x_e\left[\left(1-e^{-1/\Delta}\right)+\frac{1}{\Delta/x_e-1}\left(e^{-1/x_e}-e^{-1/\Delta}\right)\right]\right.$$
$$\left. + x_h\left[\left(1-e^{-1/\Delta}\right)-\frac{1}{\Delta/x_h+1}\left(1-e^{-1/\Delta-1/x_h}\right)\right]\right\} \quad (5.3)$$

where S is the sensitivity in C cm^{-2} R^{-1}, e is the elementary charge, α_{air} and ρ_{air} are the energy absorption coefficient and the density of the air respectively, $W_{\pm}$ is the EHP creation energy, α_{en} and α are the energy absorption coefficient and the linear attenuation coefficient of the photoconductor respectively, Δ is the normalized attenuation depth, $\Delta=1/(\alpha L)$, and $x_e = \mu_e\tau_e F$ and $x_h = \mu_h\tau_h F$ represent the electron and hole schubwegs per unit thickness respectively.

Using the above formula, as well as the data from Table 5.1 and Table 5.2 for samples that had both holes and electrons relaxing, the change in sensitivity over the course of a relaxation could be calculated. For a first calculation, typical values for operating a detector for mammography were used; thickness was taken to be L = 200 μm, incident x-ray energy was E_{ph} = 20 keV, and operating bias was 10 V/μm. The results from the calculations are shown in Table 5.3. Under positive bias, the sensitivity only increases 1-3%, which would not be particularly significant to device operation unless the detector had very stringent requirements. Under negative bias, the sensitivity increases by 4-9%, which could have a noticeable impact on detector performance.

The calculation was repeated using typical values for operating a detector for general radiography; thickness was taken to be L = 1000 μm, incident x-ray energy was E_{ph} = 50 keV, and operating bias was 10 V/μm. The results from the calculations are shown in Table 5.4. Under positive bias, the sensitivity increases 8-17%, which would definitely have an effect on detector performance. Similarly, under negative bias, the sensitivity increases by 14-26%, which would also have a noticeable impact on detector performance. From these calculations, it is clear that the sensitivity of a detector being

used for general radiography is affected by the relaxation far more than the sensitivity of a detector being used for mammography.

Table 5.3: Change in sensitivity of a detector for mammography using a-Se over the course of the relaxation

Material	Initial Sensitivity (Positive Bias, pC cm^{-2} mR^{-1})	Final Sensitivity (Positive Bias, pC cm^{-2} mR^{-1})	% Change (+ve Bias)	Initial Sensitivity (Negative Bias, pC cm^{-2} mR^{-1})	Final Sensitivity (Negative Bias, pC cm^{-2} mR^{-1})	% Change (-ve Bias)
a-Se:0.2%As (Sample A, Annealing)	204.457	208.794	**2.12**	197.845	205.131	**3.68**
a-Se:0.3%As +5ppm Cl (Deposition)	207.484	210.111	**1.27**	189.816	200.348	**5.55**
a-Se:0.5%As (Annealing)	199.825	206.314	**3.25**	180.203	196.117	**8.83**

Table 5.4: Change in sensitivity of a detector for general radiography using a-Se over the course of the relaxation

Material	Initial Sensitivity (Positive Bias, pC cm^{-2} mR^{-1})	Final Sensitivity (Positive Bias, pC cm^{-2} mR^{-1})	% Change (+ve Bias)	Initial Sensitivity (Negative Bias, pC cm^{-2} mR^{-1})	Final Sensitivity (Negative Bias, pC cm^{-2} mR^{-1})	% Change (-ve Bias)
a-Se:0.2%As (Sample A, Annealing)	2225.45	2470.49	**11.0**	2078.55	2373.17	**14.2**
a-Se:0.3%As +5ppm Cl (Deposition)	2296.31	2482.28	**8.10**	1925.56	2234.95	**16.1**
a-Se:0.5%As (Annealing)	1945.82	2284.89	**17.4**	1631.06	2056.79	**26.1**

It is also informative to see the effects of the relaxation on the total trap concentration. In Chapter 3, an expression (equation 3.45) was developed that related the total trap concentration to the product $\mu\tau$:

$$\mu\tau = \mu_o \tau_{c2} = \frac{\mu_o}{\sigma u N_T}$$

where μ is the drift mobility of the carrier, τ is the lifetime of the carrier, μ_o is the conduction mobility, σ is the capture cross section, u is the mean speed of the carriers, and N_T is the total trap concentration.

Using this expression, and taking u as the thermal velocity $u = 10^7$ m/s, σ as the capture-cross section using a capture radius of 3Å from [50], μ_o for holes as $\mu_o = 0.34$ cm^2/Vs, μ_o for electrons as $\mu_o = 0.1$ cm^2/Vs, and the $\mu\tau$ data from Table 5.1 and Table 5.2. The results are shown in Table 5.5. For both electrons and holes, there seems to be typically a 40-50% drop in the total trap concentration from the start of the relaxation to when the sample has reached steady state. This implies that the electron and hole trap concentrations are affected by the same factors during the relaxation.

Table 5.5: Change in the total trap concentration in a-Se over the course of the relaxation.

Material	**Initial trap concentration ($\times 10^{10}$ cm^{-3})**	**Final trap concentration ($\times 10^{10}$ cm^{-3})**	**% Drop**
Holes, Pure a-Se (Annealing)	13.185	9.431	**28**
Holes, a-Se+7ppm O (Annealing)	2.352	0.811	**66**
Holes, a-Se:0.2%As (Sample A, Annealing)	6.175	3.170	**49**
Holes, a-Se:0.3%As+5ppm Cl (Deposition)	2.096	1.230	**41**
Holes, a-Se:0.5%As (Annealing)	7.890	4.141	**48**
Electrons, Pure a-Se (Annealing)	9.125	5.565	**39**
Electrons, a-Se:0.2%As (Sample B, Annealing)	10.967	5.987	**45**

Electrons, a-Se:0.2%As (Sample B, Deposition)	8.593	4.583	**47**
Electrons, a-Se:0.2%As (Sample A, Annealing)	4.060	2.109	**48**
Electrons, a-Se:0.3%As+5ppm Cl (Annealing)	6.755	3.566	**47**
Electrons, a-Se:0.5%As (Annealing)	9.642	4.678	**51**

5.4 Summary

This chapter presented the results of the all the experiments performed throughout this project. The TOF and IFTOF measurement techniques were successfully used to determine the mobility and lifetime for both electrons and holes in different alloys of a-Se. These measurements were used to study the relaxation of the carrier range in a-Se alloys. The relaxation of the carrier range can cause changes in the performance of a photodetector using a-Se. The relaxation was examined both from immediately after deposition, as well as annealing above T_g. It was found that relaxation from either starting point yielded similar results.

It was found that both the drift mobility and lifetime increased as they relaxed. The electron and hole mobility did not have very good fit quality to the stretched exponential, but there still appeared to be a pattern in which, regardless of material composition, the stretched exponential had a $\tau_{sr} \approx 25$ hours and $\beta = 0.4\text{-}0.7$. It was found that the mobility for electrons increased more than the mobility for holes; electron mobility increased by about 20-40% while the hole mobility increased by less than 10% for all compositions. Both electron and hole lifetimes were found to relax on a stretched exponential with a similar structural relaxation time, τ_{sr}, for a given composition. The stretching factor, β, was found to be constant at 0.6-0.7 for all a-Se compositions. The structural relaxation time τ_{sr} was also found to increase as the material composition increased in complexity, indicating that more complex a-Se alloys will require more time for their properties to reach steady state. For both electrons and holes, the overall increase in lifetime was greater than the overall increase in mobility. For electrons, the

lifetime increased on average by 45%, while in holes, the lifetime increased on average by 85%.

The effect of the relaxation on the sensitivity of a detector was also examined. It was found that for a typical detector to be used for mammography operating with a positive bias, the increase in sensitivity was only 1-3%, significant only for a detector under very stringent of requirements. On the other hand, under negative bias, the increase in sensitivity was 4-9%, which could very easily cause a noticeable effect on detector performance. In contrast, for a typical detector to be used for general radiology, under positive bias the sensitivity increased by 8-17%, and under negative bias the sensitivity increased by 14-26%. Both increases are significantly more than for a mammographic detector, and would definitely have an effect on detector performance. The effect of the relaxation on the total trap concentration was observed. For both electrons and holes, there was typically a 40-50% decrease in the total trap concentration as the sample relaxed. This indicates that the concentration of traps for both electrons and holes are controlled by similar factors during the relaxation.

6. Summary and Conclusions

Radiography is an important medical imaging tool used for medical diagnosis. Unfortunately, most of the x-ray imaging today is still based on the tried-and-true analog photographic film and phosphor screen. Recently though, both direct- and indirect-conversion digital detectors have been developed for radiographic imaging. This work was based on direct conversion detectors, which have the highest resolution. These digital detectors use an x-ray sensitive photoconductor, such as a-Se, to directly convert incident x-rays into electronic signals, eliminating the need for both the photographic film and phosphor screen. The photoconductor material is coated on top of an active-matrix-array (AMA) of thin film transistors (TFTs) to read out the electrical charges to produce a digital image. These digital detectors have self-scanning capability, so the x-ray image can be immediately viewed. a-Se and its alloys are an excellent choice for use as the x-ray photoconductor on these AMAs due to their ability to be readily deposited onto the AMA without damaging the circuitry, good x-ray sensitivity, good charge transport properties, and relatively low dark current.

An experimental apparatus capable of performing time-of-flight (TOF) and interrupted-field time-of-flight measurements (IFTOF) was developed and built. The TOF and IFTOF techniques can readily measure the drift mobility (μ) and trapping time, i.e. the lifetime, (τ) in a-Se samples; both are important properties because their product, $\mu\tau$, is directly related to the sensitivity of a-Se as a photoconductor. The TOF technique has been well established over the years as an effective method of measuring the mobility in a-Se and its alloys. The IFTOF technique, though able to accurately determine the lifetime in amorphous semiconductor samples, is less widely used due to implementation difficulties associated with switching large bias voltages (<1kV).

An apparatus for performing both TOF and IFTOF measurements was successfully designed and built. The use of a grounded bridge network, containing

balanced resistors and a capacitor to match the sample capacitance, as well as several high-speed diodes, eliminated the large displacement currents associated with switching high voltages. A high-speed differential amplifier was used to extract and amplify the transient photocurrent signal to be measured. The results of these measurements were used to attain a better understanding of the relaxation of the electrical properties of a-Se and its alloys.

The project has clearly shown that there are important changes in the electrical properties of a-Se photoconductors over several days from the instant at which the photoconductor was deposited. These changes are due to structural relaxation effects that occur in all glasses. In the case of a-Se, the relaxation effects occur over a few days whereas for many other glasses the effects can take years.

It is important to emphasise that the observed relaxation effects in the electrical properties directly affect the sensitivity of the detector. Thus, the timing of quality control experiments is critical because tests on a recently fabricated detector would yield inferior results than those taken a few days later when the a-Se structure has relaxed.

6.1 Relaxation of the Electrical Properties of a-Se

TOF and IFTOF measurements were used to examine the relaxation of the electrical properties of a-Se and its alloys. Since a-Se is a typical glass, it has typical glass relaxation characteristics, including the relaxation of its electrical properties. Of particular interest was how the drift mobility (μ) and lifetime (τ) relaxed, since these two properties are directly related to the schubweg of the charge carriers in the photoconductor, and hence the sensitivity of a photodetector using these materials. A methodology was developed to observe the relaxation of μ and τ as they relaxed over time from sample fabrication and from immediately after annealing. The relaxation was also observed for various different alloys of a-Se to observe the effects of material composition on the relaxation process.

The mobility, μ was found to relax only slightly, but did not have a particularly good fit quality when we attempted to fit to a stretched exponential. There was, however, a tendency in the data in that the stretched exponential tended to have a structural relaxation time $\tau_{sr} \approx 25 \pm 5$ hours as well as $\beta = 0.4 - 0.7$ consistently, regardless of sample composition. Given the poor fit quality, it is unclear whether the relaxation actually follows a stretched exponential or another function. While the exact shape of the mobility relaxation function was unclear, the increase in magnitude for both electrons and holes was worth noting. The increase in the mobility for electrons was significantly more than the increase in mobility for holes in all sample compositions measured. For electrons, the mobility increased by 20-40%, whereas for holes, the mobility only increased by less than 10%.

The relaxation of the lifetime (τ), on the other hand, fit to a stretched exponential reasonably well. Furthermore, the overall increase in lifetime as it relaxed was greater than the increase in the mobility. The average increase in lifetime was 85% for holes and 45% for electrons. The lifetime relaxation was fit to a stretched exponential of the form $\tau_e = \tau_{e\infty} + (\tau_{eo} - \tau_{e\infty})\exp\left[-(t/\tau_{sr})^{\beta}\right]$, where $\tau_{e\infty}$ is the electron lifetime when the sample is fully relaxed, τ_{eo} is the initial electron lifetime, τ_{sr} is the structural relaxation time, and β is the stretching factor. For a given a-Se alloy, the structural relaxation time, τ_{sr}, seemed to be constant for both electron and hole lifetime relaxations. Additionally, τ_{sr} was approximately the same for alloys relaxing from both immediately after sample deposition, and annealing above T_g, indicating that the relaxation is readily repeatable. Similarly, the stretching factor, β, maintained a value between 0.6 and 0.7 for both electron and hole relaxations, and for relaxations from deposition from annealing and deposition.

The relaxation was observed to depend on the a-Se composition. While the magnitude of the relaxation changed from alloy to alloy, its functional form remained as a stretched exponential. The stretching factor, β, for the lifetime remained 0.6-0.7 for all a-Se alloys used in this work. However, the structural relaxation time, τ_{sr}, changed

dramatically depending on the composition of a-Se. τ_{sr} increased with increasing As content, from ~7.5 hours for pure a-Se to ~40 hours for a-Se:0.5% As. τ_{sr} was found to be the same for both electron and hole relaxations for a given composition. Thus the relaxation in both the electron and hole lifetime seems to be controlled by the same structural relaxation process, that is, the electron and hole traps are structural in origin.

The structural relaxation time, τ_{sr}, for a given a-Se alloy is significant to detector performance. Detectors with higher As content will take far longer to reach nominal sensitivity than pure a-Se. Recovery of 90% of the final carrier lifetime takes $(2.303)^{1/\beta}\tau_{sr}$, thus a typical sample of a-Se:0.2% As will take about 2.5 days to reach 90% of its "steady state" value, while a sample of a-Se:0.5% As will take 6.7 days to reach 90%. However, if a mammographic detector with thickness L = 200 μm is operated under positive bias, the sensitivity only increases 1-3% over the course of the relaxation, only significant to detectors needing a high level of precision. On the other hand, under negative bias, the sensitivity increases 4-9%, which could have a noticeable effect on detector performance. The change in sensitivity for a detector to be used for general radiography, on the other hand, is affected by the relaxation far more. Under positive bias the sensitivity increased by 8-17%, and under negative bias the sensitivity increased by 14-26%. These increases would have a significant effect on the performance of any detector for generally radiography. The effect of the relaxation on the total trap concentration was observed. It was found that regardless of composition, both electrons and holes had a 40-50% drop in total trap concentration over the course of the relaxation, indicating that the concentration of traps is likely controlled by similar factors during the relaxation.

6.2 Suggestions for Future Work

Since there has been no examination of the relaxation of the electrical properties of a-Se done before, there are several areas that can use further examination. In this work, it was shown that τ_{sr} changes with changing sample composition. However, with a

larger variety in the sample compositions, a mathematical expression could potentially be developed to find τ_{sr} based on the composition of the sample without having to directly measure it. This would be especially helpful to manufacturers who are without the means to directly measure these properties.

In this work, the samples were limited to two different temperatures for the most part: above T_g for annealing and deposition, and room temperature (approximately 23 ºC) for all the measurements of the relaxation process. Thus, the most important extension of this work would be to see exactly how temperature could affect the relaxation of an a-Se alloy. It would be informative to see how the relaxation changes when a sample relaxes to a temperature other than room temperature. The relaxation could then be examined to see what effect, if any, temperature has on the relaxation process.

More work on the relaxation of the mobility could also be performed. The mobility was found to relax, and potentially on a stretched exponential, but the fit quality was too low to reach a definite conclusion. Further experimentation could be done to get a more accurate measurment of how the mobility of the carriers relaxes. More data points could be used along the relaxation curve to improve the fit quality. Furthermore, it is know that the thickness of the samples change as they relax. Monitoring how the thickness changes could enable slightly more accurate measurement of the mobility at a given time.

7. References

[1] Rowlands J.A. and Kasap, S.O., "Amorphous Semiconductors Usher in Digital X-ray Imaging", Physics Today, **50**, 1997, pp. 24-30.

[2] Selzer, R.H., "The use of computers to improve biomedical image quality", Fall Joint Computer Conference, 1968, pp. 817-834.

[3] Guler N. F. and Ubeyli E. D., "Theory and application of telemedicine", Journal of Medical Systems, **26**, 2002, pp. 199-220.

[4] Kasap S.O. and Rowlands J.A., "Direct-conversion flat-panel x-ray image sensors for digital radiography", Proceedings of the IEEE, **90**, 2002, pp. 591-604.

[5] Zhao W. and Rowlands J. A., "X-ray imaging using amorphous selenium: feasibility of a flat panel self-scanned detector for digital radiology", Medical Physics, **22**, 1995, pp. 1595-1604.

[6] Kasap S.O. and Rowlands J.A., "Direct-conversion flat-panel x-ray image detectors", IEEE Proceedings: Circuits, Devices, and Systems, **149**, 2002, pp. 85-96.

[7] Kasap S.O. and Rowlands J.A., "Review: X-ray photoconductors and stabilized a-Se for direct conversion digital flat-panel x-ray image detectors", Journal of Materials Science: Materials in Electronics, **11**, 2000, pp. 179-198.

[8] Kasap S.O., "X-ray sensitivity of photoconductors: application to stabilized a-Se", Journal of Physics D: Applied Physics, **33**, 2000, pp. 2853-2865.

[9] Que W. and Rowlands J.A., "X-ray photogeneration in amorphous selenium: geminate versus columnar recombination", Physical Review B, **51**, 1995, pp. 10500-10507.

[10] Kasap S.O. "Photoreceptors: The Chalcogenides", Chapter 9 in *The Handbook of Imaging Materials: Second Edition*, *Revised and Expanded*, edited by A.S. Diamond and D.S. Weiss, Marcel Dekker Inc., New York, 2002, pp. 329-368.

[11] Fogal, B., *Electronic Transport Properties of Stabilized Amorphous Selenium X-Ray Photoconductors*, M.Sc. Thesis, University of Saskatchewan, Saskatoon, Canada, 2005.

[12] Mott N.F., "Electrons in disordered structures", Advances in Physics, **16**, 1967, pp. 49-57.

[13] Cohen M.H., Fritzsche H. and Ovshinski S.R., "Simple band model for amorphous semiconductor alloys", Physical Review Letters, **22**, 1969, pp. 1065-1068.

[14] Marshall J.M. and Owen A.E., "Drift mobility studies in vitreous arsenic triselenide", Philosophical Magazine, **24**, 1971, pp. 1281-1290.

[15] Mott N.F. and Davis E.A., *Electronic processes in non-crystalline materials*, Clarendon Press, Oxford, 1979.

[16] Lucovsky G. and Galeener F.L., "Intermediate range order in amorphous solids", Journal of Non-Crystalline Solids, **35-36**, 1980, pp. 1209-1214.

[17] Robertson J. "Electronic structure of amorphous semiconductors", Advances in Physics, **32**, 1983, pp. 361-452.

[18] Adler D. and Yoffa E.J., "Localized electronic states in amorphous semiconductors", Canadian Journal of Chemistry, **55**, 1977, pp. 1920-1929.

[19] Abkowitz M., "On the question of chain-end ESR in amorphous selenium", Journal of Chemical Physics, **46**, 1967, pp. 4537-4538.
[20] Agarwal S.C., "Nature of localized states in amorphous semiconductors- a study by electron spin resonance", Physical Review B, **7**, 1973, pp. 685-691.
[21] Abkowitz M., "Density of states in a-Se from combined analysis of xerographic potentials and transient transport data", Philosophical Magazine Letters, **58**, 1988, pp. 53-77.
[22] Spear W.E., "Transit time measurements of charge carriers in amorphous selenium films", Proceedings from the Physical Society of London, **B70**, 1957, pp. 669-675.
[23] Rudenko A.I. and Arkhipov V.I., "Drift and diffusion in materials with traps. I. Quasi-equilibrium transport regime", Philosophical Magazine B, **45**, 1982, pp. 177-187.
[24] Hartke J.L. and Regensburger P.J., "Electronic states in vitreous selenium", Physical Review, **139**, 1965, pp. A970-A980.
[25] Davis E.A., "Optical absorption, transport and photoconductivity in amorphous selenium", Journal of Non-Crystalline Solids, **4**, 1970, pp. 107-116.
[26] Pai D.M. and Enck R.C., "Onsager mechanism of photogeneration in amorphous selenium", Physical Review B, **11**, 1975, pp. 5163-5174.
[27] Spear W.E., "Drift mobility techniques for the study of electrical transport properties in insulating solids", Journal of Non-Crystalline Solids, **1**, 1969, pp. 197-214.
[28] Polischuk B., *Interrupted Field Time-of-Flight Transient Photoconductivity Technique and its Applications to Amorphous Semiconductors*, Ph. D. Thesis, University of Saskatchewan, Saskatoon, Canada, 1994.
[29] Papadakis A.C., "Theory of transient space-charge perturbed currents in insulators", Journal of Physics and Chemistry of Solids, **28**, 1967, pp. 641-647.
[30] Kasap, S.O., *Optoelectronics and Photonics: Principles and Practices*, Prentice Hall, Upper Saddle River, New Jersey, 2001.
[31] Zanio K.R., Akutagawa W.M., and Kikuchi R., "Transient currents in semi-insulating CdTe characteristic of deep traps", Journal of Applied Physics, **39**, 1968, pp. 2818-2828.
[32] Akutagawa W. and Zanio K., "The possibilities of using CdTe as a gamma spectrometer", IEEE Transactions on Nuclear Science, **15**, 1968, pp. 266-274.
[33] Nesdoly M.T.A., *X-ray Sensitivity and X-ray Induced Charge Transport Changes in Stabilized a-Se Films,* Ph. D. Thesis, University of Saskatchewan, Saskatoon, Canada, 2000.
[34] Martini M., Mayer J.W., and Zanio K.R., "Drift velocity and trapping in semiconductors – transient charge technique", *Applied State Science: Advances in Materials and Device Research*, edited by R. Wolfe, Academic Press, 1972.
[35] Blakney R.M. and Grunwald H.P., "Small-signal current transients in insulators with traps", Physical Review, **159**, 1967, pp. 658-664.
[36] Blakney R.M. and Grunwald H.P., "Trapping processes in amorphous selenium", Physical Review, **159**, 1967, pp. 664-671.

[37] Kasap S.O., Thakur R.P.S., and Dodds D., "Method and apparatus for interrupted transit time transient photoconductivity measurements", Journal of Physics E: Scientific Instrumentation, **21**, 1988, pp. 1195-1202.
[38] Kepler R.G., "Charge carrier production and mobility in anthracine crystals", Physical Review, **119**, 1960, pp. 1226-1229.
[39] LeBlanc O.H., "Hole and electron drift mobilities in anthracine", Journal of Chemical Physics, **33**, 1960, pp. 626.
[40] Brown F.C., "Temperature dependence of electron mobility in AgCl", Physical Review, **97**, 1955, pp. 355-362.
[41] Kasap S.O. and Juhasz C., "Transient photoconductivity probing of negative bulk space charge evolution in halogenated amorphous selenium films", Solid State Communications, **63**, 1987, pp. 553-556.
[42] Haugen C. J., *Charge Carrier Recombination in Amorphous Selenium Films*, M. Sc. Thesis, University of Saskatchewan, Saskatoon, Canada, 1995.
[43] Hirsh J., Jahankhani, H., "The carrier yield in a-Se under electron bombardment", Journal of Physics: Condensed Matter, **1**, 1989, 8789-8798.
[44] Kasap S.O., Polischuk B. and Dodds D., "An interrupted field time-of-flight (IFTOF) technique in transient photoconductivity measurements", Review of Scientific Instruments, **61**, 1990, pp. 2080-2087.
[45] Polischuk B., and Kasap S.O., "A high-voltage interrupted-field time-of-flight transient photoconductivity apparatus", Measurement Science & Technology, **2**, 1991, pp. 75-80.
[46] Yannacopoulos, S. and Kasap, S.O., "Glass transformation phenomena in bulk and film amorphous selenium via DSC heating and cooling scans", Journal of Materials Research, **5**, 1990, pp. 789-794.
[47] Tonchev, D. and Kasap, S.O., "Effect of aging on glass transformation measurements by temperature modulated DSC", Materials Science and Engineering, **A328**, 2002, pp. 62-66.
[48] Fogal B., Johanson R., Belev G., O'Leary S., Kasap S.O., "X-ray induced effects in stabilized a-Se X-ray photoconductors", Journal of Non-Crystalline Solids, **299-302**, 2002, pp. 993-997.
[49] Tan W.C., Belev G., Koughia, K., Johanson R., O'Leary S., Kasap S.O., "Optical properties vacuum deposited and chlorine doped a-Se thin fims: aging effects", Journal of Materials Science: Materials in Electronics, **18**, 2007, pp. S429-S433.
[50] Kasap S., Aiyah V., Polischuk B., Abkowitz M., "Determination of the deep-hole capture cross section in a-Se via xerographic and interrupted-field time-of-flight techniques", Philosophical Magazine Letters, **62**, 1990, pp. 377-382.

Appendix: Sensitivity Calculations

1. Introduction

The performance of a direct-conversion x-ray detector is directly related to the properties of the material being used to absorb the incoming x-rays and convert them into electrical charges. The sensitivity of the material is of particular importance to the performance of the detector, as it determines just how well a material can act as a direct conversion photoconductor. In this section, a brief derivation of the formulas used to calculate the sensitivity of the amorphous selenium samples used in this work is given, as well as the MATLAB code used to perform the calculation.

2. Calculation

The sensitivity of a photoconductor is given by the collected charge per unit area per unit exposure of x-ray radiation. Thus, the sensitivity can be examined in relation to three main factors. The first factor is how much of the incident x-ray energy is actually absorbed by the material. This is found from the quantum efficiency of the detector which is dependent on the photoconductor thickness and the photoelectric absorption coefficient, α, which is dependent on the incident x-ray photon energy, E_{ph} [i]. The next factor determining the sensitivity of the material is how many EHPs will be generated from the absorbed x-rays. This is based on the EHP creation energy $W_{\pm}$, which is dependent on the material properties and applied electric field [ii]. The third factor is how much of the generated electrical charge is actually collected in the external circuitry of the detector. This is determined by the charge transport properties of the material (mobility, lifetime), as well as the thickness of the photodetector and the pixel size [i].

To find an expression for sensitivity, a high-resistivity photoconductor (such as a-Se) is connected to a bias voltage like that shown in Figure A.1. Incident x-ray electrons

are absorbed exponentially as exp(-αx) along the photoconductor thickness and generate an EHP concentration profile that follows the absorbed incident x-ray photon profile. The generated electrons and holes will split up and travel in opposite direction under the applied field and generate a transient photocurrent. For this calculation, the applied bias is assumed to be negative.

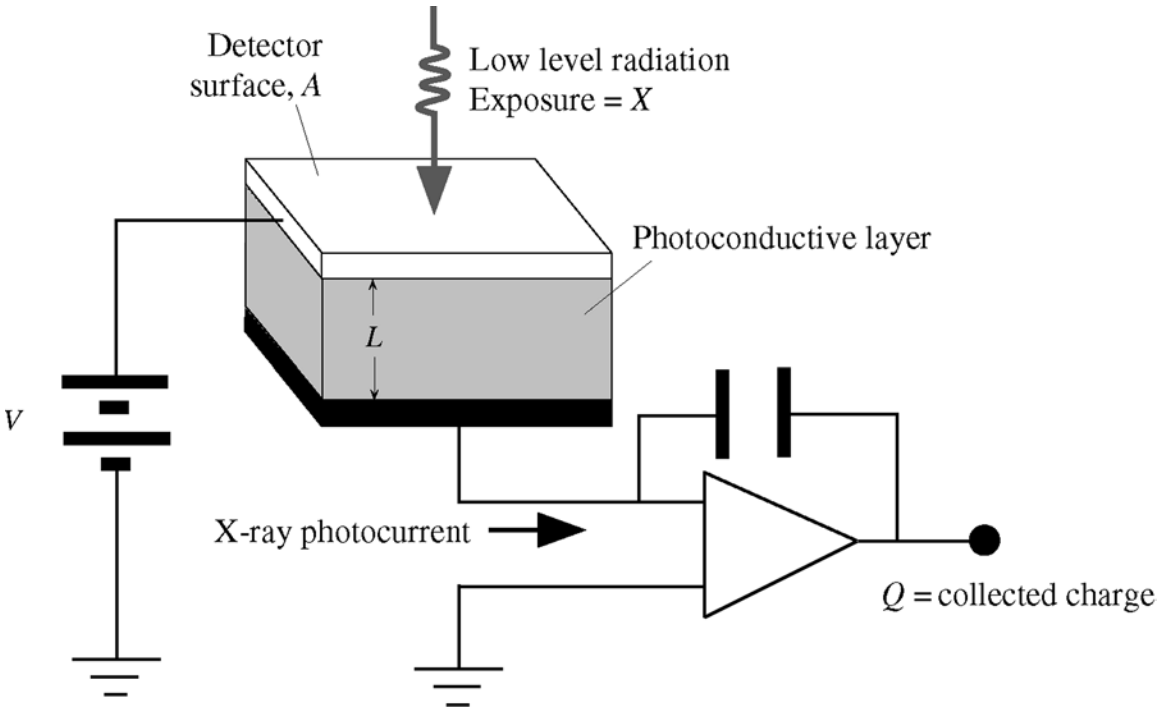

Figure A.1: Schematic diagram of a photoconductor sandwiched between two metal plates as electrodes. From [iii].

A number of assumptions are used to simplify the derivation. First, the applied field is assumed to be uniform throughout the photoconductor, essentially making this derivation for the small signal condition. The diffusion of carriers is also assumed to be negligible compared with their drift. Next, the mobility μ and lifetime τ are assumed to be constant for both electrons and holes. The loss of carriers to deep trapping is also assumed to be more significant than losses to bulk recombination. The incident x-ray pulse is also assumed to be monoenergetic and much shorter in duration than the carrier transit time through the photoconductor. Also, small pixel effects are neglected so that the collected charge can be found by the integration of the total photocurrent. Finally, any damage induced by the incident x-rays is ignored.

The x-ray sensitivity of the photodetector is defined as the collected charge per unit area per unit exposure of x-ray radiation,

$$S = \frac{Q}{AX} \tag{1}$$

where S is the sensitivity, Q is the total charge collected, A is the receiving area, and X is the x-ray exposure. With the assumptions listed above, with a full calculation that can be found in [iv], the total collected charge can be found to be:

$$\begin{aligned} Q = {} & \frac{5.45\times10^{13}\times eAX}{(\alpha_{\text{air}}/\rho_{\text{air}})W_{\pm}}\left(\frac{\alpha_{\text{en}}}{\alpha}\right)\times \\ & \left\{\frac{\mu_e\tau_e F}{L}\times\left[\left(1-e^{-\alpha L}\right)+\frac{1}{1/(\alpha\mu_e\tau_e F)-1}\left(e^{-L/\mu_e\tau_e F}-e^{-\alpha L}\right)\right]\right. \\ & \left.+\frac{\mu_h\tau_h F}{L}\times\left[\left(1-e^{-\alpha L}\right)-\frac{1}{1/(\alpha\mu_h\tau_h F)+1}\left(1-e^{-\alpha L-L/(\mu_h\tau_h F)}\right)\right]\right\} \end{aligned} \tag{2}$$

where e is the elementary charge, α_{air} and ρ_{air} are the energy absorption coefficient and the density of the air respectively, $W_{\pm}$ is the EHP creation energy, α_{en} and α are the energy absorption coefficient and the linear attenuation coefficient of the photoconductor respectively, L is the detector thickness, and $\mu_e\tau_e F$ and $\mu_h\tau_h F$ are the electron and hole schubwegs respectively.

Substituting equation 2 into 1 and using the normalized attenuation depth, $\Delta=1/(\alpha L)$ and the electron and hole schubwegs per unit thickness $x_e = \mu_e\tau_e F$ and $x_h = \mu_h\tau_h F$ respectively in order to simplify the writing of the equation, an expression for the sensitivity is found:

$$\begin{aligned} S = {} & \frac{5.45\times10^{13}\times e}{(\alpha_{\text{air}}/\rho_{\text{air}})W_{\pm}}\left(\frac{\alpha_{\text{en}}}{\alpha}\right)\times\left\{x_e\left[\left(1-e^{-1/\Delta}\right)+\frac{1}{\Delta/x_e-1}\left(e^{-1/x_e}-e^{-1/\Delta}\right)\right]\right. \\ & \left.+x_h\left[\left(1-e^{-1/\Delta}\right)-\frac{1}{\Delta/x_h+1}\left(1-e^{-1/\Delta-1/x_h}\right)\right]\right\} \end{aligned} \tag{3}$$

which gives the sensitivity in C cm^{-2} R^{-1}. It should be noted that this equation applies only to the case where there is a *negative* bias. If *positive* bias is present, then the terms x_e and x_h should be interchanged.

Due to the complexity of the expression for sensitivity, performing repeated calculations by hand is incredibly time consuming. To facilitate easier and quicker calculations of the sensitivity, a MATLAB function was generated to calculate the sensitivity. This function takes in user-defined values for electron mobility μ_e, electron lifetime τ_e, hole mobility μ_h, hole lifetime τ_h, detector thickness L, applied bias V, incident x-ray energy E_{ph}, and allows the user to specify whether the detector will be operated with positive or negative bias.

One of the key elements for calculating the sensitivity, the EHP creation energy $W_{\pm}$ is dependent on the detector thickness, and applied field. Therefore, it was important to have a system to calculate $W_{\pm}$ for varying conditions. Though an exact method for determining $W_{\pm}$ in a-Se has yet to be found, work done by [iii] has indicated that $W_{\pm}$ can be approximated by:

$$W_{\pm} \approx W_{\pm}^{o} + \frac{B}{F}$$

where $W_{\pm}^{o}$ = 6eV, B = 4.4×10^6 eV cm^{-1}, and F is the applied field, V/L in V/μm.

Several material constants were also needed in order to calculate the sensitivity. These include values for the mass energy absorption coefficient of air (α_{air}) and mass energy absorption (α_{en}) and linear attenuation (α) coefficients for Se, all of which are dependent on the incident x-ray photon energy. In order to calculate these quantities for varying incident x-ray energy, data from the website of the National Institute of Standards and Technology Physics Laboratory [v] shown in Figure A.2 and Figure A.3 was fit with a power law to generate expressions for α_{en}, and α. For the purposes of calculations, the density of Se was taken to be ρ_{Se} = 4.3 g/cm^3 [iii] and the density of air was taken to be $\rho_{\text{air}} = 1.2 \times 10^{-3}$ g/cm^3 [v]. The power law fits for α and α_{en} are as follows:

$$\alpha = \rho_{\text{Se}} \times 127435 \times \left(\frac{E_{ph}}{1000}\right)^{-2.644} \qquad \text{for } 12.6578\text{keV} \le E_{ph} \le 90\text{keV}$$

$$\alpha_{\text{en}} = \rho_{\text{Se}} \times 76571 \times \left(\frac{E_{ph}}{1000} \right)^{-2.6035} \qquad \text{for } 12.6578\text{keV} \le E_{ph} \le 90\text{keV}$$

α_{air} was found by using an expression found in [vi] for photon fluence. Photon fluence, Ψ_{ph}, is given by

$$\Psi_{ph} = \frac{8.73 \times 10^{-6}}{eE_{ph}\left(\alpha_{\text{air}} / \rho_{\text{air}}\right)}$$

Solving for α_{air} gives:

$$\alpha_{\text{air}} = \frac{\rho_{\text{air}} \times 8.73 \times 10^{-6}}{e\Psi_{ph}E_{ph}} \qquad \text{for } 3.20290\text{keV} \le E_{ph}$$

where Ψ_{ph} can be found from:

$$\Psi_{ph} = \left(-5.0233 \times 10^{-6} + 1.8106 \times 10^{-7} \sqrt{\frac{E_{ph}}{1000}} \ln\left(\frac{E_{ph}}{1000} \right) + \frac{0.0088387}{\left(\frac{E_{ph}}{1000} \right)^2} \right)^{-1}$$

With the constants defined, the calculation for sensitivity can now be performed for different conditions.

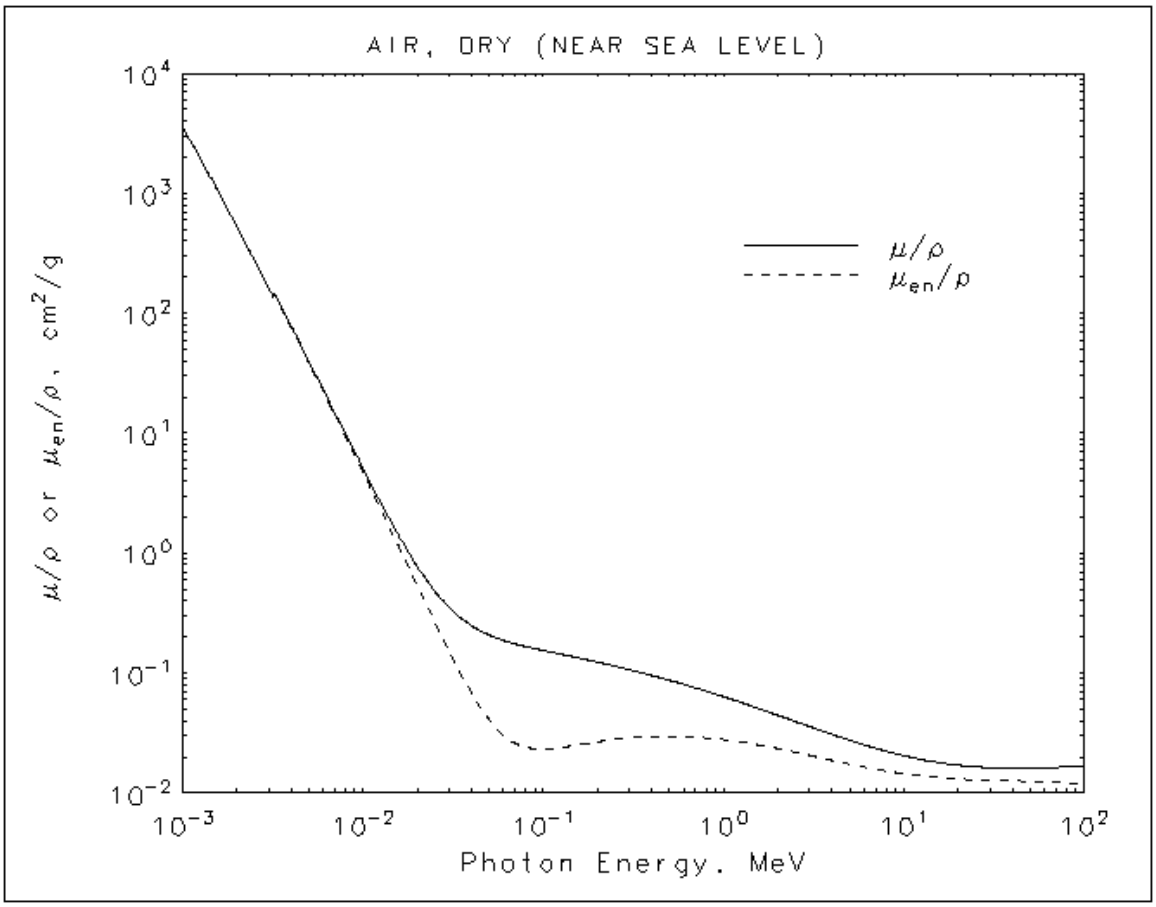

Figure A.2: Plot of the mass energy absorption coefficient (α_{air}) vs. incident x-ray photon energy for air.

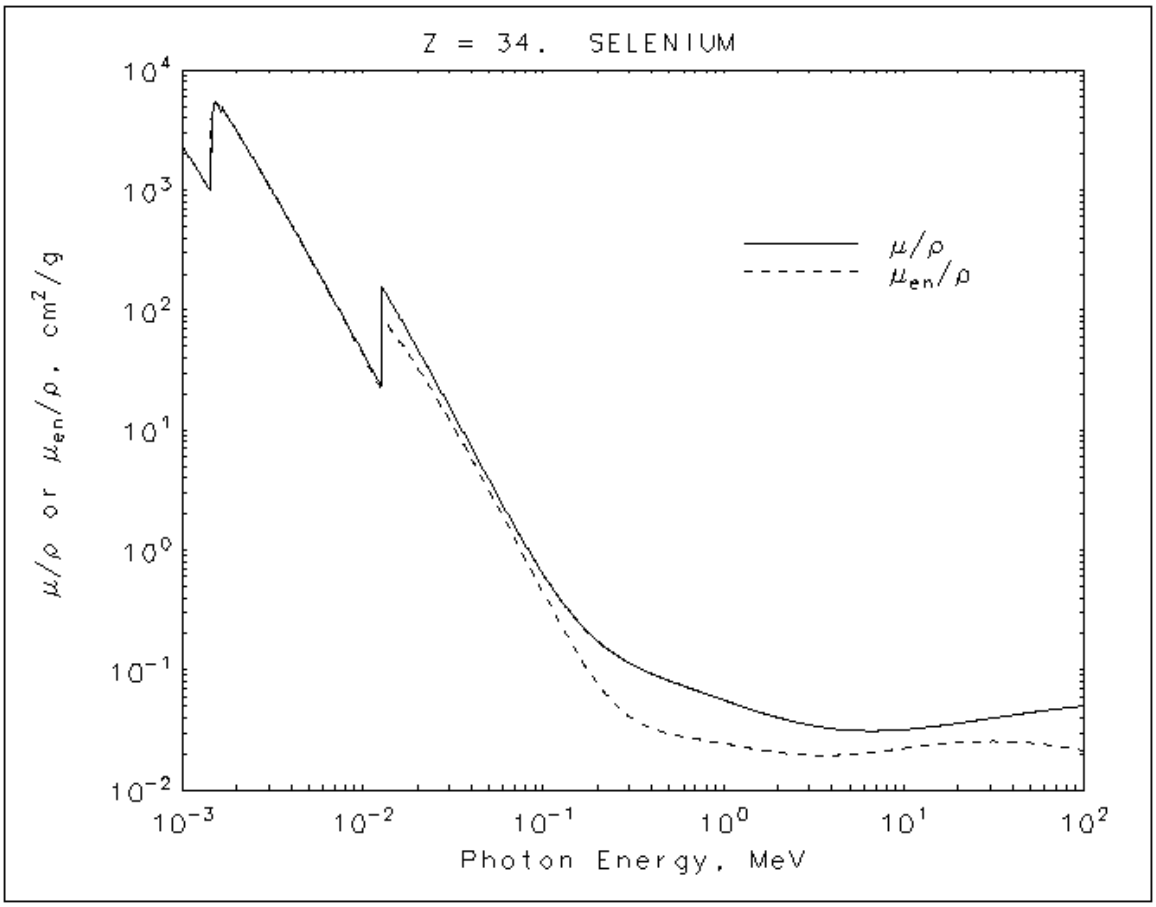

Figure A.3: Plot of the mass energy absorption coefficient (α_{en}) and linear attenuation coefficient (α) vs. incident x-ray photon energy for Se.

3. MATLAB Code

The following is the MATLAB code used to calculate the sensitivity in this work. It is a function that takes in user-defined values for electron mobility μ_e, electron lifetime τ_e, hole mobility μ_h, hole lifetime τ_h, detector thickness L, applied bias V, incident x-ray energy E_{ph}, and allows the user to specify whether the detector will be operated with positive or negative bias and then calculates the sensitivity as well as the charge collection efficiency. The code is as follows:

```
function [Sunits,ncc] = Sensitivity(top, mu_e_in, mu_h_in, tau_e_in, tau_h_in,
L_in, Eph_in, V)
%   Sensitivity calculates the sensitivity and charge collection efficiency
%           for a given set of parameters; the mutau values for both holes
%           and electrons are required, as well as the thickness, incident
```

```
%           x-ray energy, and the apllied voltage
%
%   Synopsis:
%       [Sunits,ncc] = Sensitivity(top, mu_e_in, mu_h_in, tau_e_in, tau_h_in,
L_in, Eph_in, V)
%
%   Input:
%       top = current bias for the calculation, top = 0 for negative bias, top
= 1 for positive
%       mu_e_in = electron mobility in cm^2/V^-1s^-1
%       mu_h_in = hole mobility in cm^2/V^-1s^-1
%       tau_e_in = electron lifetime in us
%       tau_h_in = hole lifetime in us
%       L_in = thickness in um
%       E_ph_in = energy of the incident x-ray, in keV
%       Note: the fits for the alpha values only apply well for 12.6578 keV
%       < Eph < 60 keV, see m-file for details
%       V = applied voltage, in Volts
%
%   Output:
%       Sunits = sensitivity in pC cm^-2 mR^-1
%       ncc = the charge collection effeciency

%Constants
W_pmo = 6; %Value for EHP creation energy when field is infinite, in eV
B = 4.4e6*1e2; %Constant used for EHP creation energy calculation eV/m
ro_Se = 4.3; %Density of a-Se in g /cm^3
ro_air = 1.2e-3; %Density of air in g/cm^3

%Convert inputs into specific units
mu_e = mu_e_in*1e-4; %convert the mobilities to m^2/V^-1s^-1
mu_h = mu_h_in*1e-4;
tau_e = tau_e_in*1e-6; %convert the lifetimes to s
tau_h = tau_h_in*1e-6;
L = L_in*1e-6; %convert the thickness to m
Eph = Eph_in*1e3; %converts the incident energy into eV

%Calculate values used to find the sensitivity
F = V/L; %Applied field, in V/m
W_pm = W_pmo + B/F; %EHP creation energy
%The values for alpha are from fitting power laws to the data from
%http://physics.nist.gov/PhysRefData/XrayMassCoef/cover.html
%for a-Se, the fitting equation applies only for Eph > 12.6578 keV
%for air, Eph > 3.20290 keV, but rapidly loses accuracy for Eph > 60 keV
alpha = ro_Se*127435*100*(Eph/1000)^(-2.644);   %Linear attenuation coefficient
for a-Se, 1/m
alpha_en = ro_Se*76571*100*(Eph/1000)^(-2.6035);  %Energy absorbtion
coefficient for a-Se, 1/m
%J.M.Boone, Ch1, Eq 1.22b, photon fluence per 1 mR and per mm^2
alpha_air = ro_air*8.73e-6/(1.602e-19*Eph*(-5.0233e-6+1.8106e-
7*sqrt(Eph/1000)*log(Eph/1000)+8.8387e-3/((Eph/1000)^2))^-1*1e5);
%Energy absorbtion coefficient for air, 1/cm

delta=1/(alpha*L); %Used to simplify the equation writing


%Adjusts the calculation based on positive or negative bias
if top==1
    x = [(mu_h*tau_h*F/L) (mu_e*tau_e*F/L)];
else
    x = [(mu_e*tau_e*F/L) (mu_h*tau_h*F/L)];
end
```

```
%Calculate the Sensitivity
for index = 1:2
    Sen(2*index-1) = (5.45e13*1.602e-
19/(alpha_air/ro_air*W_pm))*(x(index))*(alpha_en/alpha);
end
Sen(2) = (1-exp(-1/delta))+1/(delta/x(1)-1)*(exp(-1/x(1))-exp(-1/delta));
Sen(4) = (1-exp(-1/delta))-1/(delta/x(2)+1)*(1-exp(-1/delta-1/x(2)));

S = Sen(1)*Sen(2)+Sen(3)*Sen(4); %Calculates the Sensitivity in C cm^-2 R^-1
normS=S/((5.45e13*1.602e-19/(alpha_air/ro_air*W_pm))*(alpha_en/alpha));
%Normalized Sensitivity
Sunits = S/1e3/1e-12;    %Sensitivity in pC cm^-2 mR^-1

%Calculate the charge collection efficiency
ncc=x(2)*(1-((1-exp(-1/delta-1/x(2)))/((1+delta/x(2))*(1-exp(-
1/delta)))))+x(1)*(1-(exp(-1/x(1))-exp(-1/delta))/((1-delta/x(1))*(1-exp(-
1/delta))));
```

4. Conclusion

The sensitivity of a photoconductor is a very important factor in determining how well a material will work in a photodetector. A formula to find the sensitivity based on the charge transport properties of a-Se was determined and programmed into MATLAB. With this MATLAB function, the sensitivity before and after the relaxation was calculated to see the effects of the relaxation process on the sensitivity of a-Se as a photodetector. The results from this calculation can be found in Chapter 5.

---

[i] Kabir M., Kasap S.O., Zhao W., Rowlands J.A., "Direct conversion X-ray sensors: sensitivity, DQE and MTF", IEE Proceedings - Circuits, Devices and Systems, V, 150, No. 4, 2003, pp. 258-266.

[ii] Kabir, M.Z., Kasap, S.O., "DQE of photoconductive X-ray image detectors: application to a-Se", Journal of Physics D: Applied Physics, **35**, 2002, pp. 2735–2743.

[iii] Kasap, S.O., "X-ray sensitivity of photoconductors: application to stabilized a-Se", Journal of Physics D: Applied Physics, **33**, 2000, pp. 2853-2865.

[iv] Kabir, M., Kasap, S.O., "Charge collection and absorption-limited sensitivity of x-ray photoconductors: Applications to a-Se and HgI2", Applied Physics Letters, **80**, 2002, pp. 1664-1666.

[v] http://physics.nist.gov/PhysRefData/XrayMassCoef/cover.html

[vi] Boone J.M. "X-ray production, interaction and detection in diagnostic imaging", Chapter 1 in *Handbook of Medical Imaging: Volume 1, Physics and Psychophysics*, edited by J. Beutel, H.L. Kundel, and R.L. Van Metter, SPIE Press, Bellingham, 2000, pp. 1-78.